Winter 12-15-2023

# MICROPLATE-LIKE METAL PYROPHOSPHATE ENGINEERED ON NI-FOAM TOWARDS MULTIFUNCTIONAL ELECTRODE MATERIAL FOR ENERGY CONVERSION AND STORAGE

Rishabh Srivastava
*Pittsburg State University*, rivastava@gus.pittstate.edu

### Recommended Citation

MICROPLATE-LIKE METAL PYROPHOSPHATE ENGINEERED ON NI-FOAM
TOWARDS MULTIFUNCTIONAL ELECTRODE MATERIAL FOR ENERGY
CONVERSION AND STORAGE

A Thesis Submitted to the Graduate School
in Partial Fulfilment of the Requirements
For the Degree of
Master of Science

Rishabh Srivastava

Pittsburg State University

Pittsburg, Kansas

December, 2023

MICROPLATE-LIKE METAL PYROPHOSPHATE ENGINEERED ON NI-FOAM
TOWARDS MULTIFUNCTIONAL ELECTRODE MATERIAL FOR ENERGY
CONVERSION AND STORAGE


Rishabh Srivastava


APPROVED:

Thesis Advisor _____

                Dr. Ram K. Gupta, Department of Chemistry


Committee Member _____

                Dr. Serif Uran, Department of Mathematics and Physics


Committee Member _____

                Dr. Khamis Siam, Department of Chemistry

## Acknowledgments

Firstly, the foremost gratitude I would like to express to my research and program advisor Dr. Ram K. Gupta for his enormous support and guidance. His teaching methods led me to enrich my academics and research aptitude. His supervision and guidance led me to conduct my research productively and effortlessly. Moreover, Dr. Gupta supervised my hands-on training in various techniques and equipment in the laboratory, as well as generously offering his electrochemistry, battery, and polymer expertise. I would like to express many thanks for his mentorship and continuous encouragement to write and read about new scientific discoveries in the world outside my research scope. It updated my knowledge of the new scientific world and although it was challenging, the last two years of my Master program have been the most productive so far. Again, I would like to say thank you to him.

Secondly, I would like to acknowledge my thanks to Dr. William Shirley who provided me with great lectures on Chemical thermodynamics with his passion and effort. As a result, I learned a great deal about intrinsic and extrinsic chemistry of the materials which is very useful for recent technological enhancement in the energy sector. I would also like to say thank you to Dr. Tim Dawsey who has been one of the pillars of the National Institute for Materials Advancement. He provided not only academic knowledge during research meetings but also guidance and support to succeed now and in my future academic endeavours.

Thirdly, I would also like to extend my appreciation to my committee members: Dr. Serif Uran and Dr. Khamis Siam. Their advice and suggestions about my thesis enabled me to write a better one. Despite their busy schedules, they made time to support my academic efforts, and I thank them for sharing their precious insight.

# MICROPLATE-LIKE METAL PYROPHOSPHATE ENGINEERED ON NI-FORM TOWARDS MULTIFUNCTIONAL ELECTRODE MATERIAL FOR ENERGY CONVERSION AND STORAGE

An Abstract of the Thesis by
Rishabh Srivastava

High clean energy demand, dire need for sustainable development, and low carbon footprints are the few intuitive challenges, leading researchers to aim for research and development for high-performance energy devices. The development of materials used in energy devices is currently focused on enhancing the performance, electronic properties, and durability of devices. Tunning the attributes of transition metals using pyrophosphate ($P_2O_7$) ligand moieties can be a promising approach to meet the requirements of energy devices such as water electrolyzers and supercapacitors, However, such a material's configuration is rarely exposed for this purpose of study.

Herein, we grow $Ni_2P_2O_7$, $Co_2P_2O_7$, and $Fe_2P_2O_7$ composites on conductive Ni-foam using a hydrothermal procedure. The results indicated that, among all the synthesized samples, $Fe_2P_2O_7$ exhibited outstanding oxygen evolution reaction (OER) and hydrogen evolution reaction (HER) with the least overpotential of 220 and 241 mV to draw a current density of 10 mA/cm$^2$. Further, wastewater rich in urea from sanitary units and industries is subjected to produce green energy through wastewater-splitting. Thus, urea oxidation reaction (UOR) is the most widely promoted. We employed synthesized composites towards UOR investigation, and it was found that $Fe_2P_2O_7$ exhibits splendid performance with the low onset potential of 1.317 V (vs RHE) at 10 mA/cm$^2$ of current density. The low Tafel slope, high turnover frequency, low charge transfer resistance, greater electrochemical surface area, and roughness factor

contribute to enriching the performance of $Fe_2P_2O_7$ as an effective electrocatalyst towards OER, HER, and UOR. Theoretical studies indicate that the optimal electronic coupling of the Fe site with the pyrophosphate enhances the overall electronic properties of $Fe_2P_2O_7$, thereby, showing its electrocatalytic performance concerning freshwater and wastewater-splitting. Moreover, the composite materials showed the best capacitive properties for supercapacitor energy storage applications. The specific capacitance offered by composite materials ranges from 3000-8000 $mF/cm^2$ at 1 $mA/cm^2$. Additionally, it possessed high capacitance retention and coulombic efficiency up to 5,000 charge/discharge cycles.

Consequently, this work suggests how to use pyrophosphate moieties to fabricate non-noble metal-based electrode materials to achieve good performance in electrocatalytic splitting water as energy conversion and supercapacitors as energy storage applications.

**TABLE OF CONTENTS**

# LIST OF TABLES

# LIST OF FIGURES

**CHAPTER I**

**INTRODUCTION**

## 1.1 Need for Energy

The global energy crisis and prominent environmental concerns significantly influence our ecosystems, public human health, and the economy. Therefore, proper action is required to limit the negative impact of such certainties on our everyday lives, for instance, the increase in oil prices, and health complications due to environmental contamination. To tackle these challenges, we have fastened the step to exploit a new type of clean energy technology, and efficient energy storage devices are required. Of high energy density, power density, efficiency, and green nature, splitting water for hydrogen energy generation has drawn the momentous attention of researchers and supercapacitor devices towards storing energy, consequently known as energy conversion and storage, respectively.

## 1.2 Introduction of electrocatalyst for water splitting

The sixth assessment report of the Intergovernmental Panel on Climate Change (IPCC), USA, released in August 2021, concerns the seriousness and urgency of the climate crisis [1]. Therefore, the United States and China recalled their joint statement, which addressed the successful implementation of policies and measures to reduce the emissions of greenhouse gases effectively. To corroborate the action, they reemphasized

the implementation of the Paris Agreement for combating the climate catastrophe and targeting the average increase in global temperature for limiting to 1.5 ºC, which is currently increasing at the rate of 2 ºC [2]. On the other hand, niches in urbanization and industrialization have caused tremendous use of fossil fuels, resulting in an upsurge in metropolitan air pollution, leading to environmental damage, global warming, and carcinogenic effects. To overcome the running issues, the two countries agreed to distributed generation policies that encourage clean and sustainable power production [3,4]. Therefore, the renewable sector is producing and developing cost-effective and superior-quality electrodes for energy conversion. In this respect, scientists are developing sustainable alternatives for energy production, as the demand for zero-emission automobiles has increased. The energy demand is expected to grow from 16 Terawatt (TW) in 2010 to 23 TW in 2030, and even up to 30 TW in 2050 [5]. Thus, among various greenways of energy production, the best representative is electrocatalytic water splitting, which involves hydrogen and oxygen evolution from water.

Hydrogen is a pivotal energy source. It is mainly utilized to produce ammonia for fertilizer and to refine petroleum. In addition, a tremendous amount of hydrogen is used for aerospace missions and fuel cell-driven electric vehicles, which have recently attracted much attention [6]. Hydrogen can be driven by steam methane reforming, coal gasification, and water electrolysis. On the one hand steam methane reforming and coal gasification methods are considered as clean energy production with the efficiency of 95% of hydrogen. On the other hand, both processes simultaneously contribute to environmental pollution due to the emission of $CO_2$ [7]. Therefore, many studies were conducted on water electrolysis methods that do not report the generation of $CO_2$ as one of the end products. Moreover, another important product of water electrolysis is

Oxygen gas, in particular, which is always in higher demand in hospitals for medical purposes and also used for the storage mechanism of the metal-air battery, recognized as a new generation battery as it delivers higher energy density of 5,200 Wh/Kg than Li-ion battery (200-250 Wh/Kg) [8]. For these reasons, the development of a method capable of producing hydrogen and oxygen from water seems essential.

An electrolyzer is a device that helps to improve the productivity of the water-splitting process, consisting of cathode, anode, and aqueous electrolyte where hydrogen evolution reaction (HER) and oxygen evolution reaction (OER) take place on the cathode and anode, respectively. Based on thermodynamic consideration, the water-splitting potential is 1.23 V at 25 ºC regardless of media. However, extra voltage, called overpotential should be applied for water-splitting. The anodic process (OER) is exceedingly sluggish due to the large re-organization energy of oxygen released from water. This limits the overall water-splitting process and necessitates the use of effective electrocatalysts. By optimizing the adsorption energies of intermediates ($OH^*$, $O^*$, and $OOH^*$) on active sites of a catalyst, an electrocatalyst can often lower the activation energy of the rate-determining step of water-splitting. Additionally, to attain efficient overall water-splitting in an alkaline medium, developing an efficient electrocatalyst for HER ($2H^+ + 2e^- \rightarrow H_2$) and OER ($4OH^- \leftrightarrow 2H_2O + O_2 + 4e^-$) is significantly vital, where electrocatalyst are needed to reduce the overpotential for the breakdown of water [6]. Recently, urea-rich wastewater splitting or urea oxidation reaction (UOR) has attracted great attention in urea-dependent energy conversion technologies, as it allows for the production of hydrogen and the treatment of urea-rich wastewater [9]. Thermodynamically it requires a lower potential of 0.37 V than the OER. Therefore, UOR offers more energy efficiency in hydrogen generation via electrochemical water-splitting. Since UOR is driven by six-electron-transfer process deemed to be kinetically

stubborn ($CO(NH_2)_2 + 6OH^- \rightarrow N_2 + 5H_2O + CO_2 + 6e^-$) [10]. Thus, HER, OER, and UOR require highly active, stable, and high-performance electrocatalysts. On the other hand, traditional catalysts such as Pt/C, oxides of ruthenium, and iridium, showed promising terms towards catalytic activity. However, their use on a broad scale is driving up both their market prices and the limitations of their use for other applications [11]. Therefore, the concerned science societies are engaged in finding suitable alternatives with excellent activities, durability, and stability.

After a long-term exploration by researchers, transition metals (Ni, Fe, Co, and Mn) are perceived with similar valence shell electronic configuration of $3d^{6-8}4s^2$, additionally, as expected options for their abundance of presence in nature and sensible expense so numerous efforts have been done and transition metal-based oxides [12], hydroxides [13], phosphides [14], sulfides [15], chalcogenides [16], double perovskites [17], MXenes [18], metal-organic framework [19] and carbon-based composites [20] have been investigated. However, these materials still possess limitations due to poor alteration of transition metal electronic characteristics by corresponding oxide, sulfide, and phosphide frameworks [21]. Thus, it was hypothesized that the pyrophosphate framework would demonstrate exceptional electronic alteration of transition metal atoms as well as possess outstanding physical and chemical properties. Pyrophosphates have been also investigated due to their layered crystal structure and unique physicochemical attributes [22]. These pyrophosphates are the derivatives of metal phosphates tetrahedra ($PO_4^{3-}$) to form one pyrophosphate ($P_2O_7^{4-}$) [23]. For example, Mn, Co, and Ni transition metals were integrated into a pyrophosphate framework, forming $Mn_2P_2O_7$, $Co_2P_2O_7$, and $Ni_2P_2O_7$. Hence, the peculiar property of the pyrophosphate groups has attracted substantial attention from researchers for improved water-splitting performance. To date, only a few investigations have been reported on

metal pyrophosphates concerning electrocatalytic purposes. For instance, Liu et al. [24] synthesized cobalt iron orthophosphate, pyrophosphate, and tripolyphosphate by using a co-precipitation strategy. Among them, cobalt iron pyrophosphate showed high durability of about 90% after 30,000 s in 1 M KOH due to its nanosheet morphology with porous structure. Likewise, Chang et al. [25] reported a nanocrystal like $Co_2P_2O_7$ with porous nanocarbon towards OER, attained 397 mV of overpotential in 10 mA/cm$^2$. Correspondingly, Du et al. [26] and Wulan et al. [27] also fabricated metal pyrophosphate electrocatalysts for water-splitting.

## 1.3 Introduction of supercapacitor

An emerging industry of electric vehicles is touching the paramount demand for lithium-ion batteries due to its high energy density; it is also used in various applications such as laptops, and mobile phones. The rechargeable Li-ion batteries consist of a cathode which is layered $LiMO_2$ (M = Co, Ni, Mn) materials, and anode of graphite materials. Charge storage can take place when Li-ion is introduced between each layer of the host materials. Whereas, the diffusion of ions within the bulk of crystalline materials obstructs the charge-discharge rate of the battery, resulting in poor power density [28]. This disadvantage limits the use of batteries in electric vehicles. Therefore, supercapacitors came into existence which are referred to as promising candidates for energy storage applications with fast charging and long cycle life. The energy storage ability of supercapacitors is higher than that of traditional capacitors, and their power density is higher than secondary batteries [29]. Hence, supercapacitors can be used in electric and hybrid vehicles to provide a high power density and short duration of acceleration for energy recovery throughout braking, in this sense, saving energy and

protecting the life of the battery from the rapid phase of high-frequency dynamic operation [30].

There are three types of supercapacitors based on their working principles. (1) Electrochemical double-layer capacitors (EDLC), (2) Pseudo capacitors, and (3) Hybrid supercapacitors [31]. EDLC works on electrostatically ion adsorption/desorption at the interface of electrode and electrolyte. The electrochemical double layer is the concept of energy storage in EDLCs. It obeys a non-faradic process which makes it unique and different from batteries because EDLCs can withstand millions of cycles in comparison to batteries which go just a few thousand. Secondly, pseudo capacitors are the supercapacitors that work on faradic mechanisms, like oxidation and reduction reactions are involved for storing charges, and charges transfer between electrolyte and electrode. Thus, this type of supercapacitor follows diffusion and capacitive behavior, resulting in achieving greater specific capacitance as well as energy densities than EDLCs [32]. Finally, hybrid supercapacitors are devices that agglomerate the traits of EDLC and pseudo capacitors into one device which is further bifurcated into two types of asymmetric hybrids and composite hybrids. Asymmetric hybrids consist of EDLC-type electrodes (carbon-based materials) and pseudo capacitors-type electrodes (transition metal oxide or conducting polymer) as anode and cathode, respectively [33]. Whereas, composite hybrids configure pseudo capacitors-based materials and EDLC-based materials into a single electrode material. The EDLC materials provide a larger surface area and high conductivity, and pseudo capacitor materials possess faradic reactions, helping to reach greater specific capacitance [34].

Several attempts have been made to investigate effective electrode materials that may give high energy density and power density simultaneously, as the performance of supercapacitors greatly relies on the type of electrode materials [35]. Among various

6

transition metal-based materials, the olivine-structured transition metal pyrophosphate ($M_xP_2O_7$) is the best choice, as phosphorous is a non-metal having multiple vacancies, helping to increase the conductivity of the materials [36]. Pyrophosphates are more stable than phosphides and phosphates as they provide more pathways for a metal ion at a faster rate [36]. Moreover, metal pyrophosphates showed better results than metal oxides and metal phosphates due to the contribution from metal ions and strong P−O bonding which abruptly improved the conductivity and mechanical stability [37]. In addition to highly efficient electrochemical performance, transition metal-based pyrophosphates are recognized for their nontoxicity and biocompatibility [38]. A simple scalable synthesis route, cost-effective approach, appropriate pore network (pore diameter of around 15 nm), low internal resistance, extensive potential window due to the presence of oxygen, and excellent electrochemical properties make metal-pyrophosphate a potential candidate for supercapacitor study [39].

## 1.4 The objective of the thesis

Transition metal pyrophosphates-based composites are of great interest for studying their performance as an electrode material for energy conversion and storage purposes due to their salient features such as providing rich active sites and easily tuneable properties. However, the limitations of this type of materials bring a new chapter of interest to the scientific world such as their slow transport kinetics of charge carrier which hinders its activity, and poor performance in electrochemical reactions which is one of the reasons that polyphosphates are usually prepared at high temperature, lead to the shrinking of the materials and not a proper contact with a substrate, poor rate capability, increasing rate capacity and energy density are ongoing challenges. Therefore, the purpose of this study was to elevate the performance and stability of the

transition metal-based pyrophosphates for energy conversion and storage. First, the effective strategy was utilized to synthesize the nanostructured material with a finite morphology which assisted in getting higher surface area and porosity. Then, to promote the electrical transport coupling, a Ni-foam was employed as a substrate to grow composites on it. Later, addressing the rest of the limitations and enhancing its properties which help to open a new era in pyrophosphates-based material science. For detailed analysis of the transition metal-based pyrophosphate materials, various structural, and electrochemical characterizations were carried out.

**CHAPTER II**

**EXPERIMENTAL DETAILS**

## 2.1. Materials

Nickel foam (NF) was purchased from MTI-KJ Group, Richmond, California, USA. Nickel (II) nitrate hexahydrate [$Ni(NO_3)_2.6H_2O$, 98%] and cobalt (II) nitrate hexahydrate [$Co(NO_3)_2.6H_2O$, 98%] were ordered from STREM Chemicals, iron (II) nitrate nonahydrate [$Fe(NO_3)_2.9H_2O$, 98%] and urea [$CO(NH_2)_2$, 98%] from ACROS Organics, sodium phosphate monohydrate [$H_2NaPO_2.H_2O$, 99%] from Sigma Aldrich, ethanol and deionized (DI) water were purchased from Fischer Scientific, USA.

### 2.1.1 Transition metal pyrophosphates

Various transition metal-based pyrophosphates ($M_2P_2O_7$, M = Ni, Co, Cu, Zn, Fe, Mn, etc.) have been extensively utilized as electrode materials for energy conversion and storage devices to an edge due to several advantages, such as their distinct frameworks and structural stabilities which are constructed with phosphate/pyrophosphate/phosphorous ions [21]. Recently, it was hypothesized that the pyrophosphate framework would demonstrate exceptional electronic alteration of transition metal atoms as well as possess outstanding physical and chemical properties. However, pyrophosphates gathered attention as an electrode material because they offer a lot of space for the ions to propagate in the medium than the other phosphate materials [40]. These materials have attracted substantial attention from

researchers for improved water-splitting performance and energy storage capacity. For instance, Liang et al. [41] $Co_2P_2O_7$@N, P co-doped carbon nanocages as Mott-Schottky electrocatalyst towards better oxygen evolution reaction with the least overpotential. On the other hand, materials with amorphous phases or poor crystallinity may exhibit unique physical and chemical properties due to their unique disordered structures, mechanical and electric isotropy, and defect-rich characteristics. For example, $Na^+$ doped $Ni_2P_2O_7$, amorphous $Ni_2P_2O_7$, and porous $Co_2P_2O_7$, having different morphologies, were constructed and found to be promising materials in energy storage applications [42]. In the electrocatalytic and electrochemical reactions of supercapacitors, the amorphous phase of materials would allow deeper diffusion of the electrolyte ions to access the active materials and produce lower overpotential and higher capacitance than corresponding crystallized materials. Except the substantial amount of work that has been done on transition metal integrated pyrophosphate materials for applications involving energy storage, these materials have been inadequately investigated in electrocatalytic water splitting, urea oxidation, and seawater splitting [43]. In addition, theoretical research on pyrophosphate electrode materials is still limited to investigating the underlying chemistry of the influence that the framework of pyrophosphate has on transition metal atoms. Therefore, $Ni_2P_2O_7$, $Co_2P_2O_7$, and $Fe_2P_2O_7$ are extensively considered for water splitting, urea oxidation, and seawater splitting, and supercapacitors due to their high electrochemical performance, low cost, chemical stability, easily tuneable properties, and lower toxicity.

## 2.2. Synthesis of $Fe_2P_2O_7$, $Co_2P_2O_7$, and $Ni_2P_2O_7$

Transition metal-based pyrophosphate was synthesized by the facile hydrothermal technique. First, 3 mmol of sodium dihydrogen phosphate, 4 mmol of urea, and 20 ml of de-ionized water were added with 1 mmol of nickel nitrate, cobalt nitrate, and ferrous nitrate precursors in three different beakers, respectively. Further, the obtained solutions were homogeneously mixed at room temperature with the help of a stirring rod and sonication for 5 minutes. Later, all the prepared solutions and the Ni-foam (2 $\times$ 2 cm$^2$) were transferred into a 50 ml Teflon-lined stainless-steel vessel and heated at 180 °C for 12 h. When the reactor cooled to room temperature, the product was collected by centrifuge and washed with DI water and ethanol. After cleaning, the obtained Ni foams supported by $Ni_2P_2O_7$, $Co_2P_2O_7$, and $Fe_2P_2O_7$ arrays were transferred to an oven to dry overnight.
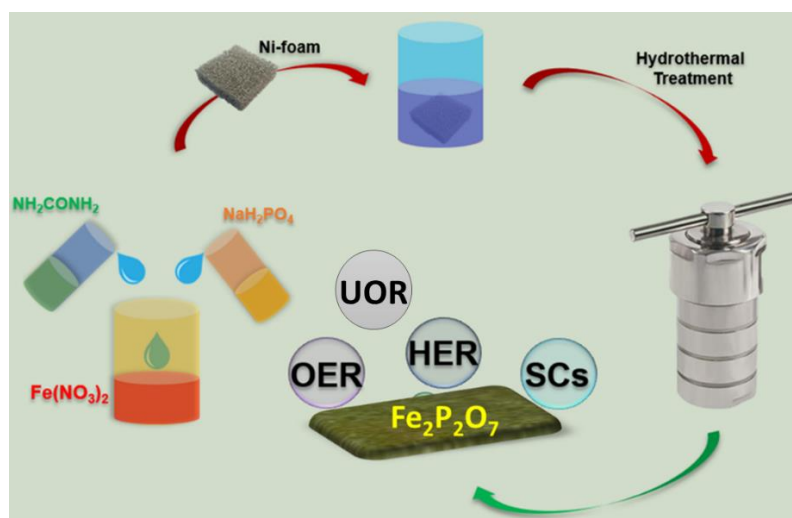


**Figure 2.1:** A schematic representation of a preparation of $Fe_2P_2O_7$ by hydrothermal route.

## 2.3 Physical characterization

The morphology and structure of synthesized metal-based pyrophosphate composite materials were investigated by field emission scanning electron microscopy

(FESEM) (SU 5000 – Hitachi), Energy dispersive X-ray analysis (EDAX, Oxford) under an operating voltage ranging from 0.1 to 30 kV, X-ray diffraction (XRD; Lab X, XRD-6000, Shimadzu X-Ray diffractometer Cu Kα source with a wavelength of 1.54 Å) (Columbia, MD, USA), X-ray photo-electron spectroscopy (XPS) (Thermo Scientific K-alpha, East Grinstead, UK) were collected using a Kratos Axis Ultra DLD spectrometer with a non-monochromatic Al $K_{\alpha}$ radiation and a beam size of ~ 1 mm. The curve fitting and quantitative analysis were obtained by measuring the area under the elemental and synthesized peaks. The binding energy of various core levels was determined by fitting the recorded spectra with Gauss-Lorentz curves. The data was analyzed using the NIST XPS database for peak assignment, and Fourier transform infrared spectroscopy (FT-IR) (PerkinElmer, USA).

### 2.3.1. Field-Emission Scanning Electron Microscopy

Field-Emission Scanning Microscopy was employed to investigate the morphology of all synthesized materials. The sample's morphology was obtained as electrons generated from electron beams bombarding the sample. The interaction between the incident electron and the sample can produce X-rays, Auger electrons, backscattered electrons, and secondary electrons. The morphology and topography are produced by the detection of the secondary electrons (all images were acquired at 10 keV) while the composition of elements in the samples was obtained by backscattered electrons.
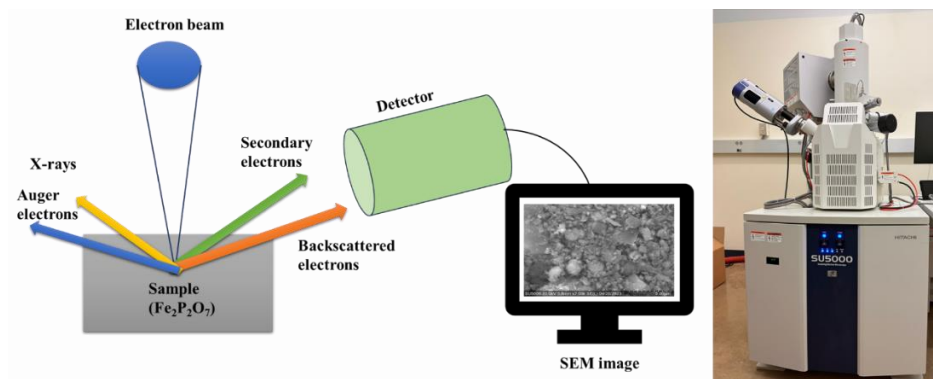
**Figure 2.2:** Schematic of SEM and the digital image of FESEM (SU 5000 - Hitachi) used in this research.

### 2.3.2. X-ray Diffraction

X-ray Diffraction measurement was utilized to study the crystal structure, phase purity, and crystallinity of all prepared composites. The XRD mainly consists of an X-ray tube and detector. The X-ray generated from the tube hit the sample in the middle of the instrument, and then the scattered X-ray was recorded by the detector. As the X-ray tube synchronized with the detector, X-ray diffraction patterns were observed at different angles. The structure and phase of crystalline material were investigated based on Bragg's law ($2d \sin\theta = n\lambda$) where n is the order of reflection, $\lambda$ is the wavelength of X-rays, d is the inter-planner spacing, and $\theta$ is the diffracted angle. The XRD pattern of all samples was obtained by Shimadzu X-ray diffractometer (XRD, CuK$\alpha$1 $\lambda$ = 1.5406 Å).

**Figure 2.3:** Digital images of Shimadzu X-ray diffractometer used in this research.

### 2.3.3. X-ray Photoelectron Spectroscopy

X-ray Photoelectron Spectroscopy was used to study the elemental chemical states, the chemical composition, the atomic weight percentage, and the binding energy of the as-prepared samples. The surface investigation of all materials was conducted using X-rays. First, an X-ray beam hit the material, and then the X-ray induced the excited electrons from the inner shell electrons, which are called "photo-emitted electrons." The detector probed the kinetic energy of photo-emitted electrons to generate the spectrum of all samples. All measurements were conducted under vacuum conditions, and XPS were collected using a Kratos Axis Ultra DLD spectrometer with a non-monochromatic Al Kα x radiation and a beam size of ~ 1 mm (hν = 1486.6 eV). The curve fitting and quantitative analysis were obtained by measuring the area under the elemental and synthesized peaks. The binding energy of various core levels was determined by fitting the recorded spectra with Gauss-Lorentz curves. The data was analysed using the NIST XPS database for peak assignment.
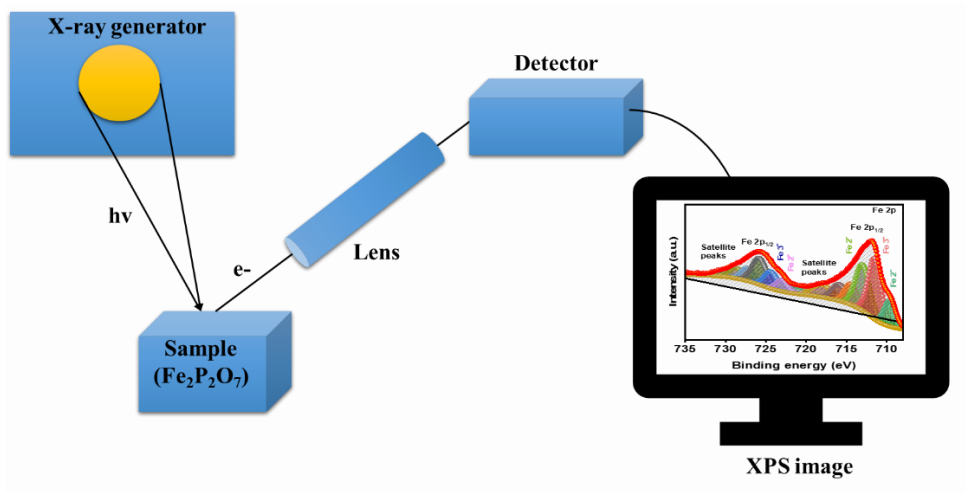
**Figure 2.4:** Schematic of XPS.

### 2.3.4. Fourier Transform Infrared Spectroscopy

Fourier Transform Infrared Spectroscopy was used to study the chemical bonds in a molecule by producing an infrared absorption spectrum. It is considered one of the useful analytical techniques for confirming the identity of organic, polymeric, and in some cases inorganic compounds and composites. FT-IR uses a Michelson interferometer working principle, where the interferometer creates a beam of different frequencies of light at once, and then that beam strikes the sample, determining how much of that beam is absorbed by the sample to construct an interferogram as the raw signal. The FT-IR spectrum is obtained on the system screen, comprised of infrared light absorbance by the substance on the vertical axis and the frequency (wavelength) on the horizontal axis. The FT-IR spectrum of all the synthesized samples was obtained by using the PerkinElmer Spectrum Two FT-IR Spectrophotometer.
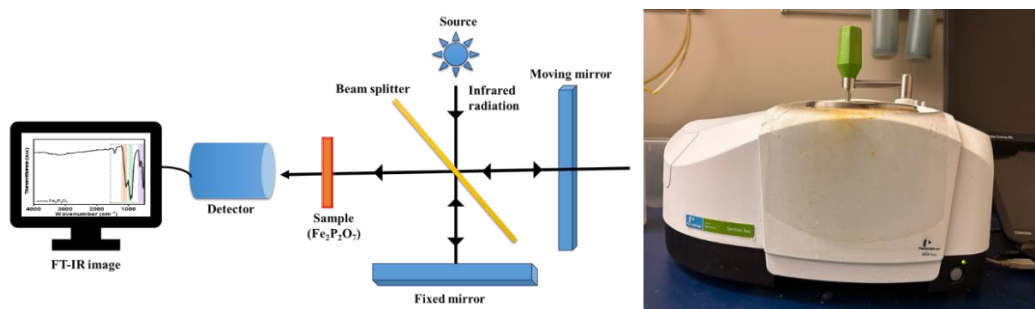
**Figure 2.5:** Schematic of FT-IR and the digital image of PerkinElmer Spectrum Two FT-IR spectrophotometer used in this research.

## 2.4. Electrochemical characterization

All electrochemical tests were accomplished at room temperature in a PARSTAT MC electrochemical workstation (Princeton Applied Research, USA) in conventional three-electrode systems. Three electrode systems consist of working, counter, and reference electrodes. First, a working electrode was already prepared by growing metal pyrophosphates on Ni-foam after 12 h. Platinum wire (Pt) was used as a counter electrode, and saturated calomel electrode (SCE) or Hg/HgO was used as a reference electrode for the study of its performance in water splitting and its characteristics as a supercapacitor, respectively. The potentiodynamic and electrochemical supercapacitor study was conducted based on surface area consideration as the material directly grown on Ni-foam and mass-loading of material on Ni-foam was not considered for this purpose of study. However, mass loading is an important parameter during electrochemical investigations therefore, we have measured mass-loading of the material on the Ni-foam. The mass-loading of $Ni_2P_2O_7$, $Co_2P_2O_7$, and $Fe_2P_2O_7$ are 26.3, 31.8, and 21.9 mg/cm$^2$, respectively. For the potentiodynamic study as an electrocatalyst, linear sweep voltammetry (LSV), chronoamperometry (CA), and

16

electrochemical impedance spectroscopy (EIS) measurements were performed in 1 M

KOH electrolyte. All measured potentials were converted to the reversible hydrogen

electrode (RHE). In that perspective, the LSV was carried out after iR compensation

using the formula: $E_{RHE} = E_{Hg/HgCl_2} + 0.059 * pH - iR$ (iR for $Fe_2P_2O_7$, $Co_2P_2O_7$,

and $Ni_2P_2O_7$ is 0.015, 0.064, and 0.065 V, respectively). In the case of supercapacitor

testing, cyclic voltammetry (CV), galvanostatic charge-discharge (GCD)

measurements, and durability tests over 5,000 cycles were employed in 3 M KOH

media for the analysis of energy storage properties.
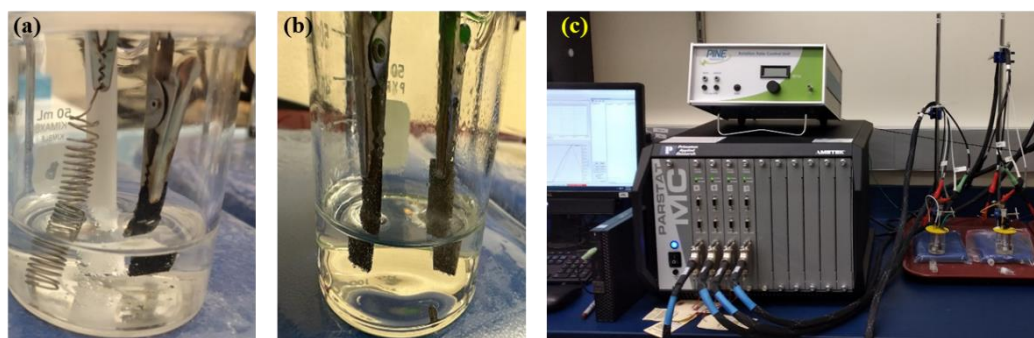


**Figure 2.6:** Images of (a) 3 electrode configurations, (b) 2 electrode configurations,

and (c) the digital image of PARSTAT MC electrochemical workstation used in this

research.

# CHAPTER III

# RESULTS AND DISCUSSION

## 3.1 Structure characterization

### 3.1.1 Field-Emission Scanning Electron Microscopy

The morphology of the as-prepared composites $Fe_2P_2O_7$, $Co_2P_2O_7$, and $Ni_2P_2O_7$, were observed under FESEM or ordinarily known as SEM, as shown in **Figure 3.1.** A similar pattern of morphology was noticed for the prepared materials. Firstly, the powdered form of the prepared composites was investigated by SEM technique, and it found that the morphology of composites comprised of microplates and agglomerated nanoparticles with non-homogeneous sizes of 15 to 1 μm of $Fe_2P_2O_7$, $Co_2P_2O_7$, and $Ni_2P_2O_7$ microparticles. Further, SEM-EDX mapping was carried out at 10 μm to analyze the composition of the prepared samples. The results indicated that the images taken under the $Fe_2P_2O_7$, $Co_2P_2O_7$, and $Ni_2P_2O_7$ samples have corresponding elements, as shown in the right inset figure of **Figure 3.1** and the respective EDX of the samples were illustrated in **Figure 3.2**. Furthermore, to gain a better understanding of the microstructure of the as-prepared materials, the SEM of $Fe_2P_2O_7$, $Co_2P_2O_7$, and $Ni_2P_2O_7$ grown on Ni-foam were taken at different magnifications before electrochemical testing as well as accounted elemental mapping and EDX analysis for the same in **Figure 3.3**, **3.4**, and **3.5**, respectively. Close observations of the SEM revealed a similar 3D microplate-like structure engineered on the Ni-foam for all three prepared samples.
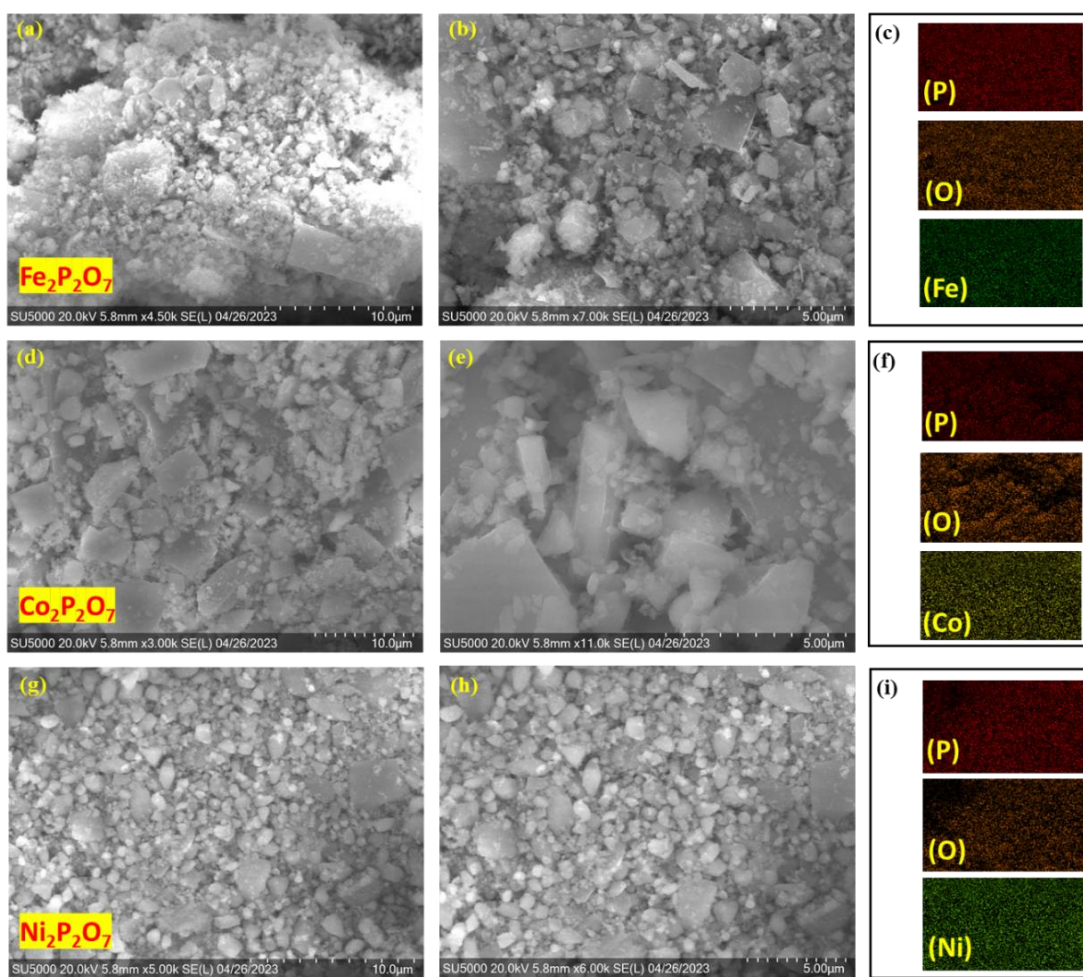
**Figure 3.1:** SEM images of powdered (a-b) $Fe_2P_2O_7$, (d-e) $Co_2P_2O_7$, and (g-h) $Ni_2P_2O_7$, Elemental mapping at 10 μm of (c) P, O, and Fe for $Fe_2P_2O_7$, (f) P, O, and Co for $Co_2P_2O_7$, and (i) P, O, and Ni for $Ni_2P_2O_7$.
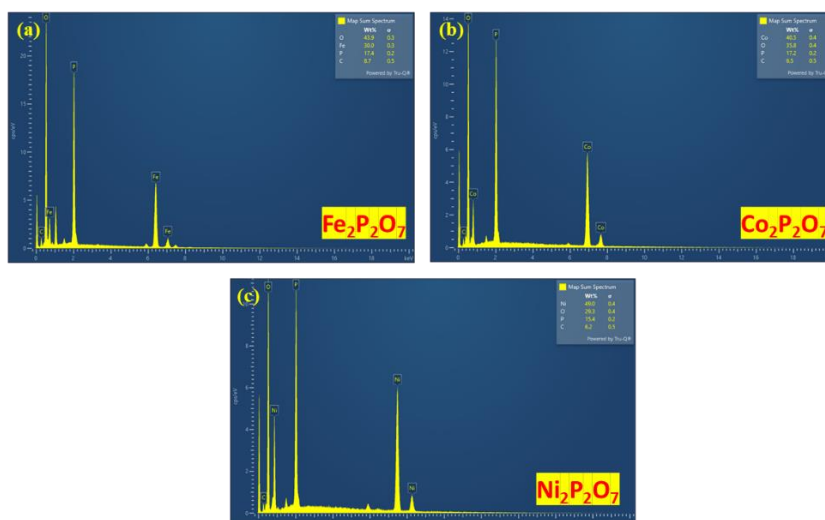
**Figure 3.2:** EDX analysis (20 kV) of (a) Fe, P, and O emission lines for $Fe_2P_2O_7$, (b) Co, P, and O emission lines for $Co_2P_2O_7$, and (c) Ni, P, and O emission lines for $Ni_2P_2O_7$.
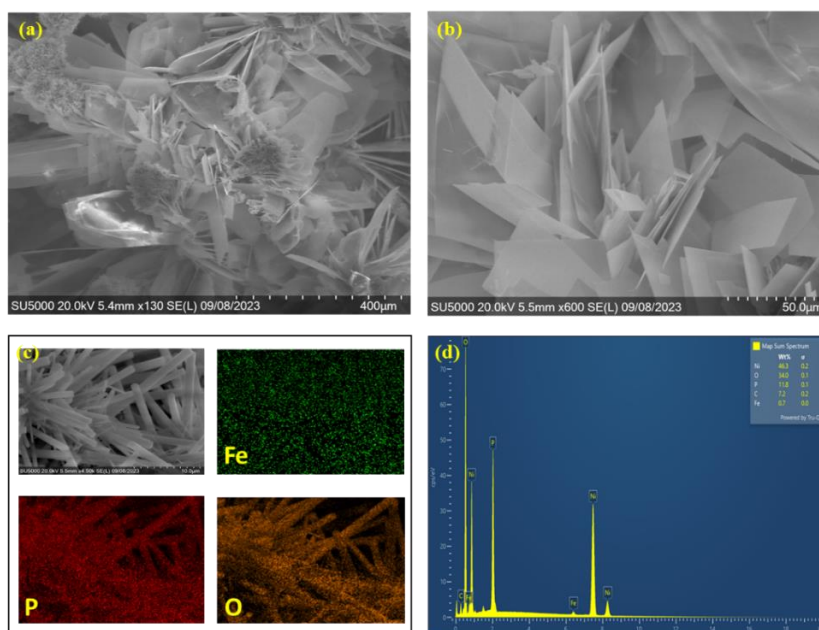


**Figure 3.3:** SEM images of grown $Fe_2P_2O_7$ on Ni-foam before testing (a) at 400 μm, (b) at 50 μm, (c) enlarged SEM image of $Fe_2P_2O_7$ and elemental mapping (20 kV) of Fe, P, and O, and (d) EDX analysis of Fe, P, and O emission lines for $Fe_2P_2O_7$.
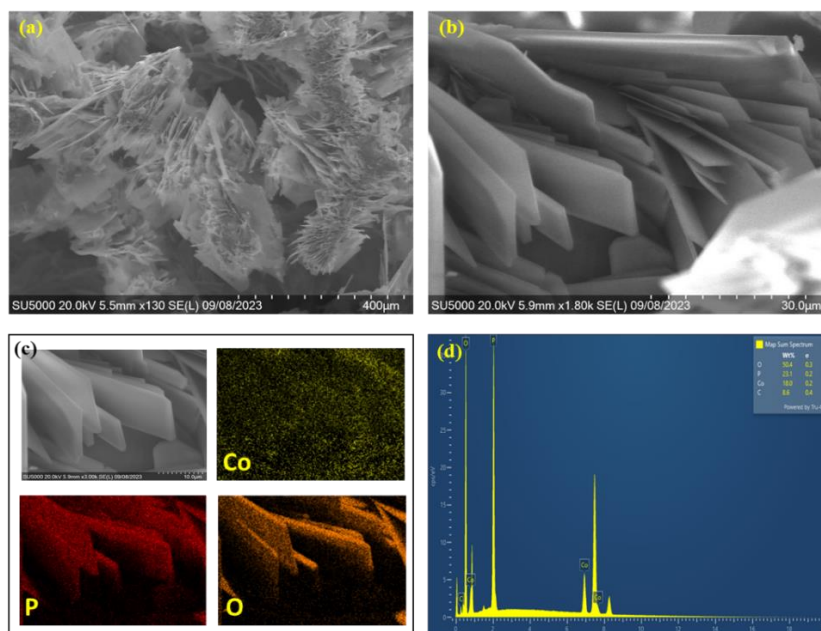
**Figure 3.4:** SEM images of grown $Co_2P_2O_7$ on Ni-foam before testing (a) at 400 μm, (b) at 30 μm, (c) enlarged SEM image of $Co_2P_2O_7$ and elemental mapping (20 kV) of Co, P, and O, and (d) EDX analysis of Co, P, and O emission lines for $Co_2P_2O_7$.
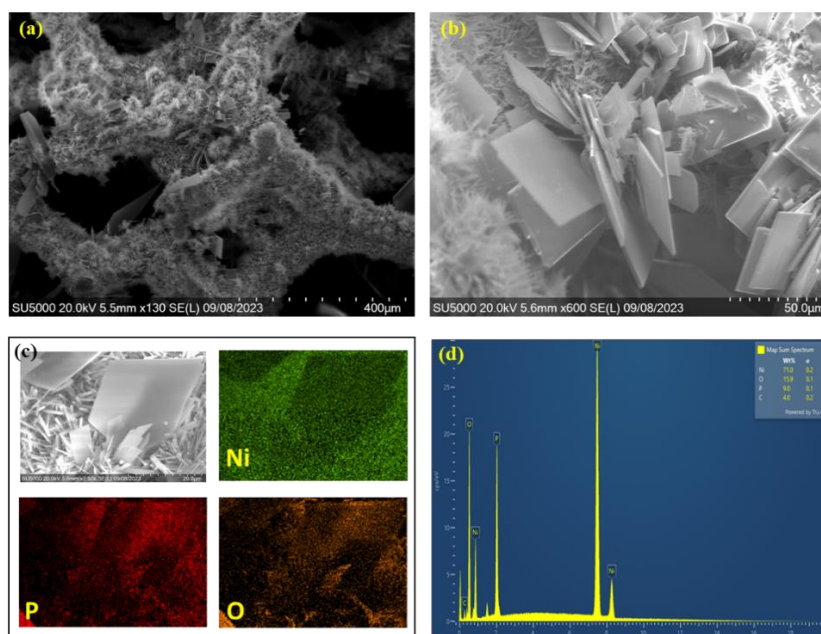


**Figure 3.5:** SEM images of grown $Ni_2P_2O_7$ on Ni-foam before testing (a) at 400 μm, (b) at 50 μm, (c) enlarged SEM image of $Ni_2P_2O_7$ and elemental mapping (20 kV) of Ni, P, and O, and (d) EDX analysis of Ni, P, and O emission lines for $Ni_2P_2O_7$.

*3.1.2 X-ray Diffraction*

The Structural changes, phase purity, crystallinity, and crystal structure of the prepared $Fe_2P_2O_7$, $Co_2P_2O_7$, and $Ni_2P_2O_7$ composites were carried out by the powder X-ray diffraction measurement as enumerated in **Figure 3.6**. It can be obvious from the XRD paradigm of amorphous $Fe_2P_2O_7$ that the diffraction peaks at particular intensities are associated with 28.9º, 29.7º, 32.8º, 35.3º, and 36.8º correspond to (101), (011), (-120), (-210), and (220) planes, respectively, reflecting triclinic distortion of the form $Fe_2P_2O_7$ (JCPDS#00-72-1516) [44–48]. Likewise, Li et al. [47] also prepared a low crystalline $Fe_2P_2O_7$ nanoplates-like structure by adopting interfacial engineering, where the semicrystalline nature of $Fe_2P_2O_7$ provides better surface area and more active sites towards the electrochemical surface phenomenon. Moreover, the main characteristic diffraction peaks of the $Co_2P_2O_7$ lie at 2θ between 15º and 50º, the obvious diffraction peaks that can be indexed to (JCPDS#00-034-1378) (210), (002), (20-2), (311), (022), (40-2), (420), (402), and (232) planes of monoclinic crystal structure [25,49–51]. Similarly, Chang et al. [25] reported nanocrystals of $Co_2P_2O_7$ through polymer gelation towards water oxidation and emphasized the monoclinic phase of $Co_2P_2O_7$ XRD. Further, the $Ni_2P_2O_7$ best matches the indexed pattern of JCPDS #00-039-0710 and has good agreement with lattice constant parameters (a = 8.823 Å, b = 8.291 Å, and c = 8.961 Å [52,53]. The diffraction peaks at 18.9, 21.3, 24.8, 26.8, 28.1, 32.2, 34.7, 36.1, 39.7, 43.0, 44.6, and 48.6 are assigned to (110), (10-2), (21-1), (120), (11-2), (130), (321), (420), (102), (032), (33-2), and (42-4) planes, respectively, illustrating the formation of a phase pure monoclinic crystal system [54–56]. The XRD line indicates a good crystallinity for the agglomerated nanoparticles of $Ni_2P_2O_7$ obtained at 180º C after 12 hours. Pang et al. [57] synthesized the nickel pyrophosphate microstructures at different temperature ranges from 350-700º C and could not obtain a pure crystalline

phase. However, in this study, we have grown $Ni_2P_2O_7$ on Ni-foam with a pure crystalline phase. The XRD data of all the synthesized samples revealed no impurity peaks, implying that we successfully prepared the transition metal-based pyrophosphates.
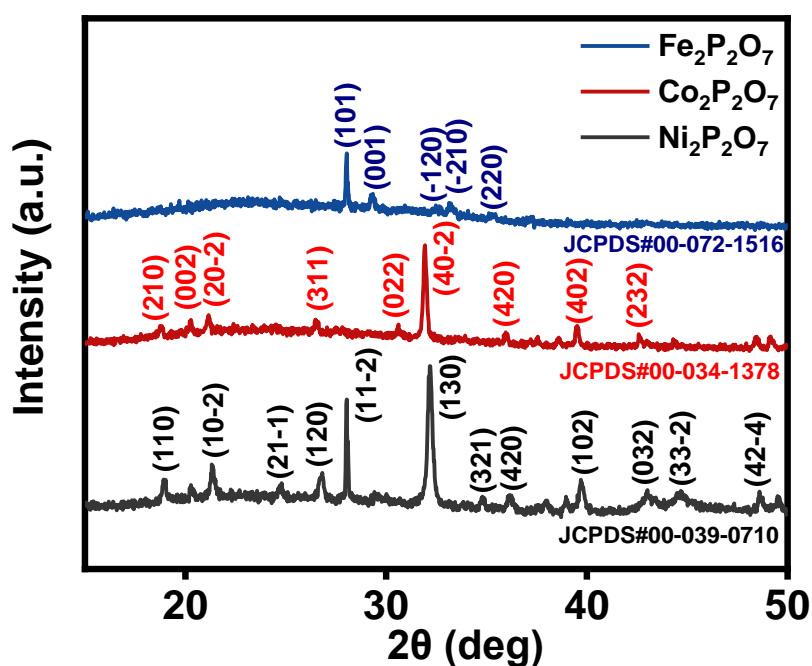


**Figure 3.6:** XRD spectra of $Fe_2P_2O_7$, $Co_2P_2O_7$, and $Ni_2P_2O_7$.

### 3.1.3 X-ray Photoelectron Spectroscopy

Subsequently, to understand the surface composition, elemental configuration, and chemical valence states of the as-synthesized materials, the X-ray photoelectron spectroscopy was adopted, and the Gaussian fitting approach was further employed to analyze the attributable peaks of the prepared samples. **Figure 3.7** delineates, the XPS broad spectrum of $Fe_2P_2O_7$, $Co_2P_2O_7$, and $Ni_2P_2O_7$ composites, the presence of Fe, P, and O elements indicates the formation of $Fe_2P_2O_7$, as well as the existence of Co, P,

and O elements reflects the presence of $Co_2P_2O_7$, and the survey spectrum of $Ni_2P_2O_7$ indicated the presence of Ni, P, and O elements in the composite. Hence, the survey spectrum illustrated the main constituent elements present in the obtained composites. Further, to dig more about chemical valence states and bonding, the high-resolution XPS was accompanied.
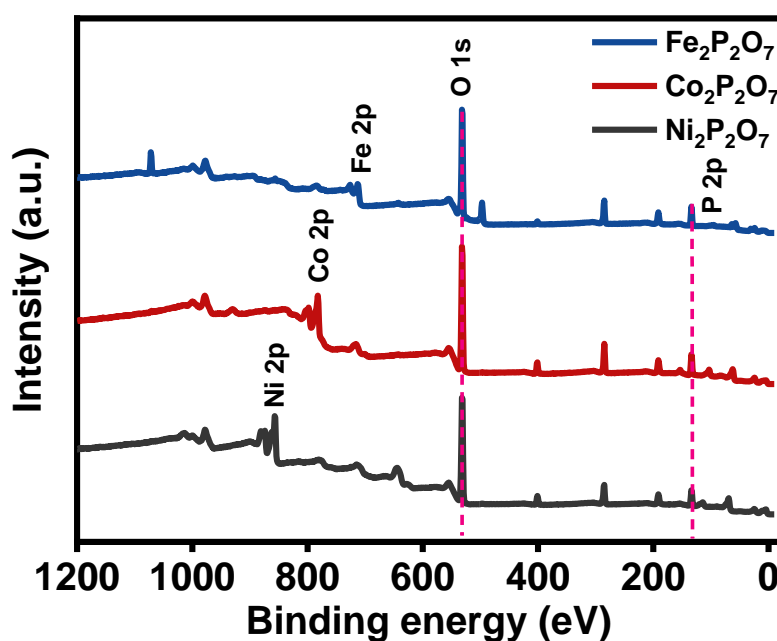


**Figure 3.7:** XPS survey spectra of $Fe_2P_2O_7$, $Co_2P_2O_7$, and $Ni_2P_2O_7$.

The defined deconvoluted Ni 2p spectrum as shown in **Figure 3.8a** of a $Ni_2P_2O_7$ specifies two significant peaks observed at 856.4 and 874.1 eV attributed to Ni $2p_{3/2}$ and Ni $2p_{1/2}$, respectively, spin orbitals splitting into $Ni^{2+}$ and $Ni^{3+}$ species. At high binding energy, $Ni^{2+}$ dominates the presence of nickel species [58–60]. The peaks located at 862.9 and 880.4 eV correspond to shakeup satellite peaks, suggesting that the Ni is mainly in the state of $Ni^{2+}$. **Figure 3.8b** shows the P 2p peak centered at a binding energy of 134.3 and 133.3 eV, attributing that +5 and highly oxidized phosphorous species $(P_2O_7)^{4-}$, phosphate states for P elements, respectively [61,62]. Further, O 1s

spectrum (**Figure 3.8c**) was deconvoluted in two Gaussian distended peaks at 531.2 and 532.5, resembling the metal-oxide bond (P-O) and oxygen ions in low coordination at surface and metal oxide (Ni-O), respectively [63]. Thus, it confirms the presence of Ni, P, and O elements concerning the chemical bonding and structure of $Ni_2P_2O_7$. **Figure 3.8d** enumerates the high-resolution spectra of Co 2p which bifurcated into two prominent peaks of Co $2p_{3/2}$ at 781.6 eV with other two spin-orbital of $Co^{3+}$ (781.4 eV) and $Co^{2+}$ (782.8 eV) and Co $2p_{1/2}$ at 797.5 eV which deconvoluted into $Co^{2+}$ at 801.2 eV and $Co^{3+}$ 798.2 eV spin-orbit splitting values [25,64]. As per the P 2p spectrum shown in **Figure 3.8e**, the peaks at binding energy 133.4 and 134.4 eV correspond to P $2p_{3/2}$ and P $2p_{1/2}$, respectively, proving the existence of P (5+) in Cobalt pyrophosphate [64,65]. The role of O and its existence in the chemical structure and valence states was confirmed from the XPS of O 1s (**Figure 3.8f**) where, surface absorbed hydroxyl groups (OH) at 532.8 eV, lattice oxygen at 531.5 eV and low coordination of metal-oxide (Co-O) at 530.9 eV [51]. These outcomes support the successful formation of the $Co_2P_2O_7$ composite. Simultaneously, the XPS of $Fe_2P_2O_7$ was obtained. **Figure 3.8g** illustrates the Fe 2p pattern which can be convoluted to $Fe^{2+}$ ($2p_{3/2}$ at 710.1 and 714.1 eV, and $2p_{1/2}$ at 724.1 eV) and $Fe^{3+}$ ($2p_{3/2}$ at 711.6 eV and $2p_{1/2}$ at 726.3 eV), and respective satellite peaks [66]. The high-resolution spectra of P 2p (**Figure 3.8h**) and O 1s (**Figure 3.8i**), indicate the presence of $P^{5+}$ (P-O-Fe at 134.3 eV and $(P_2O_7)^{4-}$ at 133.4 eV) and oxygen group (chemisorbed hydroxyl group at 532.9 eV and metal-oxide group at 531.3 eV), respectively [67,68]. Hence, the findings from the XPS convey the effective formation of $Fe_2P_2O_7$ composite.
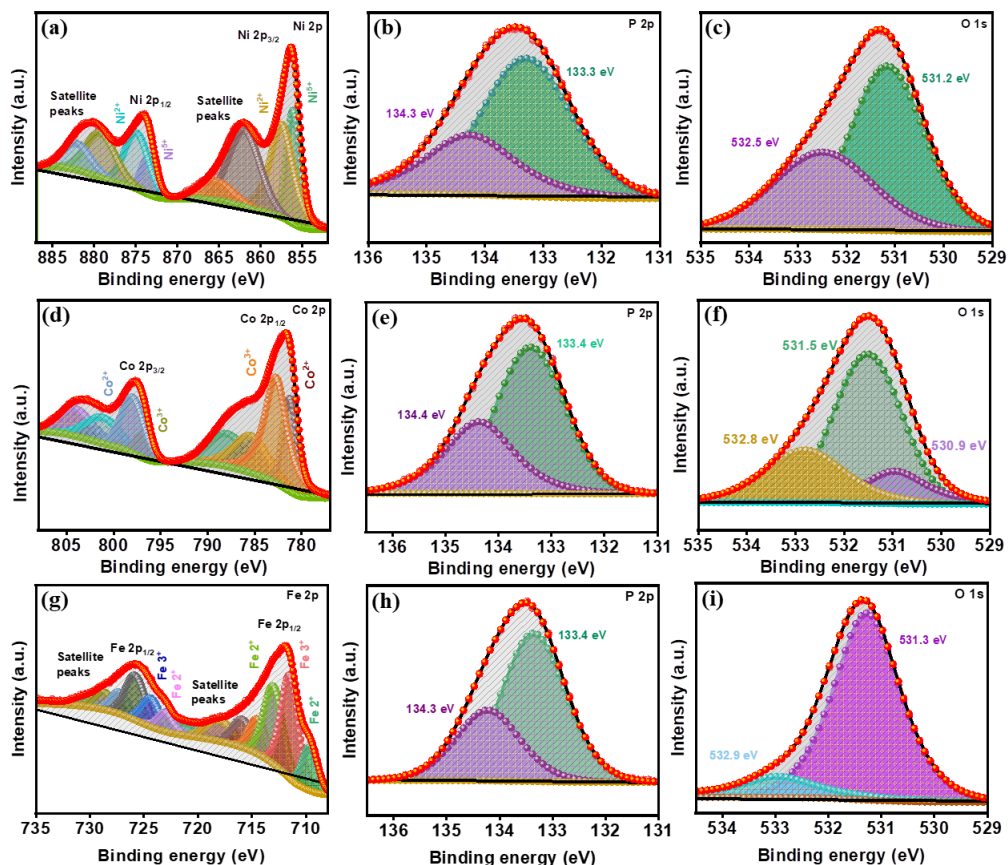
**Figure 3.8:** High-resolution XPS spectra of (a) Ni 2p, (b) P 2p, (c) O 1s of $Ni_2P_2O_7$, (d) Co 2p, (e) P 2p, (f) O 1s of $Co_2P_2O_7$, and (g) Fe 2p, (h) P 2p, (i) O 1s of $Fe_2P_2O_7$.

### 3.1.4 Fourier Transform Infrared Spectroscopy

Fourier transform infrared spectroscopy spectra (**Figure 3.9**) of as-fabricated samples were collected to reconfirm the possible existing bonds, which are identical to those of metal-pyrophosphate ($M_2P_2O_7$, M = Cu, Co, Ni, Ca, Cd, Fe, Mn) [69]. The pyrophosphate group frequencies can be allocated to characteristic peaks of the $PO_3$ group and P-O-P bridge [70]. The band from 1600 to 500 $cm^{-1}$ typically displays the region of pyrophosphates. The P-O-P bridge vibration is observed around 946 $cm^{-1}$ [71]. The asymmetric and symmetric absorption peaks at 1098, and 1065 indicates $PO_3$ stretching frequencies. The binding modes of $PO_3$ have been seen in the very weak

vibration range of 601-515 cm$^{-1}$, where M-O stretching usually appears [72]. The appearance of a strong P-O-P band is known to be the most important attribute of pyrophosphate spectra [71]. The FT-IR and XPS results are consistent with XRD, suggesting the crystal structure with pyrophosphate group and successful formation of $Ni_2P_2O_7$, $Co_2P_2O_7$, and $Fe_2P_2O_7$ samples.
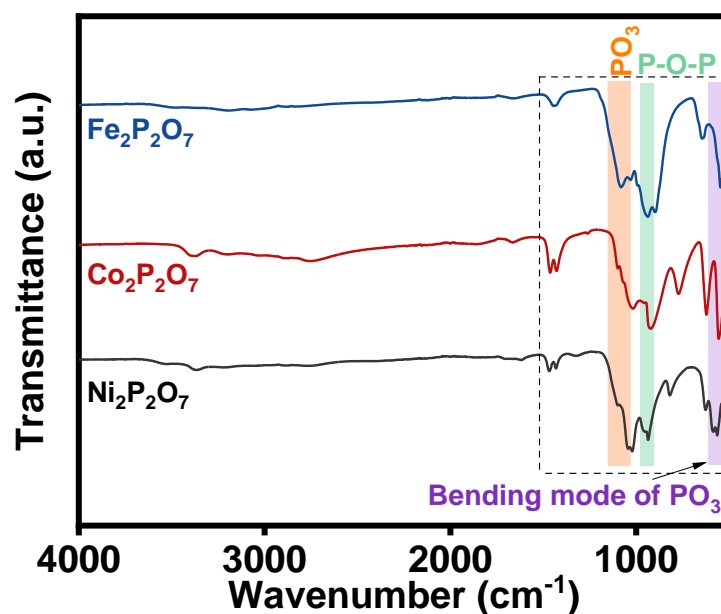


**Figure 3.9:** FT-IR spectra of $Fe_2P_2O_7$, $Co_2P_2O_7$, and $Ni_2P_2O_7$.

## 3.2 Electrochemical measurements

### 3.2.1 Electrocatalytic Performance towards Hydrogen Evolution Reaction

The electrocatalytic attributes of the as-prepared composites ($Fe_2P_2O_7$, $Co_2P_2O_7$, and $Ni_2P_2O_7$) were analyzed, and the linear sweep voltammetry measurement was carried out in 1 M KOH electrolyte to investigate the catalytic behavior towards HER. To reduce the chances of capacitive current a slow scan rate of 2 mV/s was adopted to observe the indispensable information from the polarization curve. **Figure 3.10a** shows the typical HER polarization curves for $Co_2P_2O_7$, $Ni_2P_2O_7$, and $Fe_2P_2O_7$

composites, demonstrating overpotential 268 mV, 241 mV, and 219 mV, respectively, at an accepted benchmark current density of 10 mA/cm$^2$ to distinguish the catalytic activity of the composites. The overpotential at lower and higher current density was also recorded as depicted in **Figure 3.10b** where, the overpotential required at 5 mA/cm$^2$ for $Co_2P_2O_7$, $Ni_2P_2O_7$, and $Fe_2P_2O_7$ is 229 mV, 200 mV, and 179 mV, respectively. Whereas the overpotential at a current density of 50 mA/cm$^2$ for $Co_2P_2O_7$, $Ni_2P_2O_7$, and $Fe_2P_2O_7$ is 346 mV, 311 mV, and 285 mV vs RHE, respectively, revealing $Fe_2P_2O_7$ shows a distinctive decrease in overpotential at a different current density, which enhances the catalytic activity among other samples. Further, $Fe_2P_2O_7$ was compared with the bare Ni foam and Pt/C deposited electrode (**Figure 3.10c**). Pt/C-based electrode is considered an ideal electrode material for HER activity. Pt/C (25 mV) was markedly lower overpotential, but bare Ni foam possess higher overpotential of 285 mV than $Fe_2P_2O_7$. Besides, it was noticeable that $Fe_2P_2O_7$ represents superior HER electrocatalyst than other reported catalysts which are tabulated in **Table 3.1**. Furthermore, to understand the HER kinetics Tafel slope of the as-prepared composites was plotted from LSV Curves in **Figure 3.10d** depending on the equation (3.1) [73–75], which is elucidated as a rate-determining step where alkaline HER process obeys classical Volmer-Heyrovsky route ($H_2O + e^- \rightarrow H_{ads} + OH^-$), representing the intrinsic attribute of the catalysts and could be assist to probe the fundamental steps involved in the $H_2$ production process [76].

$$\eta = a + b \log j \tag{3.1}$$

where $\eta$ is a overpotential, a is a constant, b is the Tafel slope, and j is the current density. The Tafel slope of $Fe_2P_2O_7$ of 87 mV/dec is significantly lower than those of $Co_2P_2O_7$ (110 mV/dec) and $Ni_2P_2O_7$ (105 mV/dec), implying that $Fe_2P_2O_7$ could effectively speed up the dynamic process. However, the Tafel slope is inversely related

to the charge transfer coefficient, which signifies the swift transfer of the electrons due to the reduction of free energy barrier for the electrochemical reaction. Thus, the charge transfer coefficient was calculated by using equation (3.2) [77–79].

$$b = 2.303RT/\alpha nF \tag{3.2}$$

where R stands for universal gas constant, T symbolizes absolute temperature, $\alpha$ corresponds to charge transfer coefficient (values lie between 0 and 1), n signifies number of electrons (n = 2 for HER), and F is the Faraday constant. The smaller the Tafel slope, the higher the charge transfer coefficient, and the more outstanding catalytic performance. The charge transfer coefficient for $Co_2P_2O_7$, $Ni_2P_2O_7$, and $Fe_2P_2O_7$ is 0.26, 0.28, and 0.34. In that sense, $Fe_2P_2O_7$ offers better kinetics than other samples.
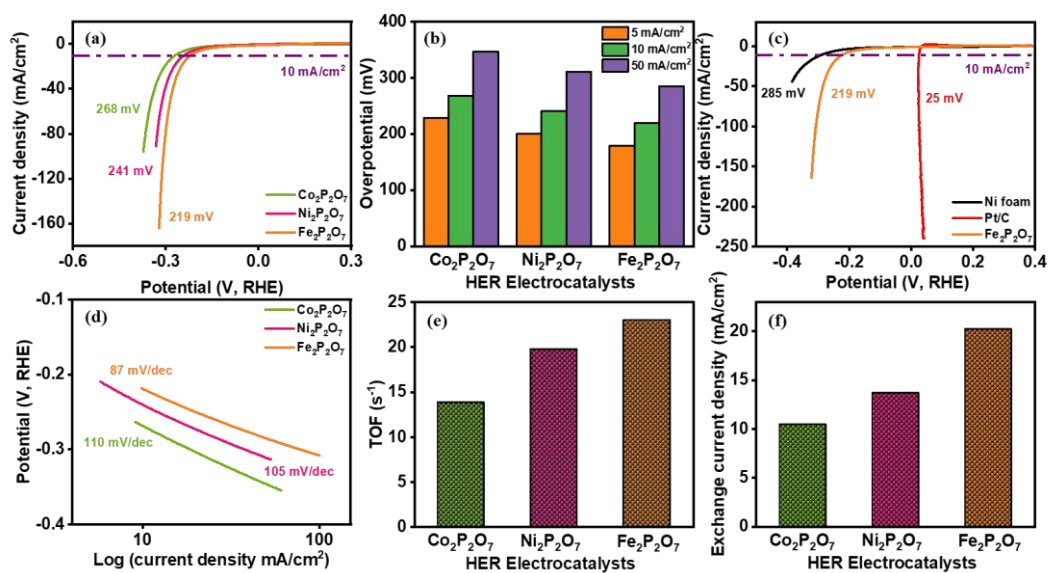


**Figure 3.10:** Electrocatalytic performance for HER: (a) LSV curve of the $Co_2P_2O_7$, $Ni_2P_2O_7$, and $Fe_2P_2O_7$ comparing overpotential at 10 mA/cm², (b) comparison of overpotential at 5 mA/cm², 10 mA/cm², and 50 mA/cm² for all the prepared samples,

(c) LSV curve of Ni-foam, Pt/C, and $Fe_2P_2O_7$ electrode, (d) Tafel slopes, (e) TOF at

an overpotential of 100 mV, and (f) Exchange current density.

To manifest the comparison on the limiting step of kinetics and corroborating comprehensive kinetic behavior of the electrocatalysts, further investigation has been carried out by employing Turnover frequency (TOF) as displayed in **Figure 3.10e** which is one of the crucial parameters to determine how rapidly a catalyst can catalyze the electrochemical reaction. Water splitting catalytic activity obeys pseudo-first-order kinetics, thereby, TOF is calculated per unit time by using equation (3.3) [80] at a specific overpotential of 100 mV.

$$TOF = jN_a/nF\tau \tag{3.3}$$

where $N_a$ is Avogadro's number, and $\tau$ is the surface concentration of active sites or the number of participating atoms in the catalyst material. The results suggested the acquisition of a TOF value of 23.02 $s^{-1}$ by $Fe_2P_2O_7$, which is much higher compared to $Co_2P_2O_7$ (13.85 $s^{-1}$) and $Ni_2P_2O_7$ (19.76 $s^{-1}$). In this perspective, lower overpotential of $Fe_2P_2O_7$ corresponds with the higher rate of TOF showcasing that amorphous nature of $Fe_2P_2O_7$ exercised excellent catalytic activity and efficient charge transfer process improving kinetics. therefore, the readiness of the electrode is required to be analyzed hence exchange current density was calculated using equation (3.4), where charge transfer resistance ($\Theta$ at 0 V) at the electrode-electrolyte interface is taken into account, and A is the geometrical area of the electrode which determines the flow of current density in each direction at equilibrium [81,82].

$$Exchange\ current\ density = RT/nF\theta A \tag{3.4}$$

The exchange current density of $Co_2P_2O_7$, $Ni_2P_2O_7$, and $Fe_2P_2O_7$ is 10.46, 13.68, and 20.22 $mA/cm^2$ as illustrated in **Figure 3.10f**, indicating $Fe_2P_2O_7$ has a faster

reaction and more active sites due to higher exchange current density. Moreover, to check the practical applicability of the electrocatalysts, a durability test was performed using linear sweep voltammetry. The HER LSV curve for all the samples after 10,000 CV cycles is illustrated in **Figure 3.11(a-c)**. All the samples displayed negligible fluctuation and cycle 1 overlaps with cycle 10,000, demonstrating their significant stability during the HER process.
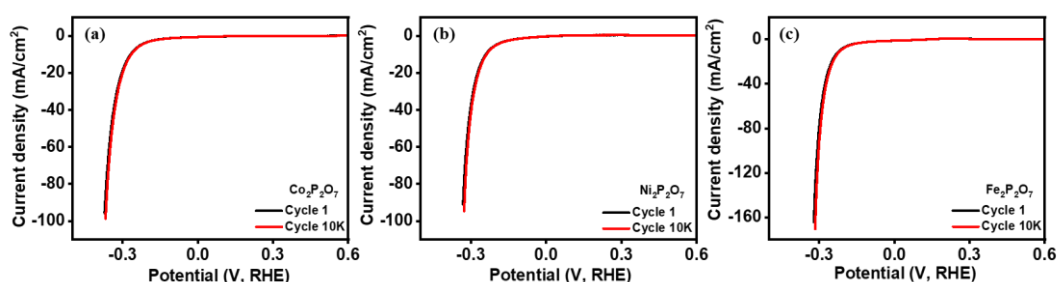


**Figure 3.11:** LSV curves after and before 10,000 cycles of cyclic voltammetry for $Co_2P_2O_7$, $Ni_2P_2O_7$, and $Fe_2P_2O_7$ samples.

**Table 3.1:** Comparison of the previously reported electrocatalysts for HER

| Electrocatalysts | Electrolyte | Overpotential (mV) @ 10 mA/cm$^2$ | Tafel slope (mV/dec) | References |
|---|---|---|---|---|
| FeP/CN | 1 M KOH | 235 | - | [83] |
| FeP | 1 M KOH | 221 | 134 | [84] |
| WS$_2$/RGO | 0.5 M H$_2$SO$_4$ | 265 | 58 | [85] |
| Cu$_2$MoS$_4$ | pH 0 H$_2$SO$_4$ | 321 | 95 | [86] |
| NiWS$_x$ | pH 7 PBS | 373 | 96 | [87] |
| MnNi-hydroxide | 1 M KOH | 231 | 110 | [88] |
| FeP/NF | 1 M KOH | 216 | 154 | [89] |
| Co$_3$S$_4$ | 1 M KOH | 266 | 200 | [90] |
| CoFe-S | 1 M KOH | 229 | 118 | [91] |
| **Co$_2$P$_2$O$_7$** | **1 M KOH** | **268** | **110** | **This Work** |
| **Ni$_2$P$_2$O$_7$** | **1 M KOH** | **242** | **105** | **This Work** |
| **Fe$_2$P$_2$O$_7$** | **1 M KOH** | **219** | **87** | **This Work** |

### 3.2.2 Electrocatalytic Performance towards Oxygen Evolution Reaction

The prepared samples have undergone electrocatalytic OER activity evaluation in 1 M basic electrolyte and were examined by LSV. A similar slow scan rate was chosen as selected for HER testing. In **Figure 3.12a**, at the current density of 10 mA/cm$^2$, the overpotential value for $Fe_2P_2O_7$ is 252 mV which is smaller than 270 mV of $Ni_2P_2O_7$ and 318 mV of $Co_2P_2O_7$ composite. Thus, the least overpotential provides the idea of producing a higher amount of $O_2$ bubbles from the surface of $Fe_2P_2O_7$. The overpotential at lower and higher current density was also recorded as described in **Figure 3.12b**, on the one hand, the overpotential required at 5 mA/cm$^2$ for $Co_2P_2O_7$, $Ni_2P_2O_7$, and $Fe_2P_2O_7$ are 299, 260, and 241 mV, respectively. On the other hand, the potential at a current density of 50 mA/cm$^2$ for $Co_2P_2O_7$, $Ni_2P_2O_7$, and $Fe_2P_2O_7$ are 364, 310, and 281 mV, respectively. As revealed from the polarization curve of as-synthesized samples, $Fe_2P_2O_7$ outlined its activity among the other than reported work such as Chondankar et al. [71] micro sheets of $Ni_2P_2O_7$ on Ni-foam possess 308 mV vs RHE overpotential at 10 mA/cm$^2$, Zhu et al. [51] fabricated sandwich structure of $Co_2P_2O_7/Ni(PO_3)_2@C$ with 279 mV at 10 mA/cm$^2$, later Yang et al. [92] prepared $CrFePO_4/NF$ requires overpotential of 280 mV at 10 mA/cm$^2$ of current density. Moreover, this conveys that the $Fe_2P_2O_7$ represents superior electrocatalytic OER performance relative to most of the other already reported benchmark electrocatalyst which are tabulated in **Table 3.2** for more precise differentiation. The catalytic activity of the best sample ($Fe_2P_2O_7$) was compared with the commercially ideal candidate $IrO_2$ which is regarded as the finest material to produce $H_2$ and $O_2$ after the dissociation of water. However, it is limited by fancy prices and scarce availability. However, iron-based material has attracted attention due to its tremendous availability and affordability. In addition, it shows comparatively significant results for OER, follows 2

or 4 e⁻ driven processes. Herein, the common reaction sequence of OER with iron-related materials is depicted below [93].

$$Fe^{2+}\text{-}OH + OH^- \rightarrow Fe^{3+}(O)\text{-}OH + H^+(aq) + e^- \tag{3.5}$$

$$Fe^{3+}(O)\text{-}OH + (OH)^-(aq) \rightarrow Fe^{2+}\text{-}OH + H^+(aq) + O_2(g) + e^- \tag{3.6}$$
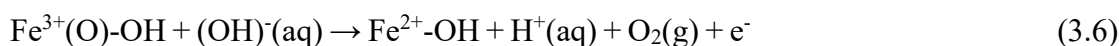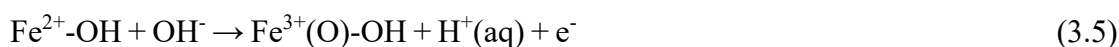
**Figure 3.12c** demonstrates the LSV curves of Ni foam, $IrO_2$, and $Fe_2P_2O_7$ where, $Fe_2P_2O_7$ exhibited a significant decrease in overpotential of only 252 mV at 10 mA/cm² and acquired the highest current density of 161.7 mA/cm², markedly improvised performance than bare Ni foam (390 mV at 10 mA/cm² and achieved a highest current density of 29.4 mA/cm²), and $IrO_2$ (296 mV at 10 mA/cm² and acquired a highest current density of 142.8 mA/cm²). In that sense, $Fe_2P_2O_7$ showed excellent catalytic activity towards OER.
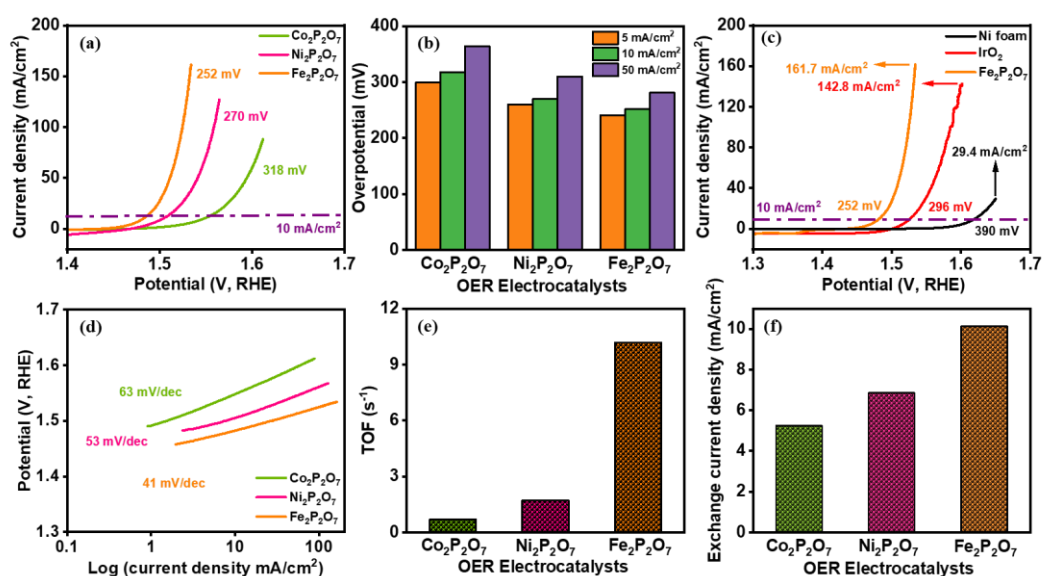


**Figure 3.12:** Electrocatalytic performance for OER: (a) LSV curve of the $Co_2P_2O_7$, $Ni_2P_2O_7$, and $Fe_2P_2O_7$ comparing overpotential at 10 mA/cm², (b) comparison of overpotential at 5 mA/cm², 10 mA/cm², and 50 mA/cm² for all the prepared samples,

(c) LSV curve of Ni-foam, $IrO_2$, and $Fe_2P_2O_7$ electrode, (d) Tafel slopes, (e) TOF at an overpotential of 100 mV, and (f) Exchange current density.

According to the literature, the OER process of metal-pyrophosphates in an alkaline medium involves a four-step proton coupled electron transfer reaction mechanism. Thus, the Butler-Volmer equation was employed to investigate the kinetics of the samples by deriving the Tafel slope from the polarization curve as enumerated in **Figure 3.12d** [94]. The Tafel slope of $Co_2P_2O_7$, $Ni_2P_2O_7$, and $Fe_2P_2O_7$ are 63, 53, and 41 mV/dec, respectively. The smaller Tafel slope of $Fe_2P_2O_7$ describes better charge transport kinetics and fast ion diffusion kinetics during water oxidation, which is consistent with the low overpotential in LSV. Additionally, the TOF of OER of the as-prepared samples is recapitulated in **Figure 3.12e** to make further evaluation of the dynamic nature of the OER process. $Fe_2P_2O_7$ yielded a TOF of 10.17 $s^{-1}$ at an overpotential of 100 mV, which was greater than $Ni_2P_2O_7$ (1.70 $s^{-1}$) and $Co_2P_2O_7$ (0.69 $s^{-1}$), demonstrating relatively superior catalytic performance. Similarly, the same trend was observed in a theoretically calculated charge transfer coefficient value of $Co_2P_2O_7$, $Ni_2P_2O_7$, and $Fe_2P_2O_7$ are 0.23, 0.27, and 0.36, respectively, conveying swift transfer of the electrons. To probe the charge transfer insight, a detailed investigation was considered. Those two important parameters in electrochemistry are exchanged current density and Electrochemical Impedance Spectroscopy (EIS). The exchange current density (**Figure 3.12f**) of $Co_2P_2O_7$, $Ni_2P_2O_7$, and $Fe_2P_2O_7$ are 5.23, 6.84, and 10.11 mA/cm$^2$, respectively. In that perspective, $Fe_2P_2O_7$ exhibits faster chemical reaction, transfer of current density in all possible directions at equilibrium, and conductivity.

Besides, the conductive nature and rate of charge transfer of the as-synthesized samples were observed through EIS testing. The Nyquist plot was encountered after

34

EIS as shown in **Figure 3.13(a-c)** of all the samples at various potentials ranging from 0.45, 0.5, 0.55, and 0.6 V. The impedance analysis was carried out in the frequency range from 10 kHz to 0.05 Hz at a 10 mV AC amplitude. The Nyquist plot showing a semicircular region at high frequency corresponds to the charge transfer resistance ($R_{ct}$) at the interface of electrode and electrolyte, where $R_{ct}$ is directly proportional to the kinetics and catalytic performance of the materials, so smaller the $R_{ct}$ refers to better passivity of ions and correlates to good electrical conductivity [95–99]. Moreover, a fitted Randles circuit as demonstrated in **Figure 3.13d** exaggerates the attribute of the Nyquist plot and after a thorough study of the circuit diagram and Nyquist plot at various potentials, it was noteworthy finding that $Fe_2P_2O_7$ showed the least charge transfer resistance among all the samples and over different potentials, tabulated in **Table 3.3**, confirming the improved kinetics, conductivity, and higher transfer of ions. The results indicated that micro sheets of $Fe_2P_2O_7$ showed improved sluggish behavior of 4 $e^-$ process of OER in the greatest degree. However, all the samples possess similar morphology. Thus, to assess the significance of surface area towards catalytic activity, electrochemical surface area (ECSA) testing was performed.
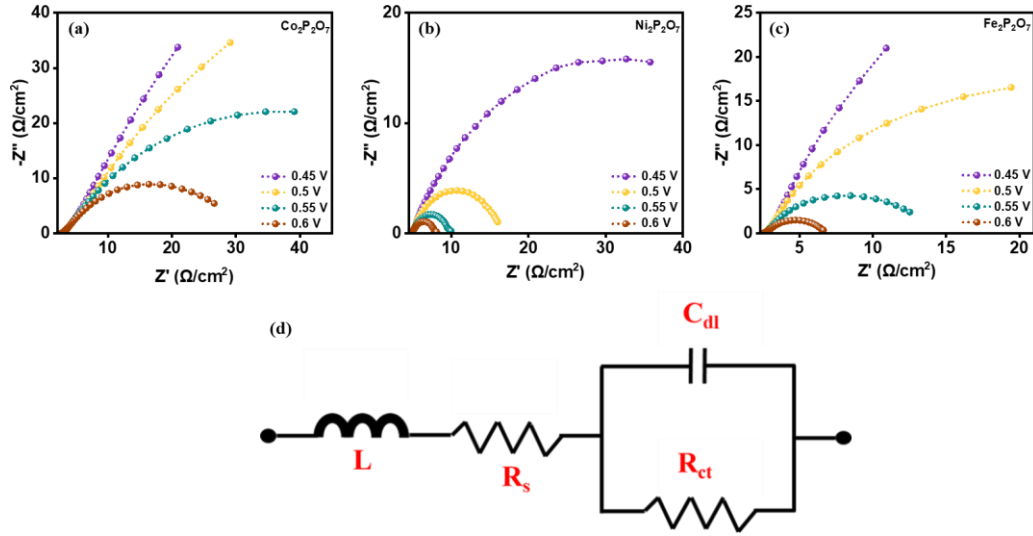
**Figure 3.13:** Nyquist plot of (a) $Co_2P_2O_7$, (b) $Ni_2P_2O_7$, and (c) $Fe_2P_2O_7$, and (d) Randle circuit according to Nyquist plot obtained for $Co_2P_2O_7$, $Ni_2P_2O_7$, and $Fe_2P_2O_7$.

ECSA was a thorough comprehension of the mechanism behind the nature of the electrocatalysts by developing CV in a non-faradic regime at various scan rates for the estimation of charging current. After careful analysis of the obtained CV, the electrochemical double layer capacitance ($C_{dl}$) value was calculated by incorporating charging current vs scan rate plot as shown in **Figure 3.14a** and equation (3.7) where, I is current, and v is scan rate [100].

$$I = vC_{dl} \tag{3.7}$$

$$ECSA = C_{dl}/C_s \; ; C_s = 0.04 \text{ mF/cm}^2 \tag{3.8}$$

$$RF = ECSA/GSA \tag{3.9}$$

$C_{dl}$ indicates ion adsorption on the surface of the catalyst. The value of $C_{dl}$ for $Co_2P_2O_7$, $Ni_2P_2O_7$, and $Fe_2P_2O_7$ is 12, 74, and 85 mF, respectively. In that sense, $Fe_2P_2O_7$ shows more ion interaction on the surface of the electrocatalyst thus it is important to investigate the active sites of the catalyst. Therefore, equation 3.8 was adopted to calculate the ECSA where $C_s$ is the specific capacitance [100]. Also, the

value of ECSA is proportional to the value of Cdl, the higher the $C_{dl}$ value, the higher the ECSA ensuring more active sites could be exposed on the surface of the catalysts and the more outstanding electrocatalytic activity. Thus, $Fe_2P_2O_7$ (2125 cm$^2$) showed much higher results than $Ni_2P_2O_7$ (1850 cm$^2$) and $Co_2P_2O_7$ (300 cm$^2$) as in **Figure 3.14b**. It may be anticipated that higher ECSA value exposed more active sites, thereby generating more $O_2$ and $H_2$ bubbles which in turn leads to enhanced catalytic activity. Equation 3.9 was utilized (where GSA is a geometric surface area) to evaluate the gas bubble dissipation efficiency by measuring the roughness factor (RF) as displayed in **Figure 3.14c** [100]. The RF value of $Co_2P_2O_7$, $Ni_2P_2O_7$, and $Fe_2P_2O_7$ is 461.53, 3775,51, and 4166.67, respectively. $Fe_2P_2O_7$ was computed to be incomparable with other samples, manifesting ideal potential for the release of excess amount of gas bubbles, which also correlate with enhanced $C_{dl}$, enriched ECSA, and augmented least $R_{ct}$. All these aspects together make $Fe_2P_2O_7$ a superior electrode, rather a catalyst of choice for water-splitting in the years to come. Moreover, XRD of $Fe_2P_2O_7$ reveals the amorphous nature which is advantageous for catalyst purposes. According to the literature, the amorphous material outlays more surface area, which in turn increases the absorption of reactants and desorption of gases, thus higher performance can be achieved [101].
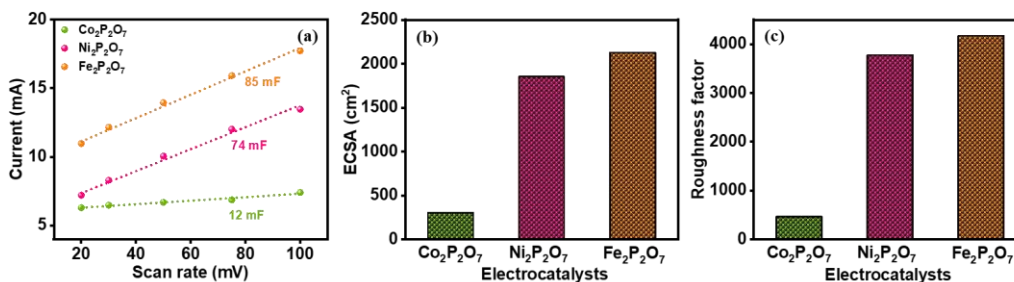
**Figure 3.14:** (a) Electrochemical double layer capacitance of $Co_2P_2O_7$, $Ni_2P_2O_7$, and $Fe_2P_2O_7$, (b) electrochemical surface area, and (c) Roughness factor of all as-synthesized samples.

Furthermore, the stability of the materials plays a crucial role in influencing the activity of the catalyst. Electrochemical 4 $e^-$ sluggish kinetics consistency is required for long-term running processes in a real-life application. The stability of OER of all as-prepared samples was examined and confirmed by steady polarization curves as portrayed in **Figure 3.15(a-c)** where cycle 1 overlaps with the cycle 10,000 polarization curve. Further, longevity was tested by long-term chronoamperometry test, herein shows the durable relationship between current density over time. Thereby, the CA is recorded as shown in **Figure 3.15(d-f)**, representing stability of all the as-synthesized composites at 0.65 V potential over 24 hours. The $Co_2P_2O_7$, $Ni_2P_2O_7$, and $Fe_2P_2O_7$ electrode's current density somewhat from 39.1, 47.2, and 114.6 to 23.6, 39.1, and 109.2 mA/cm$^2$ respectively. During the process it was observed that the current density drop fluctuated but it maintains the stable current density without an extreme deterioration. It was found that the $Fe_2P_2O_7$ has a least current density difference of 5.4 mA/cm$^2$ than $Ni_2P_2O_7$ (8.1 mA/cm$^2$) and $Co_2P_2O_7$ (15.5 mA/cm$^2$) after 24 hours. Additionally, a variation might be caused after 22 and 12 hours in $Ni_2P_2O_7$ and $Fe_2P_2O_7$, due to release and accumulation of bubbles produced by the water-splitting process. On the basis, $Fe_2P_2O_7$ possess eminent durability for OER application.
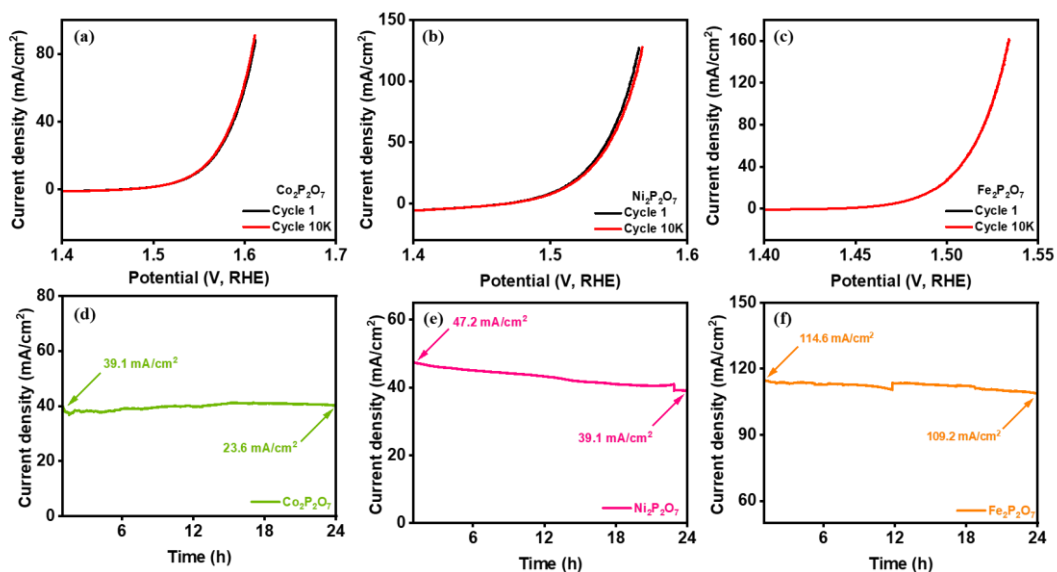
**Figure 3.15:** (a-c) Polarization curve stability over 10,000 cycles of all as-prepared samples, and (d-f) chronoamperometry test of $Co_2P_2O_7$, $Ni_2P_2O_7$, and $Fe_2P_2O_7$ catalysts towards OER.

**Table 3.2:** Comparison of the previously reported electrocatalysts for OER

| Electrocatalyst | Electrolyte | Overpotential (mV) @ 10 mA/cm$^2$ | Tafel slope (mV/dec) | Reference |
|---|---|---|---|---|
| $Fe_2B$ NMs/NF | 1M KOH | 276 | - | [102] |
| Mo-Ni-Se@NF | 1M KOH | 397 | - | [103] |
| FeP/$Ni_2P$ | 1M KOH | 154 | 23 | [104] |
| O-CoMoS | 1M KOH | 272 | 71 | [105] |
| $Co_{0.9}S_{0.58}P_{0.42}$ | 1M KOH | 266 | 48 | [106] |
| $NiSe_2$-$Ni_2P$/NF | 1M KOH | 249 | 45 | [107] |
| Gelled FeCoW/Au | 1M KOH | 191 | - | [108] |
| CoP | 1M KOH | 345 | 47 | [109] |
| NiFe LDH/Cu nanowire arrays | 1M KOH | 199 | 28 | [110] |
| $Ni_{1.5}Fe_{0.5}P$/CF | 1M KOH | 264 | 55 | [111] |
| $Co_2P$ | 1M KOH | 310 | 50 | [112] |
| N-$Ni_3S_2$/NF | 1M KOH | 260 | 70 | [113] |
| NiCoFeP/C | 1M KOH | 270 | 65 | [114] |
| FeP | 1M KOH | 320 | 51 | [115] |
| Iron oxide/phosphate | 1M KOH | 288 | 43 | [116] |

| | | | | |
|---|---|---|---|---|
| layer coated FeP | | | | |
| CoP NPs | 0.1M NaOH | 330 | 50 | [117] |
| Ni-P | 1M KOH | 344 | 49 | [118] |
| $(Co_{0.54}Fe_{0.46})_2P$ | 0.1M KOH | 370 | - | [119] |
| **$Co_2P_2O_7$** | **1M KOH** | **318** | **63** | **This Work** |
| **$Ni_2P_2O_7$** | **1M KOH** | **270** | **53** | **This Work** |
| **$Fe_2P_2O_7$** | **1M KOH** | **252** | **41** | **This Work** |

**Table 3.3:** Rct ($\Omega/cm^2$) comparison of $Co_2P_2O_7$, $Ni_2P_2O_7$, and $Fe_2P_2O_7$ at 0.45, 0.5,

0.55, and 0.6 V

| **Electrocatalyst** | **@0.45 V** | **@0.5 V** | **@0.55 V** | **@0.6 V** |
|---|---|---|---|---|
| $Co_2P_2O_7$ | 42.19 $\Omega/cm^2$ | 36.45 $\Omega/cm^2$ | 30.01 $\Omega/cm^2$ | 25.21 $\Omega/cm^2$ |
| $Ni_2P_2O_7$ | 13.27 $\Omega/cm^2$ | 11.02 $\Omega/cm^2$ | 5.14 $\Omega/cm^2$ | 3.30 $\Omega/cm^2$ |
| $Fe_2P_2O_7$ | 4.89 $\Omega/cm^2$ | 4.71 $\Omega/cm^2$ | 4.58 $\Omega/cm^2$ | 3.06 $\Omega/cm^2$ |

### 3.2.3 Overall water-splitting performance of $Fe_2P_2O_7$

Since the $Fe_2P_2O_7$ composite showed excellent bifunctional OER and HER performance, an electrocatalytic water-splitting device was built with $Fe_2P_2O_7$ sample serving as both anode and cathode (**Figure 3.16b**) to test its ability for practical application in water electrolyzer as a fuel cells. This is an alternative, renewable, and sustainable approach to produce products for a fuel and medical purposes. The results show that a sample of $Fe_2P_2O_7$ can faithfully adhere to either 2 or 4-electron process over an extended period. The $Fe_2P_2O_7\|Fe_2P_2O_7$ on NF purveyed a low cell potential of just 1.68 V at a current density of 10 mA/cm² (**Figure 3.16a**) comparatively lower cell voltage than already reported work as tabulated in **Table 3.4**, while still creating a huge bubble with a high endurance, as seen by the overlap between the cycle 1 and 1000 of polarization curves as shown in **Figure 3.16a**. Furthermore, long term durability test was performed for 24 hours (**Figure 3.16c**), to elucidate and reassure the stability over perennial period and it was observed that the electrolyzer attained 58.9 mA/cm² of

current density and after 24 hours it goes down to 57.4 mA/cm$^2$, indicating highly stable device material for splitting water into $H_2$ and $O_2$.
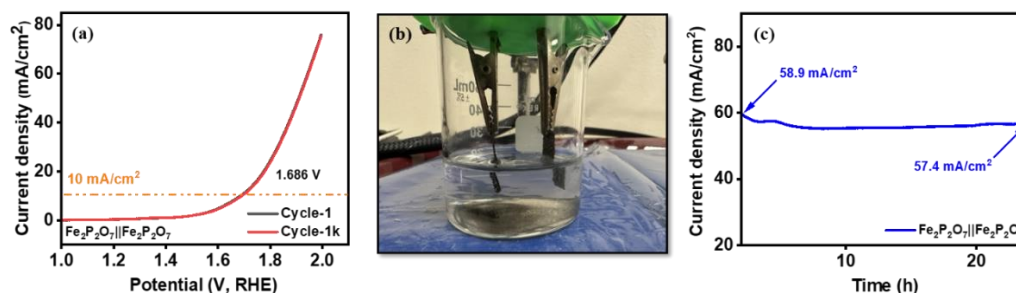


**Figure 3.16:** (a) LSV curve for electrolyzer and polarization stability over 1000 cycles, (b) working of the electrolyzer $Fe_2P_2O_7\|Fe_2P_2O_7$, and (c) chronoamperometry test for electrolyzer over 24 hours.

**Table 3.4:** Comparison of two electrode water splitting cell voltage of $Fe_2P_2O_7\|Fe_2P_2O_7$ electrocatalyst with other bifunctional electrocatalyst.

| Electrocatalyst | Support | Overall cell voltage (V) @ 10 mA/cm$^2$ | Reference |
|---|---|---|---|
| $NiCo_2O_4$ | Ni foam | 1.84 | [120] |
| Co-P | Copper foil | 1.65 | [109] |
| NiFe LDH | Ni foam | 1.70 | [121] |
| $NiCo_2O_4$ | Carbon cloth | 1.98 | [122] |
| **$Fe_2P_2O_7$** | **Ni foam** | **1.68** | **This Work** |

In order to analyze the durability of the $Fe_2P_2O_7$ material electrode towards overall water-splitting process, XRD, SEM and EDX was conducted after overall water-splitting stability testing as illustrated in **Figure 3.17**, portraying no structural changes depicted from XRD, no significant changes in the morphology were observed through SEM, and EDX analysis showed the best configuration of the elemental

distribution. Due to its robust nature, it can be summarized that there is no obvious chemical and physical changes occurred after overall water-splitting and can be the best candidate towards water-splitting fuel cell application.
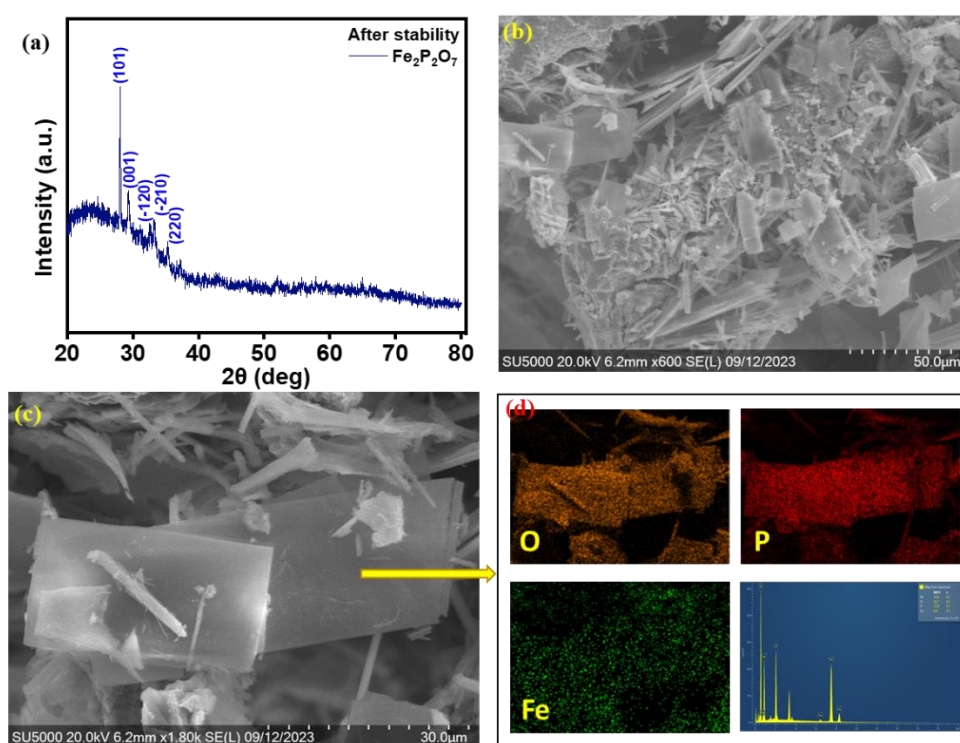


**Figure 3.17:** (a) XRD of $Fe_2P_2O_7$ after overall water-splitting stability test, SEM images of $Fe_2P_2O_7$ electrode after overall water-splitting (b) at magnification of 50 μm, and (c) 30 μm, and (d) elemental mapping (20 kV) of O, P, and Fe, and EDX analysis of Fe, P, and O emission lines for $Fe_2P_2O_7$ at 30 μm of magnification.

### 3.2.4 Electrocatalytic Performance towards Urea Oxidation Reaction

More interestingly, once 0.33 M urea is added into the 1 M KOH electrolyte, its performance towards UOR becomes more impressive, signified by ultralow potential. UOR was highly commendable as it can be used as an energy conversion to produce hydrogen and the treatment of urea-rich ($CO(NH_2)_2$) water contamination. Natural

decomposition of Urea polluted water products such as nitrate and toxic ammonia [10]. However, the products of electrochemical urea oxidation reaction in alkaline medium provides harmless $N_2$ and $CO_2$ that can be captured to form carbonates [123]. Thus, coupling UOR with OER in water electrolysis enriches the $H_2/O_2$ production. Therefore, all as-prepared samples ($Co_2P_2O_7$, $Ni_2P_2O_7$, and $Fe_2P_2O_7$) were investigated towards UOR activity. The onset potential was chosen to report as it initializes commencement of the UOR electrocatalytic activity. **Figure 3.18a** demonstrates the LSV curves of $Co_2P_2O_7$, $Ni_2P_2O_7$, and $Fe_2P_2O_7$ composites, exhibiting $Fe_2P_2O_7$ distinctly ultralow onset potential of 1.317 V than $Ni_2P_2O_7$ (1.319 V) and $Co_2P_2O_7$ (1.321 V) at 10 mA/cm$^2$ of current density. To get a deep understanding of the UOR performance, the onset potential was recorded at low and high current density (**Figure 3.18b**), where at 5 mA/cm$^2$ the potential of $Co_2P_2O_7$, $Ni_2P_2O_7$, and $Fe_2P_2O_7$ is 1.313, 1.309, and 1.307 V, respectively and at 50 mA/cm$^2$ the onset potential of $Ni_2P_2O_7$ with 1.397 V while comparing to $Co_2P_2O_7$ (1.377 V). However, $Fe_2P_2O_7$ still holds the least onset potential (1.375 V). To judge the catalytic performance of the best sample ($Fe_2P_2O_7$), an onset potential more intuitively from LSV curve is presented in **Figure 3.18c**, bare Ni foam, $IrO_2$, and $Fe_2P_2O_7$ displayed potentials of 1.471, 1.454, and 1.317 V, respectively to obtain a current density of 10 mA/cm$^2$. Moreover, $Fe_2P_2O_7$ presented a large current density of 239.5 mA/cm$^2$ which is 1.94 and 8.24 times higher than $IrO_2$ and bare Ni foam. In that prospective, the UOR performance of the synthesized catalysts showed better results as displayed in **Figure 3.18d** which is tabulated in **Table 3.5**, suggesting $Fe_2P_2O_7$ serving promising catalytic activity. Inspired by the improved activity of OER, least onset potential is not the only parameter which can detect the specialty of the material for the electrocatalytic urea oxidation. One of the pivotal parameters which integrates the catalytic activity is kinetics against the sluggish

complicated six-electron transfer process of UOR, using Tafel slope and TOF. The corresponding Taffel slope (**Figure 3.18e**) of the as-obtained samples $Co_2P_2O_7$, $Ni_2P_2O_7$, and $Fe_2P_2O_7$ is 144, 114, and 96.6 mV/dec, respectively, pointing that $Fe_2P_2O_7$ could effectively speed up the dynamic process of UOR. In addition, to examine the pseudo first order reaction kinetics, known as rate determining step reaction and intrinsic property of $Co_2P_2O_7$, $Ni_2P_2O_7$, and $Fe_2P_2O_7$ was calculated by accounting TOF and summarized in **Figure 3.18f**. The kinetics of reaction mechanism was governed by higher value of TOF. Hence, $Fe_2P_2O_7$ exhibit TOF of 0.919 $s^{-1}$ more than the other two samples, indicating faster charge transfer and kinetics.
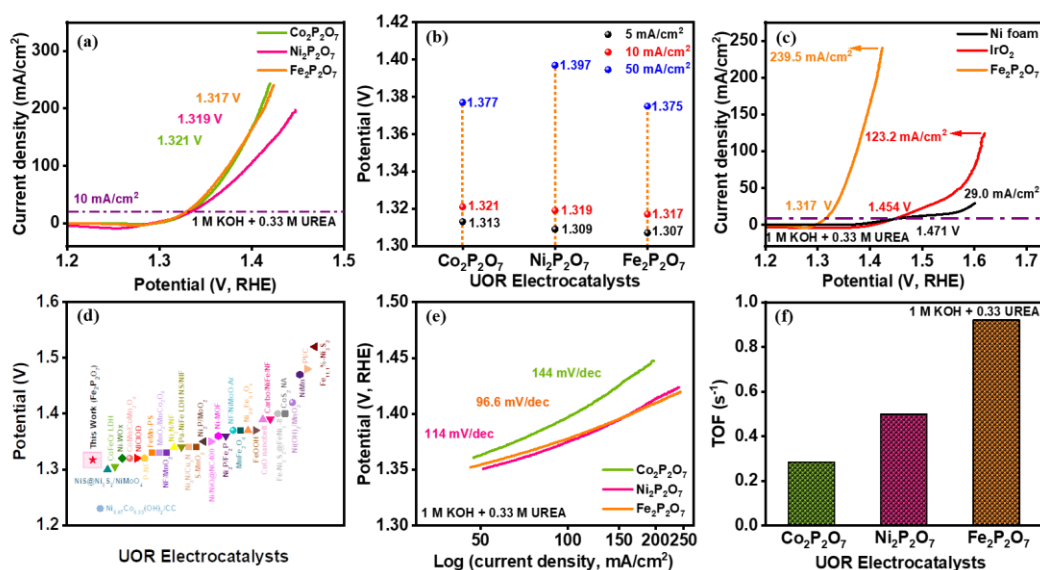


**Figure 3.18:** Electrocatalytic performance for UOR: (a) LSV curves of $Co_2P_2O_7$, $Ni_2P_2O_7$, and $Fe_2P_2O_7$ catalysts applied for electrochemical UOR (0.33 M Urea in 1 M KOH) were recorded at scan rate of 2 mV/s, (b) comparison of onset potentials at different current density for as-prepared catalysts, (c) comparison of onset potential of $Fe_2P_2O_7$ required at 10 mA/cm$^2$ with Ni foam and benchmarking $IrO_2$, (d) comparison of potential required at 10 mA/cm$^2$ with other UOR electrocatalysts, (e) Tafel slopes

of the samples, and (f) Turnover frequency at 1.58 V (v/s RHE) of $Co_2P_2O_7$,

$Ni_2P_2O_7$, and $Fe_2P_2O_7$ catalysts for UOR (0.33 M Urea in 1 M KOH).

On comparing activity of OER and UOR, polarization curves were plotted together for samples to obtain a transparent image of performance as delineated in **Figure 3.19(a-c)** for $Co_2P_2O_7$, $Ni_2P_2O_7$, and $Fe_2P_2O_7$, respectively, manifesting, addition of urea into the electrolyte enhances the current density significantly towards UOR than OER. Least overpotential, high current density, low Tafel slope, and improved TOF collectively implies that the sluggish OER can be replaced by UOR reaction to generate hydrogen at a lower cell voltage. Based on onset potential for both the UOR (1.317 V vs. RHE) and OER (1.482 V vs. RHE) processes, inferring that the $Fe_2P_2O_7$ anode was noticeably active for both processes, may be due to high anodic current density at lower potentials to produce hydrogen at high rate at cathode. The synergistic effect between Fe and P facilitates favorable conductivity and faster charge transfer.
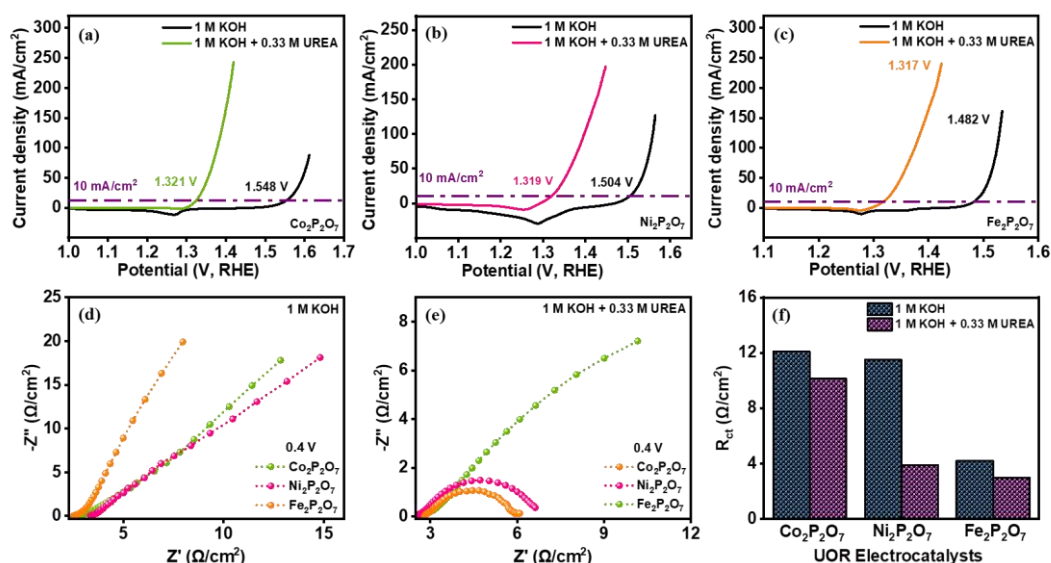
**Figure 3.19:** (a-c) Comparison of onset Potential of the OER and UOR at 10 mA/cm$^2$ for $Co_2P_2O_7$, $Ni_2P_2O_7$, and $Fe_2P_2O_7$ catalysts, (d) EIS of $Ni_2P_2O_7$, $Co_2P_2O_7$, and $Fe_2P_2O_7$ catalysts at 0.4 V (v/s RHE) in 1 M KOH (e) EIS of $Ni_2P_2O_7$, $Co_2P_2O_7$, and $Fe_2P_2O_7$ catalysts at 0.4 V (v/s RHE) in 1 M KOH + 0.33 M Urea, and (f) comparison of charge transfer resistance of OER and UOR.

Therefore, to examine conductive nature of the as-synthesized materials, electrochemical impedance spectroscopy (EIS) was carried out for OER and UOR processes and corresponding results were plotted in form of Nyquist plot at 0.4 V in **Figure 3.19d** and **Figure 3.19e**, respectively. The $R_{ct}$ values obtained in 1 M KOH and 0.33 M urea in 1 M KOH electrolytes were recorded and shown in **Figure 3.19f**. The $R_{ct}$ values obtained during the OER process for $Co_2P_2O_7$, $Ni_2P_2O_7$, and $Fe_2P_2O_7$ catalysts are 12.1, 11.5, and 4.2 $\Omega/cm^2$, whereas during the UOR process the $R_{ct}$ values for $Co_2P_2O_7$, $Ni_2P_2O_7$, and $Fe_2P_2O_7$ are 10.1, 3.9, and 2.9 $\Omega/cm^2$. The $R_{ct}$ obtained for UOR shows lower value than $R_{ct}$ obtained during OER. Thus, confirming the improved kinetics and conductivity of the iron-based pyrophosphate towards UOR. Further, to understand the comprehensive mechanism underlying the versatile nature of the as-

46

synthesized materials towards UOR, sequential analysis was performed. Since SEM images are not well finite to distinguish the morphology of the prepared materials because of similar microstructures. Therefore, high catalytic activity of $Fe_2P_2O_7$ electrode material can be attributed to the rough surface which allows the exposure of numerous active sites. Hence, electrochemical active surface area (ECSA) testing was involved to perceive the involvement of morphology during electrochemical investigations [89]. ECSA is considered as an indicator of the surface roughness and high catalytic performance of electrode material. Herein, A cyclic voltammetry (CV) for $Co_2P_2O_7$, $Ni_2P_2O_7$, and $Fe_2P_2O_7$ were obtained (**Figure 3.20(a-c)**) at a non-faradic potential window at different scan rates ranging from 2 mV/s to 100 mV/s for the estimation of charging current. The $C_{dl}$ (**Figure 3.20d**) values of the $Co_2P_2O_7$, $Ni_2P_2O_7$, and $Fe_2P_2O_7$ are 3, 32, and 85 mF. It has been noticed that the $Fe_2P_2O_7$ offers impressive double layer capacitance over the surface. In that sense, $Fe_2P_2O_7$ leads to expose more active sites, affirms the highest ECSA value of 2125 $cm^2$ than $Ni_2P_2O_7$ (800 $cm^2$) and $Co_2P_2O_7$ (75 $cm^2$) as illustrated in **Figure 3.20e**. The exposure of more active sites consecutively generates high amount of gas bubbles as a greater number of charged species interact with material surface. To investigate the gas bubble dissipation efficiency of the materials, the roughness factor (RF) of the electrode was estimated as shown in **Figure 3.20f** and observed that the RF value for $Co_2P_2O_7$, $Ni_2P_2O_7$, and $Fe_2P_2O_7$ are 117.2, 1960.7, and 4325.3, respectively. The highest RF value of $Fe_2P_2O_7$ enumerates the excellent potential of exaggerating dissipation of gases in surplus amount. Therefore, morphology of $Fe_2P_2O_7$ facilitates accelerated diffusion of electrolyte ions inwards and the diffusion of gas outwards.
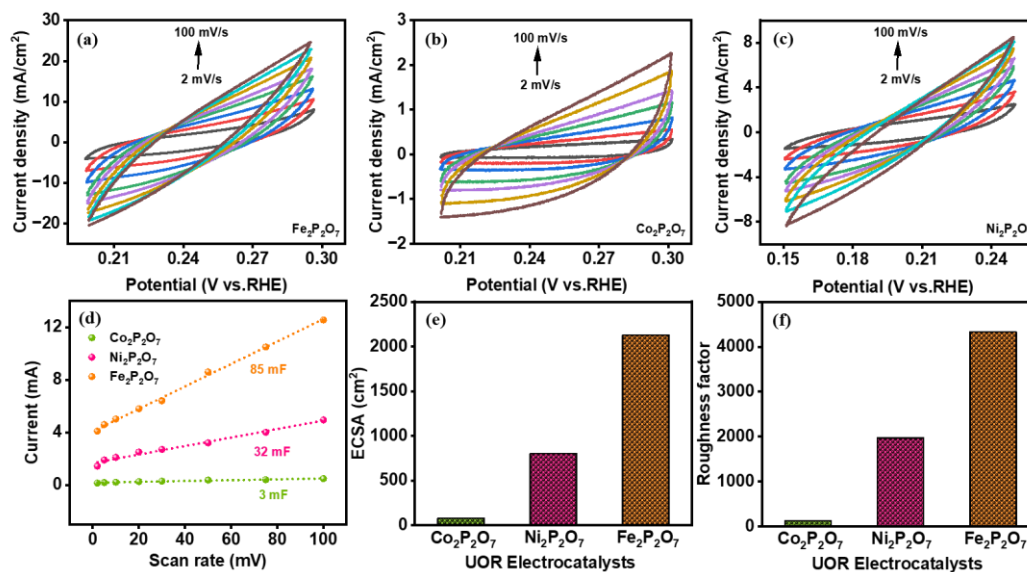
**Figure 3.20:** (a-c) CV of $Co_2P_2O_7$, $Ni_2P_2O_7$, and $Fe_2P_2O_7$ in the non-faradic region, respectively, (d) Double layer capacitance, (e) Electrochemical surface area for $Co_2P_2O_7$, $Ni_2P_2O_7$, and $Fe_2P_2O_7$, and (f) Roughness factor of all the as-synthesized samples.

The stability of UOR for all as-prepared samples were examined and confirmed by steady polarization curves as illustrated in **Figure 3.21(a-c)** where a minute deviation from cycle 1 polarization curve to the cycle 10,000 polarization curve. Further, longevity was tested by long-term chronoamperometry test, where it displays the stable relationship between current density over time. Therefore, the CA was recorded as shown in **Figure 3.21(d-f)**, representing stability of all the as-synthesized samples at 0.65 V potential. The $Co_2P_2O_7$, $Ni_2P_2O_7$, and $Fe_2P_2O_7$ electrode's current density somewhat from 43.1, 46.8, and 116.2 to 36.6, 40.6, and 110.6 mA/cm$^2$, respectively. As per the observation, the $Fe_2P_2O_7$ possess eminent durability for UOR application. It is particularly more impressive that the as-prepared catalyst shows lover $R_{ct}$, and higher ECSA which contributes to a good agreement for a best candidate towards wastewater-splitting (UOR) catalytic performance.

48
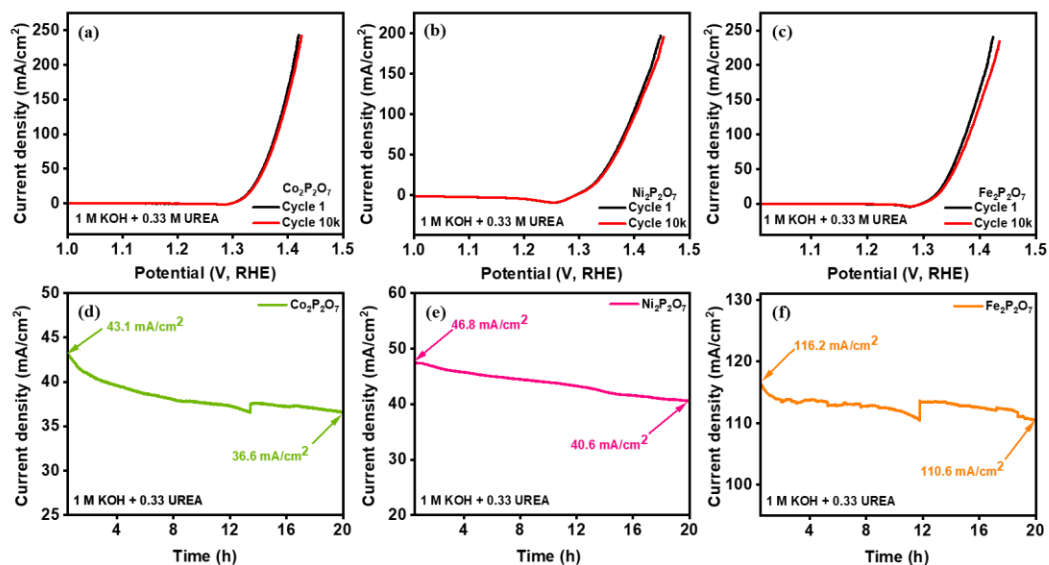
**Figure 3.21:** (a-c) Polarization curve stability over 10,000 cycles of all as-prepared samples, (d-f) Chronoamperometry test of $Co_2P_2O_7$, $Ni_2P_2O_7$, and $Fe_2P_2O_7$ catalysts towards UOR.

**Table 3.5:** Comparison of the previously reported electrocatalysts for UOR.

| Electrocatalyst | Electrolyte | Potential (V) @ 10 mA/cm² | References |
|---|---|---|---|
| $Ni_{0.67}Co_{0.33}(OH)_2$/CC | 1M KOH + 0.5M Urea | 1.23 | [10] |
| $NiS@Ni_3S_2$/NiMoO$_4$ | 1M KOH + 0.33M Urea | 1.30 | [124] |
| CoFeCr LDH | 1M KOH + 0.33M Urea | 1.305 | [125] |
| Ni-WOx | 1M KOH + 0.33M Urea | 1.32 | [126] |
| $CoMn/CoMn_2O_4$ | 1M KOH + 0.33M Urea | 1.32 | [127] |
| NICIOD | 1M KOH + 0.33M Urea | 1.32 | [128] |
| P-NF | 1M KOH + 0.33M Urea | 1.32 | [129] |
| FeMn-PS | 1M KOH + 0.33M Urea | 1.33 | [130] |
| $MnO_2/MnCo_2O_4$ | 1M KOH + 0.5M Urea | 1.33 | [131] |
| $NF/MnO_2$ | 1M KOH + 0.5M Urea | 1.33 | [132] |

| | | | |
|---|---|---|---|
| $Ni_3N/NF$ | 1M KOH + 0.33M Urea | 1.34 | [133] |
| Pa-NiFe LDH NS/NIF | 1M KOH + 0.33M Urea | 1.34 | [134] |
| $Ni_4N/Cu_3N$ | 1M KOH + 0.5M Urea | 1.34 | [135] |
| $S-MnO_2$ | 1M KOH + 0.33M Urea | 1.34 | [132] |
| $Ni_2P/MoO_2$ | 1M KOH + 0.5M Urea | 1.35 | [136] |
| $Ni/NiO@NC_{400}$ | 1M KOH + 0.33M Urea | 1.35 | [137] |
| Ni-MOF | 1M KOH + 0.33M Urea | 1.36 | [138] |
| $Ni_2P/Fe_2P$ | 1M KOH + 0.33M Urea | 1.36 | [139] |
| NF/NiMoO-Ar | 1M KOH + 0.33M Urea | 1.37 | [140] |
| N, S-doped carbon-$MnFe_2O_4$ | 1M KOH + 0.33M Urea | 1.37 | [130] |
| $Ni_{0.9}Fe_{0.1}O_x$ | 1M KOH + 0.33M Urea | 1.37 | [141] |
| FeOOH | 1M KOH + 0.33M Urea | 1.37 | [142] |
| CuO nanobelt | 1M KOH + 0.5M Urea | 1.39 | [143] |
| Carbon/NiFe/NF | 1M KOH + 0.33M Urea | 1.39 | [144] |
| $Fe-Ni_3S_2@FeNi_3-8$ | 1M KOH + 0.33M Urea | 1.40 | [145] |
| $CoS_2$ NA | 1M KOH + 0.33M Urea | 1.40 | [146] |
| $Ni(OH)_2/MnO_2$ | 1M KOH + 0.5M Urea | 1.42 | [147] |
| NiMn-decorated activated carbon | 1M KOH + 0.33M Urea | 1.47 | [148] |
| Pt/C | 1M KOH + 0.5M Urea | 1.48 | [132] |
| $Fe_{11.1\%}-Ni_3S_2$ | 1M KOH + 0.33M Urea | 1.52 | [149] |
| **$Co_2P_2O_7$** | **1M KOH + 0.33M Urea** | **1.321** | **This Work** |
| **$Ni_2P_2O_7$** | **1M KOH + 0.33M Urea** | **1.319** | **This Work** |
| **$Fe_2P_2O_7$** | **1M KOH + 0.33M Urea** | **1.317** | **This Work** |

### 3.2.5 Computational study of electrocatalysts towards sluggish kinetics of OER and UOR

To perform the theoretical calculations, the primitive unit cell with lattice parameters of a=10.14 Å and b=12.22 Å, having 20 Å vacuum space, was constructed for each catalytic material. The Quantum Espresso calculation software was used to do theoretical computations on the constructed models by employing the generalized-gradient approximation (GGA) theory in association with the Perdew-Burke-Ernzerhof (PBE) functional and the double numerical (+) polarisation functional basis set. To calculate the density of states (DOS) for the constructed models, the convergence limits for force (0.05 eV) and energy (250 eV) were set under the plane-wave expansion of the electronic wave function ($10^{-5}$ eV). After thoroughly optimizing the constructed models, the adsorption energies for OER and HER adducts were calculated using the following equation (3.10).

$$\Delta E_{ads.} = E_{(catalyst)} + E_{(reactant)} - E_{(catalyst\text{-}reactant)} \tag{3.10}$$

Where, $E_{(catalyst\text{-}reactant)}$, $E_{(catalyst)}$, and $E_{(reactant)}$ are the energies of catalyst-reactant adduct, catalyst, and reactant, respectively.

To gain a more comprehensive understanding of the OER and UOR mechanism on $Fe_2P_2O_7$, $Co_2P_2O_7$, and $Ni_2P_2O_7$ catalysts, the optimized structural model of $Fe_2P_2O_7$, $Co_2P_2O_7$, and $Ni_2P_2O_7$ catalysts is depicted in **Figure 3.22 (a-c)**, illustrating both their side and top-view perspectives.
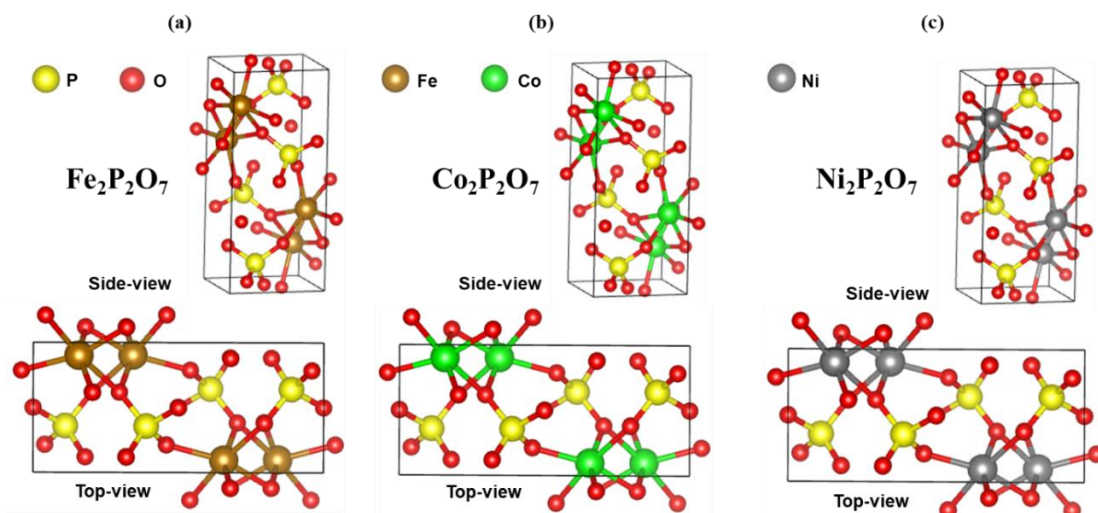
**Figure 3.22:** Side and Top views of optimized crystal lattice (a) $Fe_2P_2O_7$, (b) $Co_2P_2O_7$, and (c) $Ni_2P_2O_7$.

In addition, an investigation was conducted to examine the structural electronic modifications in $Fe_2P_2O_7$, $Co_2P_2O_7$, and $Ni_2P_2O_7$ catalysts. This investigation involved the calculation of the density of states (DOS) (**Figure 3.23 (a-c)**) and the projected density of states (PDOS) (**Figure 3.23 (d-f)**). The findings of the computed DOS and PDOS clearly indicated a significant distribution of improved density of states over the Fermi level for $Fe_2P_2O_7$ catalyst, as compared to $Ni_2P_2O_7$ and $Co_2P_2O_7$ catalysts, improving the electronic conductivity and electron migration efficiency of $Fe_2P_2O_7$ further facilitate to electron transfer in the catalytic process [150]. Hence, aggrandizing catalytic kinetics towards OER and UOR processes.
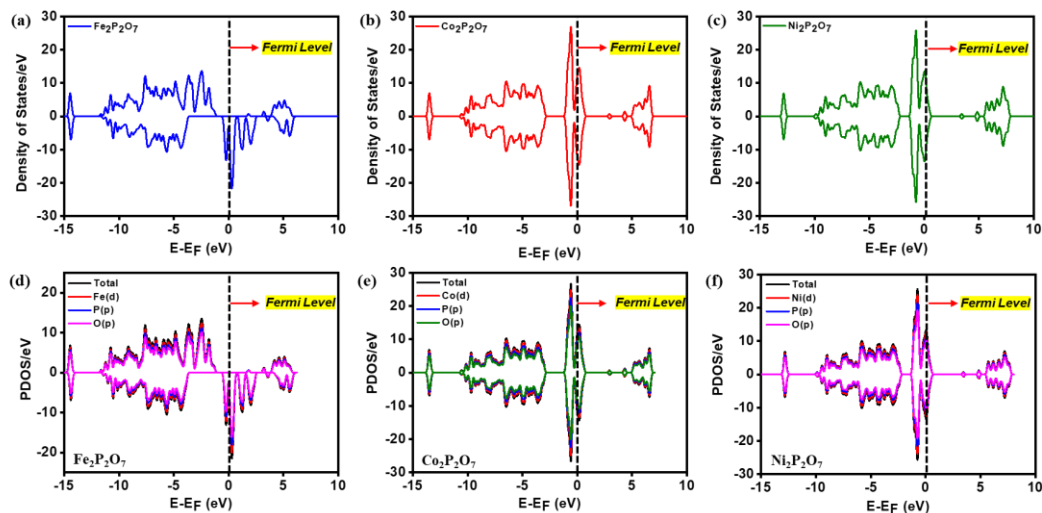
**Figure 3.23:** Density of States of (a) $Fe_2P_2O_7$, (b) $Co_2P_2O_7$, (c) $Ni_2P_2O_7$, and Projected Density of States and (d) $Fe_2P_2O_7$, (e) $Co_2P_2O_7$, and (f) $Ni_2P_2O_7$.

To investigate the electrocatalytic process on $Fe_2P_2O_7$, $Co_2P_2O_7$, and $Ni_2P_2O_7$ catalysts, further evidence was collected by employing band structure study as shown in **Figure 3.24(a-c)**, where we found a marked increase in band population in the conduction band with a low band gap value of 2.34 eV for $Fe_2P_2O_7$ catalyst as compared to $Ni_2P_2O_7$ (2.41 eV) and $Co_2P_2O_7$ (2.46 eV) catalysts, corroborated by DOS study, suggesting significant increase in the conductivity of $Fe_2P_2O_7$ as compared to other samples. These results suggested a synergistic effect between Fe and P to facilitate favourable conductivity and faster charge transfer for the $Fe_2P_2O_7$ catalyst, enhancing its activity. Further, to investigate the OER mechanism in the proposed structural models of $Fe_2P_2O_7$, $Co_2P_2O_7$, and $Ni_2P_2O_7$ catalysts, the OER reaction intermediates were systematically absorbed on their catalytic active sites (*), Fe, Co, and Ni, respectively, and optimized. The results indicated that the conversion of *O into *OOH, being a rate-determining step, controlled the overall OER reaction, requiring remarkable energy for all constructed catalysts' models. Furthermore, the observed

disparity in charge density suggests higher transfer of electron density between *OOH and Fe, in contrast to other active sites such as Ni and Co. this finding provides evidence for the efficient electronic communication between *OOH and Fe, which plays crucial role in regulating the detachment of *OOH from the Fe site (**Figure 3.24d**). Among the prepared catalysts, $Fe_2P_2O_7$ indicated a requirement of less Gibbs free energy for OH-adsorption on the active site and $O_2$ detachment from the active site, validating its high catalytic activity as compared to other catalysts (**Figure 3.24e**) [151,152].
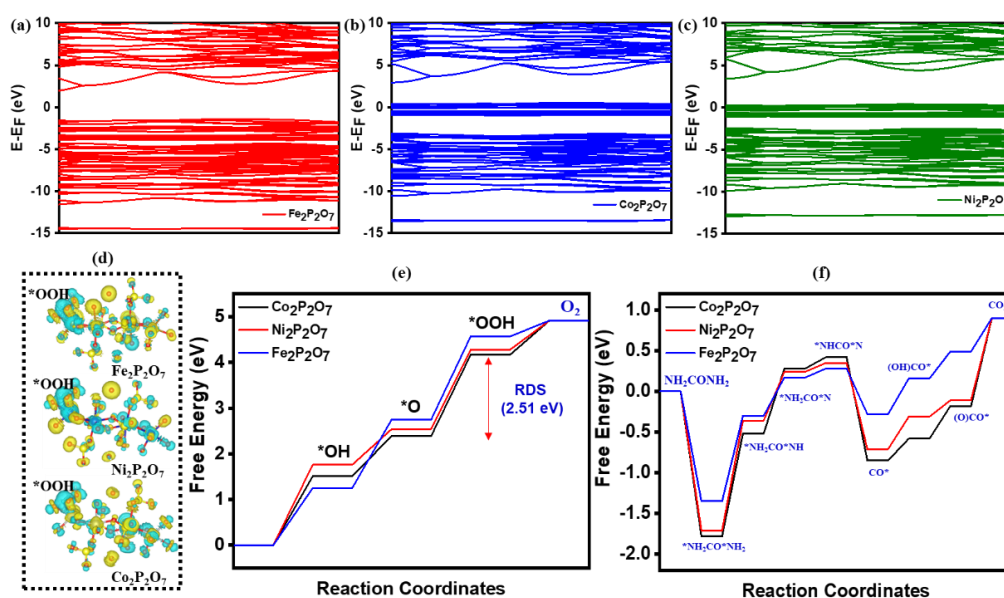


**Figure 3.24:** Band structure of (a) $Fe_2P_2O_7$, (b) $Co_2P_2O_7$, (c) $Ni_2P_2O_7$, (d) Charge density of *OOH-adduct of $Fe_2P_2O_7$, $Ni_2P_2O_7$, and $Co_2P_2O_7$, (e) OER Free Energy Diagram, and (f) UOR Free Energy Diagram.

Furthermore, to propose the UOR mechanism over the generated electrocatalysts, the likely UOR intermediates were absorbed on the active site of all the prepared samples and the computed Gibbs free energy diagram for the UOR process over the constructed catalysts in shown in **Figure 3.24f**, educating that the $Fe_2P_2O_7$

54

catalyst has lower energy barriers for all UOR step, especially acknowledging HER, than the $Co_2P_2O_7$, and $Ni_2P_2O_7$ catalysts [128,153]. Additionally, the radar plot in **Figure 3.25** illustrated the salient feature of as-prepared electrocatalysts towards HER, OER, and UOR. The computational study best matches with the electrochemical catalytic activity. Hence, $Fe_2P_2O_7$ presented high conductivity and active electrons and high adsorption of $OH^-$, leading to the facilitation of electrocatalytic activity.
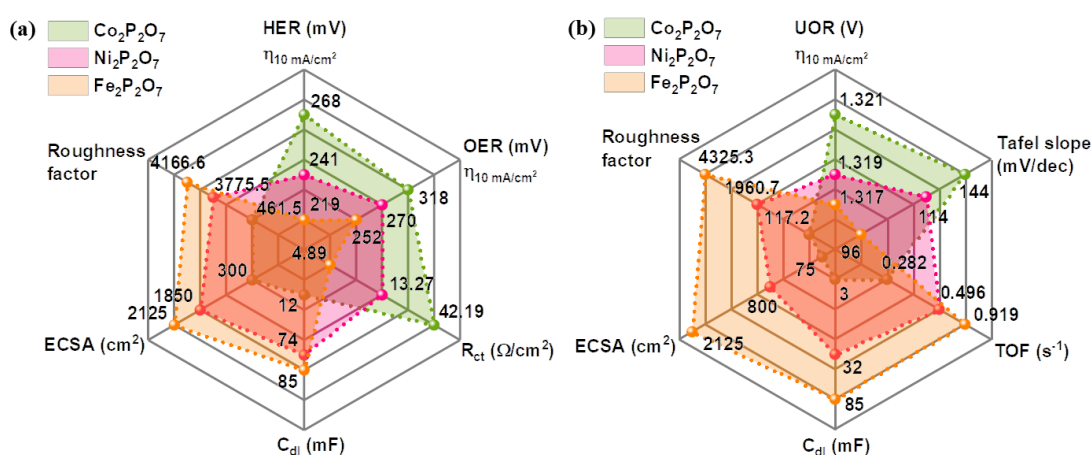


**Figure 3.25:** (a-b) Radar plot comparing six figures of merits of as-synthesized materials towards HER, OER and UOR process.

### 3.2.6 Electrochemical Supercapacitor performance

After microscopic, phase, and electrocatalyst investigation of the materials, the detailed performance of the as-synthesized metal pyrophosphate electrodes toward the electrochemical supercapacitor using cyclic voltammograms, galvanostatic charge-discharge, electrochemical impedance spectroscopy, and stability. Pyrophosphates possess excellent chemical stability, indicating better for the long-life challenge of cycling ability. On the other hand, the electrical harvesting, kinetics of charges, and holding capacity over a long time have been challenging problems for pyrophosphate

materials. Herein, we have developed the $Ni_2P_2O_7$, $Co_2P_2O_7$, and $Fe_2P_2O_7$ grown on Ni-foam to increase the overall conductivity of the electrode. Moreover, the synthesized sample was treated at an optimum temperature during hydrothermal which helped to grow metal-pyrophosphate without shrinking of material and indicated a strong bond between the material and the substrates, leading to highly enhanced stability in electrochemical reactions. For instance, Wang et al. [154] designed marigold flower-like $Mn_2P_2O_7$ material and further applied it to a Li-ion battery. However, the obtained material was irreversible at first due to charges consumed to reduce $Mn^{2+}$ ions to the metallic state and owing to the formation of electrolyte interphase. Later on, Senthilkumar *et al.* [61] fabricated a highly porous carbon-based $Ni_2P_2O_7$ electrode for supercapacitor application. To promote high conductivity and stability, electrode material possesses a high-purity phase, morphology, sufficient working potential, and reversibility. In those terms, they successfully acquired grain-like nanoparticles which resembled the monoclinic phase of $Ni_2P_2O_7$ which further enhanced the electrochemical process. Following to that, Hou *et al.* [155] designed promising 1D $Co_2P_2O_7$ nanorods without any templates and high-temperature calcination as a pseudocapacitive material for energy storage. The obtained material contains $CoO_6$ coordination octahedron phase with $P_2O_7$ groups as an electroactive component for electrochemical activity. In addition, its magnetic and microwave absorption properties also fascinated that material for highly stable and reversible supercapacitor devices. Considering all those parameters, the developed $Ni_2P_2O_7$, $Co_2P_2O_7$, and $Fe_2P_2O_7$ was projected towards preliminary CV testing in 3 M KOH electrolyte at various scan rate from 2 to 300 mV/s in a potential window of 0 to 0.6 V and the outcomes are illustrated in **Figure 3.26(a-c)**. CV plot demonstrated pseudocapacitive behaviour of the materials and one oxidation and reduction peak appeared in $Ni_2P_2O_7$ and $Fe_2P_2O_7$ at lower scan rate unless

$Co_2P_2O_7$, having two pair of redox peaks due to two step reversible redox reaction of $Co(II) \leftrightarrow Co(III)$ and $Co(III) \leftrightarrow Co(IV)$ reactions, respectively. Oxidation peaks where first peak around 0.3-0.4 V can be ascribed to the oxidation of $Co^{2+}$ to $Co^{3+}$ and peak about 0.45 to 0.55 occurred due to the $Co^{3+}$ to $Co^{4+}$; all the samples showed stable redox profile the profound reversibility due to symmetric nature of faradic reaction. Therefore, the proposed redox mechanism for $Ni_2P_2O_7$, $Co_2P_2O_7$, and $Fe_2P_2O_7$ with basic electrolyte is described in the equation (3.11-3.14), respectively [47,156–158].

$$Ni_2P_2O_7 + 2OH^- \leftrightarrow Ni_2P_2O_7(OH^-)_2 + 2e^- \tag{3.11}$$

$$Co_2P_2O_7 + 2OH^- \leftrightarrow Co_2(OH)_2P_2O_7 + 2e^- \tag{3.12}$$

$$Co_2(OH)_2P_2O_7 + 2OH^- \leftrightarrow Co_2O_2P_2O_7 + 2\,H_2O + 2e^- \tag{3.13}$$

$$Fe_2P_2O_7 + 2OH^- \leftrightarrow Fe_2P_2O_7(OH^-)_2 + 2e^- \tag{3.14}$$
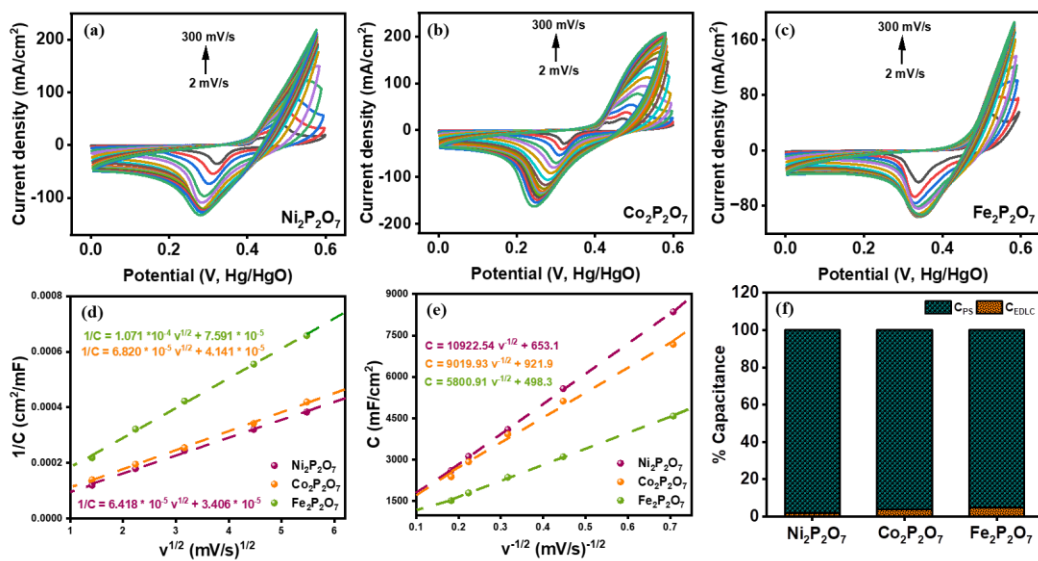


**Figure 3.26:** (a-c) CV voltammogram for the $Ni_2P_2O_7$, $Co_2P_2O_7$, and $Fe_2P_2O_7$, at different scan rates ranging from 2-300 mV/s, respectively, Trasatti plot of (d) 1/C vs $V^{1/2}$ of the $Ni_2P_2O_7$, $Co_2P_2O_7$, and $Fe_2P_2O_7$, and (e) C vs $v^{-1/2}$ of $Ni_2P_2O_7$, $Co_2P_2O_7$, and $Fe_2P_2O_7$, and (e) percentage of capacitance contribution evaluated for the electrodes based on trasatti analysis.

The electrode material delineated quasi-reversible reaction which is because of multiple oxidation states of the Ni, Co, and Fe, here $Ni^{2+}/Co^{2+}/Fe^{2+}$ transformed to the $Ni^{3+}/Co^{3+}/Fe^{3+}$ during redox process. From the reaction equation (3.11-3.14), inferred that the pair of redox reaction can be observed at a specified potential range, indicating reversible reaction. Analogous to the work done by Wang et al. and group, where they acknowledged that due to lower Pauling electronegativity of P (2.19) enables much higher conductivity. Therefore, the electronegativity difference of $P_2O_7$ anion facilitates Ni, Co, and Fe and without any further distortion of the CV plots, resembling best reversibility, enhanced mass transportation, capacitive property, and rate of charge transfer. Furthermore, the observed distinctive peak at lower rate corresponds to the pseudocapacitive performance. However, while increasing the scan rate the anodic peak shifted towards right and cathodic peak to the lower potential due to limited interaction of $OH^-$ ions. Thereby, we employed a Trasatti method to identify the charge stored by the material of the electrodes, either a pseudocapacitive which refers to reversible redox phenomenon, showing the intercalation or electro absorption of the ions or electrochemical double layer capacitance (EDLC) formed at the electrode/electrolyte interface. The equation (3.15-3.17) is involved to study the mechanism behind the CV curves [159].

$$1/C = k_1 v^{1/2} + 1/C_T \tag{3.15}$$

$$C = k_2 v^{-1/2} + C_{EDLC} \tag{3.16}$$

$$C_{PS} = C_T - C_{EDLC} \tag{3.17}$$

where, C signifies areal capacitance, $C_T$ is total capacitance, $C_{EDLC}$ symbolizes electrical double layer capacitance, and $C_{PS}$ infers pseudo capacitance contribution. A plot of $1/C$ in function to $v^{1/2}$ as illustrated in **Figure 3.26d** and a plot of C in function to $v^{-1/2}$ as

shown in **Figure 3.26e** has been analyzed to deduce the EDLC and pseudocapacitance contribution of the $Ni_2P_2O_7$, $Co_2P_2O_7$, and $Fe_2P_2O_7$ electrodes. The overall $C_{EDLC}$ and $C_{PS}$ contribution was illustrated in **Figure 3.26f** based on Trasatti method, indicating $Ni_2P_2O_7$ offered high pseudocapacitive behavior of 98% with a least EDLC influence of 2%. However, $Co_2P_2O_7$, and $Fe_2P_2O_7$ showed pseudo mechanism by 96% and 95% and EDLC of 4% and 5%, respectively.
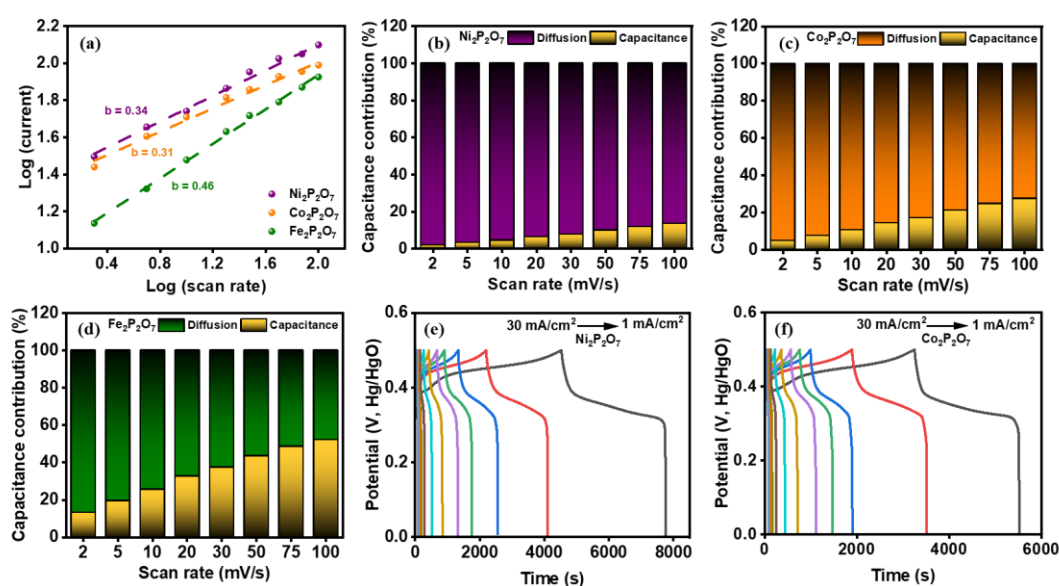


**Figure 3.27:** (a) Power-law dependence of anodic currents at various scan rates, (b-d) Diffusion and Capacitive controlled contribution at various scan rates ranging from 2-100 mV/s for $Ni_2P_2O_7$, $Co_2P_2O_7$, and $Fe_2P_2O_7$, (e) Galvanostatic charging-discharging of the $Ni_2P_2O_7$, and (f) Galvanostatic charging-discharging of the $Co_2P_2O_7$.

Overall, the $Ni_2P_2O_7$ represented pseudocapacitive dominated material. Furthermore, to corroborate the kinetic mechanism of the as synthesized materials in terms of diffusion and capacitive nature by in-depth observation of CV curves at different scan rates from 2 mV/s to 100 mV/s was taken into consideration. Hence,

Power law was adopted for further calculations which is described in equation (3.18-3.19).

$$i = i_{cap} + i_{diff} = av^b \qquad (3.18)$$

$$logi = loga + blogv \qquad (3.19)$$

where i is the sum of diffusion-controlled process ($i_{diff}$) and surface capacitance-controlled process ($i_{cap}$), v represents scan rate, a and b are adjustable parameters where predominant charge storage mechanism was ascertained using b-values, as shown in **Figure 3.27a** which depicts that all the samples completely reliance on ion diffusion. In order to further investigate the contribution of both the mechanism, the total capacity can be quantitively divided into two parts; $k_1v$ stands for capacitive effect and $k_2v^{1/2}$ for diffusion-controlled effects as according to equation (3.20).

$$i(V) = i_{cap} + i_{diff} = k_1v + k_2v^{1/2} \qquad (3.20)$$

The $k_1v$ and $k_2v^{1/2}$ contributions is illustrated for $Ni_2P_2O_7$, $Co_2P_2O_7$, and $Fe_2P_2O_7$ from 2 to 100 mV/s of scan rate in **Figure 3.27(b-d)**. At low scan rate of 10 mV/s the $k_1v$ and $k_2v^{1/2}$ contributions were 5, 11, and 26% and 95, 89, and 74% for $Ni_2P_2O_7$, $Co_2P_2O_7$, and $Fe_2P_2O_7$, respectively, whereas, at 100 mV/s the contributions tuned to 13, 28, and 52% and 87, 72, and 48% for $Ni_2P_2O_7$, $Co_2P_2O_7$, and $Fe_2P_2O_7$, respectively. On the contrary of both the mechanisms, the diffusion dominated over capacitive nature in $Ni_2P_2O_7$ with least involvement of surface capacitance. Therefore, it reflects that the $Ni_2P_2O_7$ possess high rate of ingression of anions deep inside the nanomaterial than regression of the ions. Thus, it takes a longer time to completely discharge of ions out of the material to the electrolyte. It is clearly visible that the diffusion was responsible to influence the charge barring property of the material.

Furthermore, the charge holding ability of the electrodes were tested under the norms of galvanostatic charge-discharge method and was performed at a different

current density of 1 to 30 mA/cm$^2$ ran at a potential window of 0.0 to 0.5 V in a 3 M KOH. Discharge time is the indispensable parameter for the electrochemical performance for supercapacitor and greater time indicates higher specific capacitance. The specific capacitance (C$_s$) of the electrodes was derived by using the discharge profile of the GCD as shown in **Figure 3.27(e-f)** and **Figure 3.28a**, using equation (3.21) where i is current, Δt is discharge time drew from GCD plots, cm$^2$ is the area of the electrodes, and Δv is the potential window. Herein, the GCD curve is disintegrated into three pillars: fast potential drop, plateau regime and sharp decay. The pioneer decay of potential is due to internal resistance, intermediate regime of GCD dedicated to plateau due to faradic redox reaction where, Ni$_2$P$_2$O$_7$ and Co$_2$P$_2$O$_7$ displayed a plateau region but Fe$_2$P$_2$O$_7$ showed slant nature during discharge, indicating amorphous behaviour of the material (surface capacitance). The GCD plot at higher current densities, such as 15, 20, 25 and 30 mA/cm$^2$ showed a gradual decrease in the discharge time as a consequence of increased voltage drop and insufficient active electrode material took part in redox reactions at higher current densities. The comparative plot of GCD for Ni$_2$P$_2$O$_7$, Co$_2$P$_2$O$_7$, and Fe$_2$P$_2$O$_7$ at a specific current density of 1 mA/cm$^2$ was graphed in **Figure 3.28b** to enumerates the discharge time taken and behaviour of the curve. At last, in the discharge process, the sudden drop of potential was recorded which points the formation of double layer on the surface of the electrode.

$$Specific\ capacitance = I\Delta t/cm^2\Delta v \tag{3.21}$$

The calculated specific capacitance from the discharge curves is shown in **Figure 3.28c** in the function of current densities. It was evident that the Ni$_2$P$_2$O$_7$ outcasted better charge holding property with a maximum specific capacitance than other two samples over different range of current density. In **Figure 3.28d** bar plot shows the comparison of specific capacitance at 1 mA/cm$^2$, where greatest discharge

time corresponds to $Ni_2P_2O_7$ acquired highest specific capacitance of 7986 mF/cm$^2$ (7.986 F/cm$^2$) than the $Co_2P_2O_7$ (7363 mF/cm$^2$) and $Fe_2P_2O_7$ (3745 mF/cm$^2$). **Figure 3.28e** illustrates the GCD of bare Ni foam, acknowledging highly lower discharge time than other as-synthesized composites engineered on Ni foam. Bare Ni foam showed least specific capacitance over different current densities than $Ni_2P_2O_7$, $Co_2P_2O_7$, and $Fe_2P_2O_7$. Very astounding values of $Ni_2P_2O_7$ is because of the agglomerated crystalline structured nanoparticles on the Ni-foam which facilitated more grain boundaries and higher surface area, further improving a more significant number of active sites for $OH^-$ ions. The obtained values for specific capacitance of the three novel electrode materials are better than the already reported work in the past. For instance, nanosheets of $Co_3O_4$/CC (400 mF/cm$^2$ @ 4 mA/cm$^2$) [160], MnO@C composite (720 mF/cm$^2$ @ 4 mA/cm$^2$) [160], nanoneedle arrays of $NiCo_2O_4$ (0.99 F/cm$^2$ @ 5.56 mA/cm$^2$),[161] Na-doped $Ni_2P_2O_7$//AC (22 mF/cm$^2$ at 1 mA/cm$^2$)[161], $Ni_2P_2O_7$/$Co_2P_2O_7$ nanograss array (2074 F/g @ 5 A/g)[162], $Ni_3(PO_4)_2$/RGO/$Co_3(PO_4)_2$ composite (1137.2 F/g at 0.5 A/g)[163], $MnFe_2O_4$/graphene/polyaniline (241 F/g @ 0.5 mA/cm$^2$) [164], $C_3N_4$-1/$Ni_2P_2O_7$ (4.4 F/cm$^2$ @ 1 mA/cm$^2$) [165], $Li_2Co_2(MoO_4)_3$ (1.03 F/cm$^2$ @ 1 mA/cm$^2$) [166], and $Co_{0.5}Ni_{0.5}$DHs/$NiCo_2O_4$/CFP (2.3 F/cm$^2$ @ 2 mA/cm$^2$) [167]. In that sense, the agglomerated micro sheets of the $Ni_2P_2O_7$ as discussed in SEM with high percent of Ni element percentage present in the composite as per EDX investigation provided more Ni for faradic reaction and surface and volume ratio for ease in ions transportation in bulk.
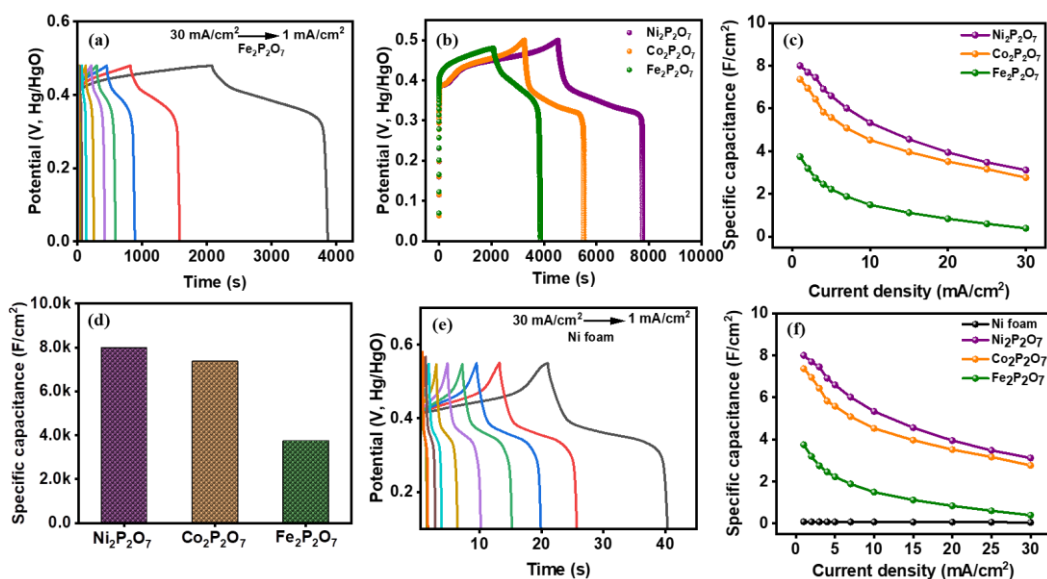
**Figure 3.28:** (a) Galvanostatic charging-discharging of the $Fe_2P_2O_7$, (b) Charge-discharge plot of $Ni_2P_2O_7$, $Co_2P_2O_7$, and $Fe_2P_2O_7$ at 1 mA/cm$^2$, (c) Specific capacitance values at different current densities, (d) Bar plot comparing specific capacitance of $Ni_2P_2O_7$, $Co_2P_2O_7$, and $Fe_2P_2O_7$ at 1 mA/cm$^2$, (e) Galvanostatic charging-discharging of the bare Ni foam at different current densities, and (f) Comparing specific capacitance of $Ni_2P_2O_7$, $Co_2P_2O_7$, and $Fe_2P_2O_7$ to bare Ni foam.

To inculcate the further comprehensive understanding on the charge transfer route and electron transport during the electrochemical process. Therefore, the electrochemical impedance spectrum was measured at room temperature over a frequency range of 0.01Hz to 10k Hz in a 10 mV AC amplitude under open circuit conditions. **Figure 3.29a** shows the Nyquist plot derived from the EIS data, where the arc in the high frequency region reflects the reaction occurring at the electrode surface, corresponding to electron transfer and controls the kinetics of the electrode interface. Hence charge transfer resistance can be calculated by measuring the radii of the arc; directly proportional to each other. The charge transfer resistance of the $Ni_2P_2O_7$, $Co_2P_2O_7$, and $Fe_2P_2O_7$ is 4.05, 5.84, and 20.77 $\Omega$/cm$^2$. The associated Randles circuit

[98] for the Nyquist plot of the as synthesized material was demonstrated in **Figure 3.29b**. Based on EIS observation, the $Ni_2P_2O_7$ is a better electrochemical active material and a defined slope at a lower frequency region also manifest the excellent ingression of ions in the electrode material, proposing more efficient charge transport thus, pointing good capacitive behavior.

Apart from this, the Bode phase angle plot (**Figure 3.29c**) was taken into consideration, which directs the capacitive and inductive nature of the material. If phase angle is closer to -90º, the material obeys capacitive behaviour and behave as an ideal capacitor. The phase angle lesser than -90º at lower frequency represents pseudocapacitive nature[168]. Herein, all the synthesized materials lie between -50º to -60º, confirming their pseudocapacitive trait. Moreover, the charge holding parameter and frequency correspondence to -45º phase angle is defined as figure of merit for supercapacitor materials and response time was calculated and it was found that the $Ni_2P_2O_7$ acquired the least response time of 5.521 s to transfer charges. However, the response time (equation (3.22)) for $Co_2P_2O_7$ and $Fe_2P_2O_7$ are 6.765 s and 8.298 s, respectively. Hence, the less response time and charge transfer resistance of the $Ni_2P_2O_7$ confirmed the improved kinetics.

The frequency dependent capacitance (C) is a addition of real ($C'$) and imaginary capacitance ($C''$) (equation (3.23))[169]. Under that line, the double layer capacitance ($C_{dl}$) was analysed by plotting frequency dependent real capacitance ($C'$) curve as shown in **Figure 3.29d**, measured by using equation (3.24), where, $Z''$ and $|Z|$ signifies the imaginary part (resistance), and modulus of total impedance, respectively and recorded that the capacitance value increases from zero to near saturation[170]. The $C_{dl}$ value for $Ni_2P_2O_7$ (1.75 $F/cm^2$) is higher than $Co_2P_2O_7$, and $Fe_2P_2O_7$, directing highest power density. Moreover, **Figure 3.29e** elucidates imaginary capacitance to

64

frequency (equation (3.25)), where Z′ is the real part (resistance)), which re-assist the response time of $Ni_2P_2O_7$, $Co_2P_2O_7$, and $Fe_2P_2O_7$ is 7.722, 11.312, and 13.227 s and matches the trend of response time calculated by using bode phase angle plot, indicating $Ni_2P_2O_7$ offered better energy density. Additionally, the relationship between power and energy densities were analysed using the Ragone plot in **Figure 3.29f**. With the niches in power density, the energy density depreciates. The maximum power density recorded for $Ni_2P_2O_7$, $Co_2P_2O_7$, and $Fe_2P_2O_7$ is 6.897, 6.870, and 5.965 mW/cm$^2$ and energy density for the three materials are 0.263, 0.251, and 0.118 mWh/cm$^2$, respectively. Thus $Ni_2P_2O_7$ electrode commanding on power and energy density over other electrodes can be used for battery-supercapacitor hybrid device [171].

$$Response\ time = \ 1/2\pi f \tag{3.22}$$

$$(f) = C'(f) + iC''(f),\ \text{where } i = \ \sqrt{-1} \tag{3.23}$$

$$C'(f) = \frac{-Z''(f)}{2\pi f |Z(f)|^2} \tag{3.24}$$

$$C''(f) = \frac{-Z'(f)}{2\pi f |Z(f)|^2} \tag{3.25}$$
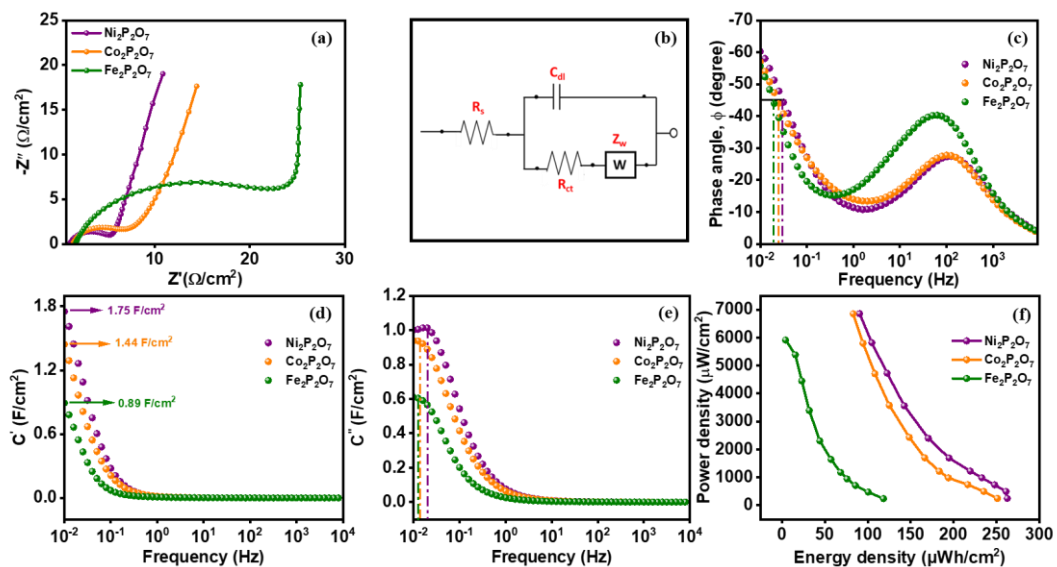
**Figure 3.29:** (a) EIS plot of $Ni_2P_2O_7$, $Co_2P_2O_7$, and $Fe_2P_2O_7$, (b) Randle circuit according to Nyquist plot obtained for $Ni_2P_2O_7$, $Co_2P_2O_7$, and $Fe_2P_2O_7$, (c) Bode phase angle for $Ni_2P_2O_7$, $Co_2P_2O_7$, and $Fe_2P_2O_7$ at 45°, (d) Real capacitance in function to frequency, (e) Imaginary capacitance in function to frequency, and (f) Power density vs energy density of $Ni_2P_2O_7$, $Co_2P_2O_7$, and $Fe_2P_2O_7$.

Stability is considered as a crucial parameter for real life application. Thereby, the cycling stability was carried out for 5000 charge-discharge cycles, **Figure 3.30(a-c)** shows the multiple charge-discharge cycles, capacitance retention and coulombic efficiency of the $Ni_2P_2O_7$, $Co_2P_2O_7$, and $Fe_2P_2O_7$, respectively, where $Ni_2P_2O_7$ holds 97% of capacitance retention and 100% coulombic efficiency. However, $Co_2P_2O_7$ and $Fe_2P_2O_7$ illustrated 81% and 76% of capacitance retention with 100% coulombic efficiency.
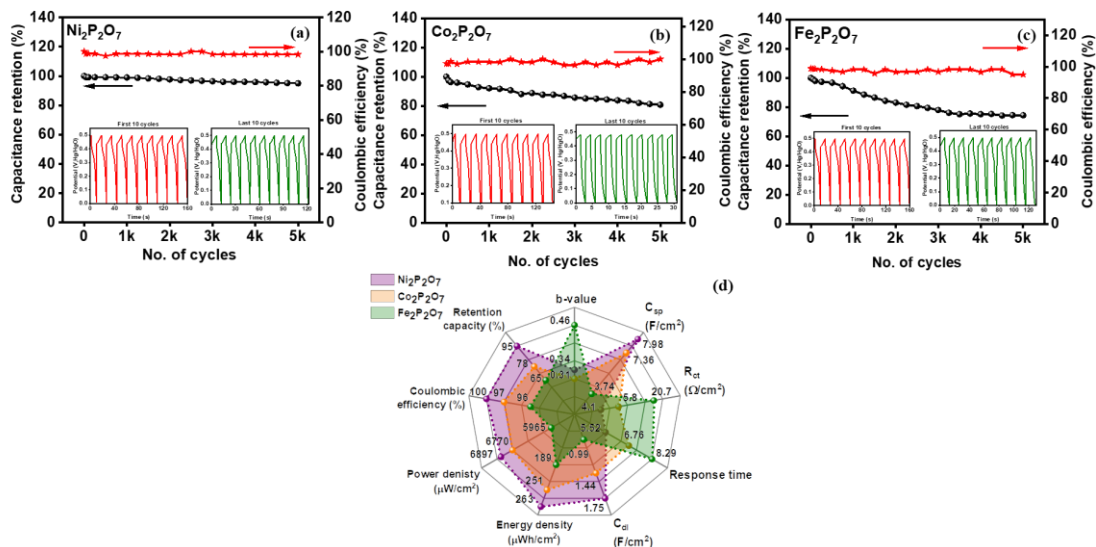
**Figure 3.30:** (a-c) Stability plot of capacitance retention and coulombic efficiency for Ni₂P₂O₇, Co₂P₂O₇, and Fe₂P₂O₇, respectively, and (d) Radar plot comparing nine figures of merit: b-value, specific capacitance ($C_{sp}$), charge transfer resistance ($R_{ct}$), response time, double layer capacitance ($C_{dl}$), energy density, power density, coulombic efficiency, and retention capacity.

The salient features depicted from the Radar plot as displays in **Figure 3.30d** and electrochemical observations as follows; (1)  The XRD reveals the high crystallinity of Ni₂P₂O₇ than other samples, (2) EDX showed more percentage composition of Ni in Ni₂P₂O₇ than other transition metals in Co₂P₂O₇ and Fe₂P₂O₇, exhibiting more conversion of oxidation states of Ni in Ni₂P₂O₇, assisting passivity to the ions feassibly, (3) thus numerous active sites are provided by Ni₂P₂O₇ and better diffuison of ions as an effect of less $R_{ct}$ and response time during electrochemical reaction, (4) highest value of $C_{dl}$, $C_{sp}$, power desnsity, energy density and stability cordially contributing to reason that Ni₂P₂O₇ showed improved and best candidate for supercapacitor application among other pyrophosphates.

**CHAPTER IV**

**CONCLUSION**

To recapitulate, we have demonstrated the fabrication of novel transition metal (Ni, Co, and Fe) based pyrophosphate in-situ engineered on Ni-foam via hydrothermal designated strategy. These materials possess micro-structures of agglomerated micro-particles/plates or flaky morphological architecture. The XRD, XPS, and FT-IR further confirmed the presence of Ni, Co, Fe, P, and O in the chemical structure of $Ni_2P_2O_7$, $Co_2P_2O_7$, and $Fe_2P_2O_7$ composites. The prepared composites were tested for electrochemical fresh and wastewater splitting and supercapacitors. The results indicated the superior performance of $Fe_2P_2O_7$ composite towards OER and HER, displaying the lowest overpotential of 220 and 241 mV at 10 $mA/cm^2$, respectively. In the sense of splitting of wastewater, UOR was carried out and noticed that the as prepared samples showed lower Tafel and higher TOF, contributing to least value of onset potential comparing to OER activity. Thus, The DFT calculations revealed that $Fe_2P_2O_7$ had a higher distribution of DOS over the fermi level than $Co_2P_2O_7$ and $Ni_2P_2O_7$, which improved its electronic characteristics and contributed to its superior electrochemical performances towards OER, HER, and UOR. Furthermore, $Ni_2P_2O_7$, $Co_2P_2O_7$, and $Fe_2P_2O_7$ composites were analysed under the norms of supercapacitor performance and $Ni_2P_2O_7$ achieved highest storage ability with greater specific capacitance of 7986 $mF/cm^2$ at 1 $mA/cm^2$ of current density with significantly improved energy and power density than other samples. This is due to the domination

of diffusion mechanism. Finally, this work can serve as an approach towards understanding of electronic alterations in transition metals via pyrophosphate species to design efficient materials for developing energy conversion and storage.

**References**

[1]  M. Pathak, WORKING GROUP III CONTRIBUTION TO THE IPCC SIXTH ASSESSMENT REPORT (AR6) Technical Summary, Mitig. Clim. Chang. (2021).

[2]  P.R. Shukla, J. Skea, R. Slade, A. Al Khourdajie, R. Van Diemen, D. Mccollum, M. Pathak, S. Some, P. Vyas, R. Fradera, M. Belkacemi, A. Hasija, G. Lisboa, S. Luz, J. Malley, ] Cambridge, M. Grubb, C. Okereke, J. Arima, V. Bosetti, Y. Chen, J. Edmonds, S. Gupta, A. Köberle, Climate Change 2022: Mitigation of Climate Change Working Group III Contribution to the IPCC Sixth Assessment Report Citations Full report Chapter 1, (2022).

[3]  P.T. Anastas, R.L. Lankey, Sustainability through Green Chemistry and Engineering, in: Adv. Sustain. through Green Chem. Eng., American Chemical Society, 2002: p. 1.

[4]  C. Liu, U. Burghaus, F. Besenbacher, Z.L. Wang, Preparation and Characterization of Nanomaterials for Sustainable Energy Production, ACS Nano. 4 (2010) 5517–5526.

[5]  N.S. Lewis, D.G. Nocera, Powering the planet: Chemical challenges in solar energy utilization, Proc. Natl. Acad. Sci. U. S. A. 103 (2006) 15729–15735.

[6]  X. Zou, Y. Zhang, Noble metal-free hydrogen evolution catalysts for water splitting, Chem. Soc. Rev. 44 (2015) 5148–5180.

[7]  M. Balat, Potential importance of hydrogen as a future solution to environmental and transportation problems, Int. J. Hydrogen Energy. 33 (2008) 4013–4029.

[8]  J.-S. Lee, S. Tai Kim, R. Cao, N.-S. Choi, M. Liu, K.T. Lee, J. Cho, Metal–Air Batteries with High Energy Density: Li–Air versus Zn–Air, Adv. Energy Mater. 1 (2011) 34–50.

[9]  B. Zhu, Z. Liang, R. Zou, Designing Advanced Catalysts for Energy Conversion Based on Urea Oxidation Reaction, Small. 16 (2020) 1906133.

[10]  G. Wang, Z. Wen, Self-supported bimetallic Ni–Co compound electrodes for urea- and neutralization energy-assisted electrolytic hydrogen production, Nanoscale. 10 (2018) 21087–21095.

[11]  S.Y. Tee, K.Y. Win, W.S. Teo, L.-D. Koh, S. Liu, C.P. Teng, M.-Y. Han, Recent Progress in Energy-Driven Water Splitting, Adv. Sci. 4 (2017) 1600337.

[12]  A. Ali, D. Najaf, A. Nazir, A. Haider, M. Iqbal, N. Alwadai, A. Kausar, A. Ahmad, Fabrication of Efficient Electrocatalysts for Electrochemical Water

Oxidation Using Bimetallic Oxides System, ACS Omega. 8 (2023) 9539–9546.

[13] P. Babar, A. Lokhande, V. Karade, B. Pawar, M.G. Gang, S. Pawar, J.H. Kim, Bifunctional 2D Electrocatalysts of Transition Metal Hydroxide Nanosheet Arrays for Water Splitting and Urea Electrolysis, ACS Sustain. Chem. Eng. 7 (2019) 10035–10043.

[14] K. Bhunia, M. Chandra, S. Kumar Sharma, D. Pradhan, S.-J. Kim, A critical review on transition metal phosphide based catalyst for electrochemical hydrogen evolution reaction: Gibbs free energy, composition, stability, and true identity of active site, Coord. Chem. Rev. 478 (2023) 214956.

[15] M. Wang, L. Zhang, Y. He, H. Zhu, Recent advances in transition-metal-sulfide-based bifunctional electrocatalysts for overall water splitting, J. Mater. Chem. A. 9 (2021) 5320–5363.

[16] K.C. Majhi, M. Yadav, Transition Metal-Based Chalcogenides as Electrocatalysts for Overall Water Splitting, ACS Eng. Au. 3 (2023) 278–284.

[17] N. Han, M. Race, W. Zhang, R. Marotta, C. Zhang, A. Bokhari, J.J. Klemeš, Perovskite and related oxide based electrodes for water splitting, J. Clean. Prod. 318 (2021) 128544.

[18] T.-Y. Shuai, Q.-N. Zhan, H.-M. Xu, Z.-J. Zhang, G.-R. Li, Recent developments of MXene-based catalysts for hydrogen production by water splitting, Green Chem. 25 (2023) 1749–1789.

[19] F. Ahmad, K. Rafiq, T. Najam, E. Hussain, M. Sohail, M.Z. Abid, A. Mahmood, M.S. Javed, S.S.A. Shah, Metal-organic frameworks for electrocatalytic water-splitting: Beyond the pyrolysis, Int. J. Hydrogen Energy. 48 (2023) 35075–35111.

[20] L. Zhang, J. Xiao, H. Wang, M. Shao, Carbon-Based Electrocatalysts for Hydrogen and Oxygen Evolution Reactions, ACS Catal. 7 (2017) 7855–7865.

[21] D. Khalafallah, J. Miao, M. Zhi, Z. Hong, Structuring graphene quantum dots anchored CuO for high-performance hybrid supercapacitors, J. Taiwan Inst. Chem. Eng. 122 (2021) 168–175.

[22] B. Liu, H.-Q. Peng, C.-N. Ho, H. Xue, S. Wu, T.-W. Ng, C.-S. Lee, W. Zhang, Mesoporous Nanosheet Networked Hybrids of Cobalt Oxide and Cobalt Phosphate for Efficient Electrochemical and Photoelectrochemical Oxygen Evolution, Small. 13 (2017) 1701875.

[23] M. Kristen, S. Hwu, P.O. Box, Synthesis of a Eutectic Halide Flux, Inorg. Chem.

34 (1995) 1495–1499.

[24]  M. Liu, Z. Qu, D. Yin, X. Chen, Y. Zhang, Y. Guo, D. Xiao, Cobalt−Iron Pyrophosphate Porous Nanosheets as Highly Active Electrocatalysts for the Oxygen Evolution Reaction, ChemElectroChem. 5 (2018) 36–43.

[25]  Y. Chang, N.E. Shi, S. Zhao, D. Xu, C. Liu, Y.J. Tang, Z. Dai, Y.Q. Lan, M. Han, J. Bao, Coralloid Co2P2O7 Nanocrystals Encapsulated by Thin Carbon Shells for Enhanced Electrochemical Water Oxidation, ACS Appl. Mater. Interfaces. 8 (2016) 22534–22544.

[26]  H. Du, W. Ai, Z.L. Zhao, Y. Chen, X. Xu, C. Zou, L. Wu, L. Su, K. Nan, T. Yu, C.M. Li, Engineering Morphologies of Cobalt Pyrophosphates Nanostructures toward Greatly Enhanced Electrocatalytic Performance of Oxygen Evolution Reaction, Small. 14 (2018) 1–9.

[27]  X. Zeng, M. Hou, P. Zhu, M. Yuan, S. Ouyang, Q. Lu, C. Zhao, H. Wang, F. Du, G. Zeng, Y. Zhang, g-C3N5-dots as fluorescence probes prepared by an alkali-assisted hydrothermal method for cell imaging, RSC Adv. 12 (2022) 26476–26484.

[28]  J. Choi, C. Zequine, S. Bhoyate, W. Lin, X. Li, P. Kahol, R. Gupta, Waste Coffee Management: Deriving High-Performance Supercapacitors Using Nitrogen-Doped Coffee-Derived Carbon, C. 5 (2019).

[29]  Y. Wang, Y. Song, Y. Xia, Electrochemical capacitors: mechanism, materials, systems, characterization and applications, Chem. Soc. Rev. 45 (2016) 5925–5950.

[30]  L. Zhang, X. Hu, Z. Wang, F. Sun, D.G. Dorrell, A review of supercapacitor modeling, estimation, and applications: A control/management perspective, Renew. Sustain. Energy Rev. 81 (2018) 1868–1878.

[31]  Poonam, K. Sharma, A. Arora, S.K. Tripathi, Review of supercapacitors: Materials and devices, J. Energy Storage. 21 (2019) 801–825.

[32]  N.I. Jalal, R.I. Ibrahim, M.K. Oudah, A review on Supercapacitors: Types and components, J. Phys. Conf. Ser. 1973 (2021).

[33]  Y. Shao, M.F. El-Kady, J. Sun, Y. Li, Q. Zhang, M. Zhu, H. Wang, B. Dunn, R.B. Kaner, Design and Mechanisms of Asymmetric Supercapacitors, Chem. Rev. 118 (2018) 9233–9280.

[34]  Y. Jiao, C. Qu, B. Zhao, Z. Liang, H. Chang, S. Kumar, R. Zou, M. Liu, K.S. Walton, High-Performance Electrodes for a Hybrid Supercapacitor Derived

from a Metal-Organic Framework/Graphene Composite, ACS Appl. Energy Mater. 2 (2019) 5029–5038.

[35]  X. Li, X. Xiao, Q. Li, J. Wei, H. Xue, H. Pang, Metal (M = Co, Ni) phosphate based materials for high-performance supercapacitors, Inorg. Chem. Front. 5 (2018) 11–28.

[36]  S.J. Marje, P.K. Katkar, S.S. Pujari, S.A. Khalate, A.C. Lokhande, U.M. Patil, Regulated micro-leaf like nickel pyrophosphate as a cathode electrode for asymmetric supercapacitor, Synth. Met. 259 (2020) 116224.

[37]  Q. Zong, C. Liu, H. Yang, Q. Zhang, G. Cao, Tailoring nanostructured transition metal phosphides for high-performance hybrid supercapacitors, Nano Today. 38 (2021) 101201.

[38]  I. Ahmed, C.A. Collins, M.P. Lewis, I. Olsen, J.C. Knowles, Processing, characterisation and biocompatibility of iron-phosphate glass fibres for tissue engineering., Biomaterials. 25 (2004) 3223–3232.

[39]  Z. Khan, B. Senthilkumar, S. Lim, R. Shanker, Y. Kim, H. Ko, Redox-Additive-Enhanced High Capacitance Supercapacitors Based on Co2P2O7 Nanosheets, Adv. Mater. Interfaces. 4 (2017) 1700059.

[40]  D. Khalafallah, W. Huang, M. Zhi, Z. Hong, Synergistic Tuning of Nickel Cobalt Selenide@Nickel Telluride Core–Shell Heteroarchitectures for Boosting Overall Urea Electrooxidation and Electrochemical Supercapattery, ENERGY Environ. Mater. n/a (2022) e12528.

[41]  D. Liang, C. Lian, Q. Xu, M. Liu, H. Liu, H. Jiang, C. Li, Interfacial charge polarization in Co2P2O7@N, P co-doped carbon nanocages as Mott-Schottky electrocatalysts for accelerating oxygen evolution reaction, Appl. Catal. B Environ. 268 (2020) 118417.

[42]  D. khalafallah, C. Ouyang, M.A. Ehsan, M. Zhi, Z. Hong, Complexing of NixMny sulfides microspheres via a facile solvothermal approach as advanced electrode materials with excellent charge storage performances, Int. J. Hydrogen Energy. 45 (2020) 6885–6896.

[43]  N.-D. Huynh, W.M. Choi, S.H. Hur, Exploring the Effects of Various Two-Dimensional Supporting Materials on the Water Electrolysis of Co-Mo Sulfide/Oxide Heterostructure, Nanomaterials. 13 (2023).

[44]  S. Liu, C. Gu, H. Wang, R. Liu, H. Wang, J. He, Effect of symbiotic compound Fe2P2O7 on electrochemical performance of LiFePO4/C cathode materials, J.

Alloys Compd. 646 (2015) 233–237.

[45] G.H. Lee, S.D. Seo, H.W. Shim, K.S. Park, D.W. Kim, Synthesis and Li electroactivity of Fe 2P 2O 7 microspheres composed of self-assembled nanorods, Ceram. Int. 38 (2012) 6927–6930.

[46] X. Xie, G. Hu, Y. Cao, K. Du, Z. Gan, L. Xu, Y. Wang, Z. Peng, Rheological phase synthesis of Fe 2 P 2 O 7 /C composites as the precursor to fabricate high performance LiFePO 4 /C composites for lithium-ion batteries, Ceram. Int. 45 (2019) 12331–12336.

[47] H. Li, T. Liu, Y. He, J. Song, A. Meng, C. Sun, M. Hu, L. Wang, G. Li, Z. Zhang, Y. Liu, J. Zhao, Z. Li, Interfacial Engineering and a Low-Crystalline Strategy for High-Performance Supercapacitor Negative Electrodes: Fe2P2O7 Nanoplates Anchored on N/P Co-doped Graphene Nanotubes, ACS Appl. Mater. Interfaces. 14 (2022) 3363–3373.

[48] Fe2P2O7-XRD-04.pdf, (n.d.).

[49] J. Zhang, P. Liu, R. Bu, H. Zhang, Q. Zhang, K. Liu, Y. Liu, Z. Xiao, L. Wang, In situ fabrication of a rose-shaped Co2P2O7/C nanohybrid via a coordination polymer template for supercapacitor application, New J. Chem. 44 (2020) 12514–12521.

[50] A. Agarwal, S. Majumder, B.R. Sankapal, Carbon Nanotube-Functionalized Surface-Assisted Growth of Cobalt Phosphate Nanodots: A Highly Stable and Bendable All-Solid-State Symmetric Supercapacitor, Energy and Fuels. 36 (2022) 5953–5964.

[51] Y. Zhu, T. Xie, S. Zhang, N. Zhang, G. Wang, P. Feng, H. Xu, K. Lv, A sandwich structure of cobalt pyrophosphate/nickel phosphite@C: one step synthesis and its good electrocatalytic performance, J. Solid State Electrochem. 26 (2022) 1221–1230.

[52] S. Surendran, A. Sivanantham, S. Shanmugam, U. Sim, R. Kalai Selvan, Ni2P2O7 microsheets as efficient Bi-functional electrocatalysts for water splitting application, Sustain. Energy Fuels. 3 (2019) 2435–2446.

[53] P. Matheswaran, P. Karuppiah, S.-M. Chen, P. Thangavelu, A binder-free Ni2P2O7/Co2P2O7 nanograss array as an efficient cathode for supercapacitors, New J. Chem. 44 (2020) 13131–13140.

[54] P. Matheswaran, P. Karuppiah, S.-M. Chen, P. Thangavelu, B. Ganapathi, Fabrication of g-C3N4 Nanomesh-Anchored Amorphous NiCoP2O7: Tuned

Cycling Life and the Dynamic Behavior of a Hybrid Capacitor, ACS Omega. 3 (2018) 18694–18704.

[55] P. Sharma, S. Radhakrishnan, M.-S. Khil, H.-Y. Kim, B.-S. Kim, Simple room temperature synthesis of porous nickel phosphate foams for electrocatalytic ethanol oxidation, J. Electroanal. Chem. 808 (2018) 236–244.

[56] A.G. Meguerdichian, T. Jafari, M.R. Shakil, R. Miao, L.A. Achola, J. Macharia, A. Shirazi-Amin, S.L. Suib, Synthesis and Electrocatalytic Activity of Ammonium Nickel Phosphate, [NH4]NiPO4·6H2O, and β-Nickel Pyrophosphate, β-Ni2P2O7: Catalysts for Electrocatalytic Decomposition of Urea, Inorg. Chem. 57 (2018) 1815–1823.

[57] H. Pang, Y.-Z. Zhang, Z. Run, W.-Y. Lai, W. Huang, Amorphous nickel pyrophosphate microstructures for high-performance flexible solid-state electrochemical energy storage devices, Nano Energy. 17 (2015) 339–347.

[58] A.P. Grosvenor, M.C. Biesinger, R.S.C. Smart, N.S. McIntyre, New interpretations of XPS spectra of nickel metal and oxides, Surf. Sci. 600 (2006) 1771–1779.

[59] A.A. Mirghni, M.J. Madito, K.O. Oyedotun, T.M. Masikhwa, N.M. Ndiaye, S.J. Ray, N. Manyala, A high energy density asymmetric supercapacitor utilizing a nickel phosphate/graphene foam composite as the cathode and carbonized iron cations adsorbed onto polyaniline as the anode., RSC Adv. 8 (2018) 11608–11621.

[60] Y. Li, C. Zhao, Iron-Doped Nickel Phosphate as Synergistic Electrocatalyst for Water Oxidation, Chem. Mater. 28 (2016) 5659–5666.

[61] B. Senthilkumar, Z. Khan, S. Park, K. Kim, H. Ko, Y. Kim, Highly porous graphitic carbon and Ni2P2O7 for a high performance aqueous hybrid supercapacitor, J. Mater. Chem. A. 3 (2015) 21553–21561.

[62] H. Liu, H. Li, X. Wang, Electrostatic Interaction-Directed Growth of Nickel Phosphate Single-Walled Nanotubes for High Performance Oxygen Evolution Reaction Catalysts, Small. 12 (2016) 2969–2974.

[63] I. V Odynets, N.Y. Strutynska, J. Li, W. Han, I. V Zatovsky, N.I. Klyui, CoOx(OH)y/C nanocomposites in situ derived from Na4Co3(PO4)2P2O7 as sustainable electrocatalysts for water splitting, Dalt. Trans. 47 (2018) 15703–15713.

[64] Y. Han, J. Lin, H. Zhou, L. Guo, Y. Wang, Self-standing Co2P2O7@N-doped

carbon/carbon foams for hydrogen evolution reaction in alkaline medium, Diam. Relat. Mater. 135 (2023) 109843.

[65] X. Wang, L. Zhuang, T. He, Y. Jia, L. Zhang, X. Yan, M. Gao, A. Du, Z. Zhu, X. Yao, S.-H. Yu, Grafting Cobalt Diselenide on Defective Graphene for Enhanced Oxygen Evolution Reaction, IScience. 7 (2018) 145–153.

[66] A.P. Grosvenor, B.A. Kobe, M.C. Biesinger, N.S. McIntyre, Investigation of multiplet splitting of Fe 2p XPS spectra and bonding in iron compounds, Surf. Interface Anal. 36 (2004) 1564–1574.

[67] J. Wang, J. Huang, S. Zhao, I.P. Parkin, Z. Tian, F. Lai, T. Liu, G. He, Mo/Fe bimetallic pyrophosphates derived from Prussian blue analogues for rapid electrocatalytic oxygen evolution, Green Energy Environ. 8 (2023) 1450–1458.

[68] P.C.J. Graat, M.A.J. Somers, Simultaneous determination of composition and thickness of thin iron-oxide films from XPS Fe 2p spectra, Appl. Surf. Sci. 100– 101 (1996) 36–40.

[69] Ni2P2O7-FTIR.pdf, (n.d.).

[70] N. Zhang, C. Chen, Y. Chen, G. Chen, C. Liao, B. Liang, J. Zhang, A. Li, B. Yang, Z. Zheng, X. Liu, A. Pan, S. Liang, R. Ma, Ni2P2O7 Nanoarrays with Decorated C3N4 Nanosheets as Efficient Electrode for Supercapacitors, ACS Appl. Energy Mater. 1 (2018) 2016–2023.

[71] S. Kaoua, S. Krimi, S. Péchev, P. Gravereau, J.-P. Chaminade, M. Couzi, A. El Jazouli, Synthesis, crystal structure, and vibrational spectroscopic and UV– visible studies of Cs2MnP2O7, J. Solid State Chem. 198 (2013) 379–385.

[72] B. Boonchom, N. Vittayakorn, Synthesis and ferromagnetic property of new binary copper iron pyrophosphate CuFeP2O7, Mater. Lett. 64 (2010) 275–277.

[73] F. Bao, E. Kemppainen, I. Dorbandt, R. Bors, F. Xi, R. Schlatmann, R. van de Krol, S. Calnan, Understanding the Hydrogen Evolution Reaction Kinetics of Electrodeposited Nickel-Molybdenum in Acidic, Near-Neutral, and Alkaline Conditions, ChemElectroChem. 8 (2021) 195–208.

[74] H. Prats, K. Chan, The determination of the HOR/HER reaction mechanism from experimental kinetic data, Phys. Chem. Chem. Phys. 23 (2021) 27150–27158.

[75] H. Fan, H. Yu, Y. Zhang, Y. Zheng, Y. Luo, Z. Dai, B. Li, Y. Zong, Q. Yan, Fe-Doped Ni3C Nanodots in N-Doped Carbon Nanosheets for Efficient Hydrogen-Evolution and Oxygen-Evolution Electrocatalysis, Angew. Chemie Int. Ed. 56 (2017) 12566–12570.

[76] J. Zhu, L. Hu, P. Zhao, L.Y.S. Lee, K.-Y. Wong, Recent Advances in Electrocatalytic Hydrogen Evolution Using Nanoparticles, Chem. Rev. 120 (2020) 851–918.

[77] R. Guidelli, R.G. Compton, J.M. Feliu, E. Gileadi, J. Lipkowski, W. Schmickler, S. Trasatti, Defining the transfer coefficient in electrochemistry: An assessment (IUPAC Technical Report), Pure Appl. Chem. 86 (2014) 245–258.

[78] S. Haghighat, J.M. Dawlaty, pH Dependence of the Electron-Transfer Coefficient: Comparing a Model to Experiment for Hydrogen Evolution Reaction, J. Phys. Chem. C. 120 (2016) 28489–28496.

[79] I. Paseka, Influence of hydrogen absorption in amorphous Ni–P electrodes on double layer capacitance and charge transfer coefficient of hydrogen evolution reaction, Electrochim. Acta. 44 (1999) 4551–4558.

[80] S. Anantharaj, S.R. Ede, K. Karthick, S. Sam Sankar, K. Sangeetha, P.E. Karthik, S. Kundu, Precision and correctness in the evaluation of electrocatalytic water splitting: revisiting activity parameters with a critical assessment, Energy Environ. Sci. 11 (2018) 744–771.

[81] M. Videa, D. Crespo, G. Casillas, G. Zavala, Electrodeposition of nickel-molybdenum nanoparticles for their use as electrocatalyst for the hydrogen evolution reaction, J. New Mater. Electrochem. Syst. 13 (2010) 239–244.

[82] R.S. Situmorang, O. Seri, H. Kawai, Estimation of exchange current density for hydrogen evolution reaction of copper electrode by using the differentiating polarization method, Appl. Surf. Sci. 505 (2020) 144300.

[83] Y. Chen, Q. Zhao, Y. Yao, T. Li, The preparation of ionic liquid based iron phosphate/CNTs composite via microwave radiation for hydrogen evolution reaction and oxygen evolution reaction, Arab. J. Chem. 14 (2021) 103440.

[84] C. Lv, Z. Peng, Y. Zhao, Z. Huang, C. Zhang, The hierarchical nanowires array of iron phosphide integrated on a carbon fiber paper as an effective electrocatalyst for hydrogen generation, J. Mater. Chem. A. 4 (2016) 1454–1460.

[85] J. Yang, D. Voiry, S.J. Ahn, D. Kang, A.Y. Kim, M. Chhowalla, H.S. Shin, Two-dimensional hybrid nanosheets of tungsten disulfide and reduced graphene oxide as catalysts for enhanced hydrogen evolution., Angew. Chem. Int. Ed. Engl. 52 (2013) 13751–13754.

[86] P.D. Tran, M. Nguyen, S.S. Pramana, A. Bhattacharjee, S.Y. Chiam, J. Fize, M.J. Field, V. Artero, L.H. Wong, J. Loo, J. Barber, Copper molybdenum sulfide: a

new efficient electrocatalyst for hydrogen production from water, Energy Environ. Sci. 5 (2012) 8912–8916.

[87] P.D. Tran, S.Y. Chiam, P.P. Boix, Y. Ren, S.S. Pramana, J. Fize, V. Artero, J. Barber, Novel cobalt/nickel–tungsten-sulfide catalysts for electrocatalytic hydrogen generation from water, Energy Environ. Sci. 6 (2013) 2452–2459.

[88] R. Srivastava, S. Bhardwaj, A. Kumar, A.N. Robinson, J. Sultana, S.R. Mishra, F. Perez, R.K. Gupta, International Journal of Hydrogen Energy Bimetallic MnNi-hydroxide electrodeposited on Ni-foam for superior water-splitting and energy storage, Int. J. Hydrogen Energy. (2023) 1–13.

[89] A. Gupta, C.A. Allison, A. Kumar, R. Srivastava, W. Lin, J. Sultana, S.R. Mishra, F. Perez, R.K. Gupta, T. Dawsey, Tuned morphology configuration to augment the electronic structure and durability of iron phosphide for efficient bifunctional electrocatalysis and charge storage, J. Energy Storage. 73 (2023) 108824.

[90] C.A. Allison, A. Gupta, A. Kumar, R. Srivastava, W. Lin, J. Sultana, S.R. Mishra, F. Perez, R.K. Gupta, T. Dawsey, Phase modification of cobalt-based structures for improvement of catalytic activities and energy storage, Electrochim. Acta. 465 (2023) 143023.

[91] S. Bhardwaj, R. Srivastava, T. Mageto, M. Chaudhari, A. Kumar, J. Sultana, S.R. Mishra, F. Perez, R.K. Gupta, Bimetallic Co–Fe sulfide and phosphide as efficient electrode materials for overall water splitting and supercapacitor, Discov. Nano. 18 (2023).

[92] L. Yang, Z. Guo, J. Huang, Y. Xi, R. Gao, G. Su, W. Wang, L. Cao, B. Dong, Vertical Growth of 2D Amorphous FePO4 Nanosheet on Ni Foam: Outer and Inner Structural Design for Superior Water Splitting, Adv. Mater. 29 (2017) 1704574.

[93] J. Quiñonero, T. Lana-Villarreal, R. Gómez, Tuning the oxygen evolution reaction activity of Ni- and Co-modified Fe(OH)2 electrodes through structure and composition control, Int. J. Hydrogen Energy. 45 (2020) 17076–17087.

[94] F. Song, L. Bai, A. Moysiadou, S. Lee, C. Hu, L. Liardet, X. Hu, Transition Metal Oxides as Electrocatalysts for the Oxygen Evolution Reaction in Alkaline Solutions: An Application-Inspired Renaissance, J. Am. Chem. Soc. 140 (2018) 7748–7759.

[95] J.R. Macdonald, W.B. Johnson, Fundamentals of Impedance Spectroscopy, in:

Impedance Spectrosc., 2005: pp. 1–26.

[96] B.-A. Mei, J. Lau, T. Lin, S.H. Tolbert, B.S. Dunn, L. Pilon, Physical Interpretations of Electrochemical Impedance Spectroscopy of Redox Active Electrodes for Electrical Energy Storage, J. Phys. Chem. C. 122 (2018) 24499–24511.

[97] A. Lasia, Electrochemical Impedance Spectroscopy and its Applications BT - Modern Aspects of Electrochemistry, Mod. Asp. Electrochem. 32 (2002) 143–248. http://dx.doi.org/10.1007/0-306-46916-2_2%5Cnpapers2://publication/doi/10.1007/0-306-46916-2_2.

[98] H.S. Magar, R.Y.A. Hassan, A. Mulchandani, Electrochemical impedance spectroscopy (Eis): Principles, construction, and biosensing applications, Sensors. 21 (2021).

[99] N.O. Laschuk, E.B. Easton, O. V Zenkina, Reducing the resistance for the use of electrochemical impedance spectroscopy analysis in materials chemistry, RSC Adv. 11 (2021) 27925–27936.

[100] K. Akbar, J.H. Jeon, M. Kim, J. Jeong, Y. Yi, S.H. Chun, Bifunctional Electrodeposited 3D NiCoSe2/Nickle Foam Electrocatalysts for Its Applications in Enhanced Oxygen Evolution Reaction and for Hydrazine Oxidation, ACS Sustain. Chem. Eng. 6 (2018) 7735–7742.

[101] J. Nai, H. Yin, T. You, L. Zheng, J. Zhang, P. Wang, Z. Jin, Y. Tian, J. Liu, Z. Tang, L. Guo, Efficient Electrocatalytic Water Oxidation by Using Amorphous Ni–Co Double Hydroxides Nanocages, Adv. Energy Mater. 5 (2015) 1401880.

[102] Q. Liu, H. Zhao, M. Jiang, Q. Kang, W. Zhou, P. Wang, F. Zhou, Boron enhances oxygen evolution reaction activity over Ni foam-supported iron boride nanowires, J. Mater. Chem. A. 8 (2020) 13638–13645.

[103] H. Yang, Y. Huang, W.Y. Teoh, L. Jiang, W. Chen, L. Zhang, J. Yan, Molybdenum Selenide nanosheets Surrounding nickel Selenides Sub-microislands on nickel foam as high-performance bifunctional electrocatalysts for water Splitting, Electrochim. Acta. 349 (2020) 136336.

[104] S.B. Jung, M.J. Choi, D. Ryu, H.S. Yi, S.E. Lee, J.Y. Chang, H.K. Chung, Y.K. Kim, S.G. Kang, J.H. Lee, K.S. Kim, H.J. Kim, C.S. Kim, C.H. Lee, R.W. Williams, H. Kim, H.K. Lee, J. Auwerx, M. Shong, Reduced oxidative capacity in macrophages results in systemic insulin resistance, Nat. Commun. 9 (2018).

[105] J. Hou, B. Zhang, Z. Li, S. Cao, Y. Sun, Y. Wu, Z. Gao, L. Sun, Vertically

Aligned Oxygenated-CoS2–MoS2 Heteronanosheet Architecture from Polyoxometalate for Efficient and Stable Overall Water Splitting, ACS Catal. 8 (2018) 4612–4621.

[106] Z. Dai, H. Geng, J. Wang, Y. Luo, B. Li, Y. Zong, J. Yang, Y. Guo, Y. Zheng, X. Wang, Q. Yan, Hexagonal-Phase Cobalt Monophosphosulfide for Highly Efficient Overall Water Splitting, ACS Nano. 11 (2017) 11031–11040.

[107] P. Wang, Z. Pu, W. Li, J. Zhu, C. Zhang, Y. Zhao, S. Mu, Coupling NiSe2-Ni2P heterostructure nanowrinkles for highly efficient overall water splitting, J. Catal. 377 (2019) 600–608.

[108] B. Zhang, X. Zheng, O. Voznyy, R. Comin, M. Bajdich, M. García-Melchor, L. Han, J. Xu, M. Liu, L. Zheng, F.P. García de Arquer, C.T. Dinh, F. Fan, M. Yuan, E. Yassitepe, N. Chen, T. Regier, P. Liu, Y. Li, P. De Luna, A. Janmohamed, H.L. Xin, H. Yang, A. Vojvodic, E.H. Sargent, Homogeneously dispersed multimetal oxygen-evolving catalysts., Science. 352 (2016) 333–337.

[109] N. Jiang, B. You, M. Sheng, Y. Sun, Electrodeposited cobalt-phosphorous-derived films as competent bifunctional catalysts for overall water splitting., Angew. Chem. Int. Ed. Engl. 54 (2015) 6251–6254.

[110] L. Yu, H. Zhou, J. Sun, F. Qin, F. Yu, J. Bao, Y. Yu, S. Chen, Z. Ren, Cu nanowires shelled with NiFe layered double hydroxide nanosheets as bifunctional electrocatalysts for overall water splitting, Energy Environ. Sci. 10 (2017) 1820–1827.

[111] W. Liu, K. Du, L. Liu, J. Zhang, Z. Zhu, Y. Shao, M. Li, One-step electroreductively deposited iron-cobalt composite films as efficient bifunctional electrocatalysts for overall water splitting, Nano Energy. 38 (2017) 576–584.

[112] A. Dutta, A.K. Samantara, S.K. Dutta, B.K. Jena, N. Pradhan, Surface-Oxidized Dicobalt Phosphide Nanoneedles as a Nonprecious, Durable, and Efficient OER Catalyst, ACS Energy Lett. 1 (2016) 169–174.

[113] P. Chen, T. Zhou, M. Zhang, Y. Tong, C. Zhong, N. Zhang, L. Zhang, C. Wu, Y. Xie, 3D Nitrogen-Anion-Decorated Nickel Sulfides for Highly Efficient Overall Water Splitting, Adv. Mater. 29 (2017) 1701584.

[114] X. Wei, Y. Zhang, H. He, L. Peng, S. Xiao, S. Yao, P. Xiao, Carbon-incorporated porous honeycomb NiCoFe phosphide nanospheres derived from a MOF precursor for overall water splitting, Chem. Commun. 55 (2019) 10896–10899.

[115] N. Ashokan, Iron phosphide nanostructures as an efficient bifunctional catalysts

for water splitting, (2016) 41.

[116] Y. Yan, B.Y. Xia, X. Ge, Z. Liu, A. Fisher, X. Wang, A Flexible Electrode Based on Iron Phosphide Nanotubes for Overall Water Splitting, Chem. – A Eur. J. 21 (2015) 18062–18067.

[117] C.-C. Hou, S. Cao, W.-F. Fu, Y. Chen, Ultrafine CoP Nanoparticles Supported on Carbon Nanotubes as Highly Active Electrocatalyst for Both Oxygen and Hydrogen Evolution in Basic Media, ACS Appl. Mater. Interfaces. 7 (2015) 28412–28419.

[118] N. Jiang, B. You, M. Sheng, Y. Sun, Bifunctionality and Mechanism of Electrodeposited Nickel–Phosphorous Films for Efficient Overall Water Splitting, ChemCatChem. 8 (2016) 106–112.

[119] A. Mendoza-Garcia, H. Zhu, Y. Yu, Q. Li, L. Zhou, D. Su, M.J. Kramer, S. Sun, Controlled Anisotropic Growth of Co-Fe-P from Co-Fe-O Nanoparticles., Angew. Chem. Int. Ed. Engl. 54 (2015) 9642–9645.

[120] A. Sivanantham, P. Ganesan, S. Shanmugam, Hierarchical NiCo2S4 Nanowire Arrays Supported on Ni Foam: An Efficient and Durable Bifunctional Electrocatalyst for Oxygen and Hydrogen Evolution Reactions, Adv. Funct. Mater. 26 (2016) 4661–4672.

[121] J. Luo, J.H. Im, M.T. Mayer, M. Schreier, M.K. Nazeeruddin, N.G. Park, S.D. Tilley, H.J. Fan, M. Grätzel, Water photolysis at 12.3% efficiency via perovskite photovoltaics and Earth-abundant catalysts, Science (80-. ). 345 (2014) 1593–1596.

[122] K. Zeng, D. Zhang, Recent progress in alkaline water electrolysis for hydrogen production and applications, Prog. Energy Combust. Sci. 36 (2010) 307–326.

[123] S.A. Patil, N.K. Shrestha, A.I. Inamdar, C. Bathula, J. Jung, S. Hussain, G. Nazir, M. Kaseem, H. Im, H. Kim, Bimetallic Cu/Fe MOF-Based Nanosheet Film via Binder-Free Drop-Casting Route: A Highly Efficient Urea-Electrolysis Catalyst, Nanomaterials. 12 (2022).

[124] L. Sha, T. Liu, K. Ye, K. Zhu, J. Yan, J. Yin, G. Wang, D. Cao, A heterogeneous interface on NiS@Ni3S2/NiMoO4 heterostructures for efficient urea electrolysis, J. Mater. Chem. A. 8 (2020) 18055–18063.

[125] Z. Wang, W. Liu, Y. Hu, M. Guan, L. Xu, H. Li, J. Bao, H. Li, Cr-doped CoFe layered double hydroxides: Highly efficient and robust bifunctional electrocatalyst for the oxidation of water and urea, Appl. Catal. B Environ. 272

(2020) 118959.

[126] L. Wang, Y. Zhu, Y. Wen, S. Li, C. Cui, F. Ni, Y. Liu, H. Lin, Y. Li, H. Peng, B. Zhang, Regulating the Local Charge Distribution of Ni Active Sites for the Urea Oxidation Reaction, Angew. Chemie Int. Ed. 60 (2021) 10577–10582.

[127] C. Wang, H. Lu, Z. Mao, C. Yan, G. Shen, X. Wang, Bimetal Schottky Heterojunction Boosting Energy-Saving Hydrogen Production from Alkaline Water via Urea Electrocatalysis, Adv. Funct. Mater. 30 (2020) 2000556.

[128] L. Zhang, L. Wang, H. Lin, Y. Liu, J. Ye, Y. Wen, A. Chen, L. Wang, F. Ni, Z. Zhou, S. Sun, Y. Li, B. Zhang, H. Peng, A Lattice-Oxygen-Involved Reaction Pathway to Boost Urea Oxidation, Angew. Chemie Int. Ed. 58 (2019) 16820–16825.

[129] L. Fei, H. Sun, R. Ran, W. Zhou, Z. Shao, Self-Supported Nickel Phosphide Electrode for Efficient Alkaline Water-to-Hydrogen Conversion via Urea Electrolysis, Ind. Eng. Chem. Res. 60 (2021) 1185–1193.

[130] X. Meng, M. Wang, Y. Zhang, Z. Li, X. Ding, W. Zhang, C. Li, Z. Li, Superimposed OER and UOR performances by the interaction of each component in an Fe–Mn electrocatalyst, Dalt. Trans. 51 (2022) 16605–16611.

[131] C. Xiao, S. Li, X. Zhang, D.R. MacFarlane, MnO2/MnCo2O4/Ni heterostructure with quadruple hierarchy: a bifunctional electrode architecture for overall urea oxidation, J. Mater. Chem. A. 5 (2017) 7825–7832.

[132] S. Chen, J. Duan, A. Vasileff, S.Z. Qiao, Size Fractionation of Two-Dimensional Sub-Nanometer Thin Manganese Dioxide  Crystals towards Superior Urea Electrocatalytic Conversion., Angew. Chem. Int. Ed. Engl. 55 (2016) 3804–3808.

[133] S. Hu, C. Feng, S. Wang, J. Liu, H. Wu, L. Zhang, J. Zhang, Ni3N/NF as Bifunctional Catalysts for Both Hydrogen Generation and Urea Decomposition, ACS Appl. Mater. Interfaces. 11 (2019) 13168–13175.

[134] J. Xie, H. Qu, F. Lei, X. Peng, W. Liu, L. Gao, P. Hao, G. Cui, B. Tang, Partially amorphous nickel–iron layered double hydroxide nanosheet arrays for robust bifunctional electrocatalysis, J. Mater. Chem. A. 6 (2018) 16121–16129.

[135] J. Li, C. Yao, X. Kong, Z. Li, M. Jiang, F. Zhang, X. Lei, Boosting Hydrogen Production by Electrooxidation of Urea over 3D Hierarchical Ni4N/Cu3N Nanotube Arrays, ACS Sustain. Chem. Eng. 7 (2019) 13278–13285.

[136] M. Yang, Y. Jiang, M. Qu, Y. Qin, Y. Wang, W. Shen, R. He, W. Su, M. Li,

Strong electronic couple engineering of transition metal phosphides-oxides heterostructures as multifunctional electrocatalyst for hydrogen production, Appl. Catal. B Environ. 269 (2020) 118803.

[137] X. Ji, Y. Zhang, Z. Ma, Y. Qiu, Oxygen Vacancy-rich Ni/NiO@NC Nanosheets with Schottky Heterointerface for Efficient Urea Oxidation Reaction, ChemSusChem. 13 (2020) 5004–5014.

[138] D. Zhu, C. Guo, J. Liu, L. Wang, Y. Du, S.-Z. Qiao, Two-dimensional metal–organic frameworks with high oxidation states for efficient electrocatalytic urea oxidation, Chem. Commun. 53 (2017) 10906–10909.

[139] L. Yan, Y. Sun, E. Hu, J. Ning, Y. Zhong, Z. Zhang, Y. Hu, Facile in-situ growth of Ni 2 P/Fe 2 P nanohybrids on Ni foam for highly efficient urea electrolysis, J. Colloid Interface Sci. 541 (2019) 279–286.

[140] Z.-Y. Yu, C.-C. Lang, M.-R. Gao, Y. Chen, Q.-Q. Fu, Y. Duan, S.-H. Yu, Ni–Mo–O nanorod-derived composite catalysts for efficient alkaline water-to-hydrogen conversion via urea electrolysis, Energy Environ. Sci. 11 (2018) 1890–1897.

[141] F. Wu, G. Ou, J. Yang, H. Li, Y. Gao, F. Chen, Y. Wang, Y. Shi, Bifunctional nickel oxide-based nanosheets for highly efficient overall urea splitting, Chem. Commun. 55 (2019) 6555–6558.

[142] J.-J. Zhang, W.-W. Bao, M.-Y. Li, C.-M. Yang, N.-N. Zhang, Ultrafast formation of an FeOOH electrocatalyst on Ni for efficient alkaline water and urea oxidation, Chem. Commun. 56 (2020) 14713–14716.

[143] Y. Wang, Y. Li, L. Ding, J. Ding, A facile oxidation–dehydration reaction-driven robust porous copper oxide nanobelt coating on copper foam for an energy-saving and low-cost urea oxidization reaction, Chem. Commun. 55 (2019) 13562–13565.

[144] M.-S. Wu, C.-Y. Jao, F.-Y. Chuang, F.-Y. Chen, Carbon-encapsulated nickel-iron nanoparticles supported on nickel foam as a catalyst electrode for urea electrolysis, Electrochim. Acta. 227 (2017) 210–216.

[145] W. Zhang, Q. Jia, H. Liang, L. Cui, D. Wei, J. Liu, Iron doped Ni3S2 nanorods directly grown on FeNi3 foam as an efficient bifunctional catalyst for overall water splitting, Chem. Eng. J. 396 (2020) 125315.

[146] S. Wei, X. Wang, J. Wang, X. Sun, L. Cui, W. Yang, Y. Zheng, J. Liu, CoS2 nanoneedle array on Ti mesh: A stable and efficient bifunctional electrocatalyst

for urea-assisted electrolytic hydrogen production, Electrochim. Acta. 246 (2017) 776–782.

[147] J. Meng, P. Chernev, M.R. Mohammadi, K. Klingan, S. Loos, C. Pasquini, P. Kubella, S. Jiang, X. Yang, Z. Cui, S. Zhu, Z. Li, Y. Liang, H. Dau, Self-supported Ni(OH)2/MnO2 on CFP as a flexible anode towards electrocatalytic urea conversion: The role of composition on activity, redox states and reaction dynamics, Electrochim. Acta. 318 (2019) 32–41.

[148] N.A.M. Barakat, M. Alajami, Z.K. Ghouri, S. Al-Meer, Effective NiMn Nanoparticles-Functionalized Carbon Felt as an Effective Anode for Direct Urea Fuel Cells., Nanomater. (Basel, Switzerland). 8 (2018).

[149] W. Zhu, Z. Yue, W. Zhang, N. Hu, Z. Luo, M. Ren, Z. Xu, Z. Wei, Y. Suo, J. Wang, Wet-chemistry topotactic synthesis of bimetallic iron–nickel sulfide nanoarrays: an advanced and versatile catalyst for energy efficient overall water and urea electrolysis, J. Mater. Chem. A. 6 (2018) 4346–4353.

[150] Y. Pei, Y. Cheng, J. Chen, W. Smith, P. Dong, P.M. Ajayan, M. Ye, J. Shen, Recent developments of transition metal phosphides as catalysts in the energy conversion field, J. Mater. Chem. A. 6 (2018) 23220–23243.

[151] R. V Mom, J. Cheng, M.T.M. Koper, M. Sprik, Modeling the Oxygen Evolution Reaction on Metal Oxides: The Infuence of Unrestricted DFT Calculations, J. Phys. Chem. C. 118 (2014) 4095–4102.

[152] V. Tripković, E. Skúlason, S. Siahrostami, J.K. Nørskov, J. Rossmeisl, The oxygen reduction reaction mechanism on Pt(111) from density functional theory calculations, Electrochim. Acta. 55 (2010) 7975–7981.

[153] J. Ge, Z. Liu, M. Guan, J. Kuang, Y. Xiao, Y. Yang, C.H. Tsang, X. Lu, C. Yang, Investigation of the electrocatalytic mechanisms of urea oxidation reaction on the surface of transition metal oxides., J. Colloid Interface Sci. 620 (2022) 442–453.

[154] C. Shi, Q. Zhao, H. Li, Z.M. Liao, D. Yu, Low cost and flexible mesh-based supercapacitors for promising large-area flexible/wearable energy storage, Nano Energy. 6 (2014) 82–91.

[155] L. Hou, L. Lian, D. Li, J. Lin, G. Pan, L. Zhang, X. Zhang, Q. Zhang, C. Yuan, Facile synthesis of Co2P2O7 nanorods as a promising pseudocapacitive material towards high-performance electrochemical capacitors, RSC Adv. 3 (2013) 21558–21562.

[156] Y. Zhou, C. Liu, X. Li, L. Sun, D. Wu, J. Li, P. Huo, H. Wang, Chemical precipitation synthesis of porous Ni2P2O7 nanowires for supercapacitor, J. Alloys Compd. 790 (2019) 36–41.

[157] Z. Khan, B. Senthilkumar, S. Lim, R. Shanker, Y. Kim, H. Ko, Redox-Additive-Enhanced High Capacitance Supercapacitors Based on Co2P2O7 Nanosheets, Adv. Mater. Interfaces. 4 (2017) 1–7.

[158] A.A. Kulkarni, V.A. Savekar, T.S. Bhat, P.S. Patil, Recent advances in metal pyrophosphates for electrochemical supercapacitors: A review, J. Energy Storage. 52 (2022) 104986.

[159] K.V. Sankar, R.K. Selvan, D. Meyrick, Electrochemical performances of CoFe2O4 nanoparticles and a rGO based asymmetric supercapacitor, RSC Adv. 5 (2015) 99959–99967.

[160] N. Yu, K. Guo, W. Zhang, X. Wang, M.Q. Zhu, Flexible high-energy asymmetric supercapacitors based on MnO@C composite nanosheet electrodes, J. Mater. Chem. A. 5 (2017) 804–813.

[161] F. Paquin, J. Rivnay, A. Salleo, N. Stingelin, C. Silva, Multi-phase semicrystalline microstructures drive exciton dissociation in neat plastic semiconductors, J. Mater. Chem. C. 3 (2015) 10715–10722.

[162] P. Matheswaran, P. Karuppiah, S.M. Chen, P. Thangavelu, A binder-free Ni2P2O7/Co2P2O7nanograss array as an efficient cathode for supercapacitors, New J. Chem. 44 (2020) 13131–13140.

[163] C. Zhao, S. Wang, Z. Zhu, P. Ju, C. Zhao, X. Qian, Roe-shaped Ni3(PO4)2/RGO/Co3(PO4)2 (NRC) nanocomposite grown: In situ on Co foam for superior supercapacitors, J. Mater. Chem. A. 5 (2017) 18594–18602.

[164] K.V. Sankar, R.K. Selvan, The ternary MnFe2O4/graphene/polyaniline hybrid composite as negative electrode for supercapacitors, J. Power Sources. 275 (2015) 399–407.

[165] N. Zhang, C. Chen, Y. Chen, G. Chen, C. Liao, B. Liang, J. Zhang, A. Li, B. Yang, Z. Zheng, X. Liu, A. Pan, S. Liang, R. Ma, Ni2P2O7 Nanoarrays with Decorated C3N4 Nanosheets as Efficient Electrode for Supercapacitors, ACS Appl. Energy Mater. 1 (2018) 2016–2023.

[166] K.M. Hercule, Q. Wei, O.K. Asare, L. Qu, A.M. Khan, M. Yan, C. Du, W. Chen, L. Mai, Interconnected nanorods-nanoflakes Li2Co2(MoO4)3 framework structure with enhanced electrochemical properties for supercapacitors, Adv.

Energy Mater. 5 (2015) 1–7.

[167] L. Gao, J.U. Surjadi, K. Cao, H. Zhang, P. Li, S. Xu, C. Jiang, J. Song, D. Sun, Y. Lu, Flexible Fiber-Shaped Supercapacitor Based on Nickel-Cobalt Double Hydroxide and Pen Ink Electrodes on Metallized Carbon Fiber, ACS Appl. Mater. Interfaces. 9 (2017) 5409–5418.

[168] B.A. Mei, J. Lau, T. Lin, S.H. Tolbert, B.S. Dunn, L. Pilon, Physical Interpretations of Electrochemical Impedance Spectroscopy of Redox Active Electrodes for Electrical Energy Storage, J. Phys. Chem. C. 122 (2018) 24499–24511.

[169] Z. Deng, C.-K. Ho, C.-Y.V. Li, K.-Y. Chan, An Impedance Study on Porous Carbon/Lithium Titanate Composites for Li-Ion Battery, ECS Meet. Abstr. MA2017-01 (2017) 613.

[170] C. Rokaya, J. Keskinen, D. Lupo, Integration of fully printed and flexible organic electrolyte-based dual cell supercapacitor with energy supply platform for low power electronics, J. Energy Storage. 50 (2022) 104221.

[171] W. Zuo, R. Li, C. Zhou, Y. Li, J. Xia, J. Liu, Battery-Supercapacitor Hybrid Devices: Recent Progress and Future Prospects, Adv. Sci. 4 (2017) 1600539.

**APPENDICES**

**APPENDICES A – List of peer-reviewed journal publications**

- Anjali Gupta, Cassia A. Allison, Anuj Kumar, **Rishabh Srivastava**, Wang Lin, Jolaikha Sultana, Sanjay R. Mishra, Felio Perez, Ram K. Gupta, Tim Dawsey (2023) "Tuned Morphology Configuration to Augment the Electronic Structure and Durability of Iron Phosphide for Efficient Bifunctional Electrocatalysis and Charge Storage" Journal of Energy Storage

**APPENDICES B – List of conference presentations**

- **Rishabh Srivastava**, and Ram K Gupta (2023) "Iron-pyrophosphate Rectifying Urea-rich Wastewater Pollution for Sustainable Hydrogen Production and Electronic Coupling to Improve Charge Storage" 2023 Joint Midwest and Great Lakes Regional Meeting ACS

- **Rishabh Srivastava**, Anjali Gupta, Cassia A. Allison, Ram K. Gupta, and Tim Dawsey (2023) "3D Crosslinked Ultrathin Flaky Structure of Nickel Metaphosphate for Durable Electrocatalysts for Water Splitting and Supercapacitors" ACS Fall 2023

- **Rishabh Srivastava**, Ram K Gupta (2023) "In situ influenced Facile Synthesis of Nickel Phosphide Nanocomposite on the Ni foam as Optimized Electronic Configuration for Bifunctional Electrocatalysts and Highly Encouraged Supercapacitor Electrode." 2023 PSU Research Colloquium

- **Rishabh Srivastava**, Himanshu Chaudhary, Ram K Gupta (2023) "Facile Synthesis of Metallic-$P_2O_7$ Embedded on Nickel sheet for Better Trifunctional Electrocatalyst and Supercapacitor Application" 2023 PSU Research Colloquium

- **Rishabh Srivastava**, Himanshu Chaudhary, Ram K Gupta (2023) "Facile synthesis of metallic-$P_2O_7$ on Nickel Foam for Tuned Morphological and Electronic Enhancement toward Bifunctional Electrocatalyst and Supercapacitor Application." 2023 MAS Annual Meeting